Light Harvesting and Photoconversion Efficiency Enhancement in Dye-Sensitized Solar Cells via Molecular and Photonic Advancements

by

Michael David Brown

Dissertation submitted for the degree of Doctor of Philosophy at the University of Oxford

January 2012

Department of Physics, University of Oxford

With thanks to Jesus College

Abstract

The main goal of this thesis is to investigate and develop the physics of dye-based photovoltaic physics through molecular and photonic routes. Numerous photovoltaics devices have been fabricated through the course of this work to study their characteristics, performance, physical composition and action. The relative youth of the field of dye-based optoelectronics provides extensive scope for new research which provides fascinating opportunities in terms of physical processes.This thesis is divided into two main projects; exploring the adaption of conventional dye-sensitized solar cells via starkly different routes which serendipitously culminated in striking similarities at their conclusion. The first route is through incorporating spectrally complementary dye molecules with the intention of extending the range of light absorption of the final devices. This initial aim was achieved and was then furthered by the realisation of an unexpected and unprecedented energy transfer process occurring, imparting enhanced photocurrent generation in both the near-IR and visibile region. The second route involves investigating the effect on dye-sensitized solar cell physics and performance of the inclusion of metallic nanoparticles with the expectation of inducing plasmonic interactions. Novel systems were designed and implemented, devices were made which display significant performance enhancement, attributed to plasmonic coupling into the dyes and thereby increasing photocapture. A number of other investigations are documented whose current completion does not sufficiently warrant independent chapters but whose scientific interest is evident.

Acknowledgments

This thesis is the culmination of work undertaken within the nascent Photovoltaics and Optoelectronics group in the Physics Department of the University of Oxford between October 2008 and January 2012.
The work was funded through a John Fell Studentship provided by the Oxford University Press.

Perhaps the greatest part of thanks must go to Dr Henry Snaith for his boundless enthusiasm and inspiration, for being my teacher and mentor and then allowing me the freedom to undertake my own research and, perhaps most significantly, for giving me the opportunity to make my own mistakes.

I have faced every trial and Snaithing of the last three years with both Pablo Docampo and Mike Lee, for that I should thank or apologise to them. I would also like to thank Annamaria Petrozza, Priti Tiwana and Patrick Parkinson for providing assistance with spectroscopy, I-Kang Ding for his XPS, Simon Fairclough for his TEMs, Michael Saliba for his ever-insightful research and thesis input, Paul Patterson for his infinite patience whilst we insidiously outgrew his clean room, Robin Nicholas as we stole his rooms, Laura Herz for letting me near her lasers and John Magorian for his sage(ish) wisdom. I must also thank our eventual legion of postdocs who provided people to talk to who weren't Henry, Pablo and Mike.

Katie Sissons demands acknowledgment. She gets it for being wonderful.

My big sister first taught me the word physics, my dad the ideas, my mum how to write them. I wrote this for them, so I thank them on the condition that they read it.

Michael David Brown

Oxford

January 2012

Contents

Abstract i

Acknowledgements ii

Table of Contents iii

List of Figures vi

1 Introduction 1

1.1 Background . . . 2

1.1.1 Energy Usage and Solar Incidence . . . 2

1.1.2 Photovoltaics . . . 2

1.1.2.1 Semiconductor Photovoltaics . . . 3

1.1.2.2 Thin Film PV . . . 4

1.1.2.3 Third Generation PV . . . 6

1.1.3 Dye-Sensitized Solar Cells . . . 6

1.1.3.1 Electrolytes . . . 6

1.1.3.2 Solid State . . . 7

1.2 Energetic Phenomena . . . 9

1.2.1 Energy Transfer . . . 9

1.2.1.1 Förster Resonant Energy Transfer . . . 9

1.2.1.2 Dexter Electron Transfer . . . 9

1.2.2 Surface Plasmon Polaritons . . . 10

1.3 Thesis Outline . . . 12

References 14

2 Methods and Experimental **17**

2.1 Solid State Dye Sensitized Solar Cell Function and Schematic 18

2.2 Solid State Dye Sensitized Solar Cell Production 19

2.3 Electrolyte Dye Sensitized Solar Cell Production 26

2.4 Device Characterisation 28

2.4.1 Current-Voltage and Photoconversion Efficiency Calculation 28

2.4.2 Spectral Response 34

2.4.3 Surface Profilometry 36

2.4.4 UV-Visible Spectrophotometry 36

References 38

3 Molecular Coadsorption Leading to Unprecedented Surface Energy Transfer **40**

3.1 Spectral limitations of solid-state dye-sensitized solar cells 41

3.2 Cosensitization of spectrally complementary dyes 42

3.2.1 Contemporary Literature 43

3.3 Device fabrication 44

3.3.1 Squaraine-Indoline cosensitization 44

3.3.2 Pthalocyanine-Indoline cosensitization 45

3.4 Intermolecular energy transfer 48

3.4.1 Förster Resonant Energy Transfer Theory 55

3.5 Conclusions 57

References 58

4 Plasmonic Nanostructures Incorporated into DSCs to Enhance Photocurrent Generation **62**

4.1 Plasmonics Introduction 63

4.1.1 Physical Explanation of Surface Plasmon Polaritons 63

4.1.2 Mathematical treatment 64

4.2 Plasmonic Solar Cell History and Contemporary Literature 66

4.3 Realisation of Plasmonic Dye Sensitized Solar Cells 67

4.3.1 Concept . . . 67
4.3.2 Evaporative metal island Incorporation . . . 67
4.3.3 Nanoparticle based Plasmonic Incorporation . . . 68
4.3.4 Incorporation methods . . . 68
4.3.4.1 Nanoparticle Fabrication and Encapsulation . . . 69
4.3.4.2 Nanoparticle Response to Sintering . . . 71
4.3.5 Characterisation of Nanoparticle-Incorporating DSCs . . . 71
4.3.6 Spectroscopy . . . 86
4.4 Conclusions . . . 91
References . . . 93

5 Ongoing projects **98**
5.1 Deriving current from non-injecting dyes . . . 99
5.2 Incorporation of further plasmonic nanostructure geometries . . . 103
5.2.1 Ultra-fast sintering of titania substrates through near-IR pulse techniques 103
5.3 Functional devices not incorporating a traditional hole transporting medium . . . 109
5.3.1 Carrier transport measurements . . . 110
References . . . 113

6 Conclusions and Outlook **115**

Refereed Publications and Conference Presentations **118**

A Appendices **120**
A.1 Structures of dyes and hole transport molecules . . . 120
A.2 Time correlated single photon counting . . . 126
A.3 Nanoparticle Synthesis Proceedures . . . 127
References . . . 128

List of Figures

1.1 Distribution of energy sources with respect to production capacity 3
1.2 Extra- and terrestrial incident solar spectrum and performance of a silicon PV cell 5
1.3 NREL photovoltaic efficiency progression 7
1.4 FRET and Dexter Energy Transfer Schematics 11

2.1 Simplified structural cross section of a typical solid-state DSC 18
2.2 Typical energy level diagram as occuring in a functional sDSC junction 19
2.3 SEM image of a titania mesostructure prepared by screen printing 22
2.4 Spiro OMeTAD structure 24
2.5 Graphic illustrating the appearance of a typical ssDSC 25
2.6 Two real solid state dye sensitized solar cells 25
2.7 Graphic illustrating the appearance of a typical electrolyte DSC 27
2.8 A fully-fabricated electrolyte dye sensitized solar cell 27
2.9 Typical diode response upon current-voltage characterisation 29
2.10 Simplified solar cell current-voltage characterisation 30
2.11 The fourth quadrant current density-voltage curve 31
2.12 Power-voltage curve from the current-voltage curve of figure 2.11 33
2.13 Solar simulator system layout 34
2.14 Spectral response system layout 35
2.15 Relating absorption, reflectance and transmission 37

3.1 Absorption spectra for D102 and TT1 43
3.2 Current density-voltage characteristics of cosensitized sDSCs 45
3.3 Quantum Efficiency Measurements for Co- and singly sensitized SDSCs. 46

3.4 Energy level diagram for a two dye pthalocyanine-indoline system. 47
3.5 Photoluminescence spectra for relevant cosensitized molecules 50
3.6 Normalised photoluminescence spectra for relevant cosensitized molecules 51
3.7 Normalised PL decay spectra for coadsorbed molecules 52
3.8 Ratios of PL emission for chromophores singly- and co-sensitized 53
3.9 FRET and Dexter Energy Transfer Schematics 55

4.1 Amplitude of surface plasmon field at a metal-dielectric interface 64
4.2 Amplitude of surface plasmon field around a shelled spherical metal particle . . . 65
4.3 Simple schematic of spin coat or doctor blade incorporation routes 69
4.4 Au and Au-SiO_2 nanoparticle TEM images 70
4.5 Absorption of films incorporating nanoparticles before and after sintering 72
4.6 Transmission and reflectance profiles of nanoparticle-incorporating TiO_2 films . . 74
4.7 Current-voltage characterisation for eDSCs containing bare nanoparticles 75
4.8 Doctor blade nanoparticle incorporation: ablative XPS depth profile 77
4.9 Spin coat nanoparticle incorporation: ablative XPS depth profile 78
4.10 SEM of gold np integrated TiO_2 mesostructure 79
4.11 J-V characterisation of liquid-phase HTM plasmonic hybrid devices 80
4.12 Optically thin and thick films with and without nanoparticle incorporation . . . 82
4.13 Absorption and spectral response of eDSCs with and without Au-SiO_2 nanoparticles 83
4.14 Spectral response for typical Z907 sDSC with and without Au-SiO_2 nanoparticles 84
4.15 Current voltage characterisation of solid state plasmonic hybrid devices 85
4.16 Histogram of JV performance statistics for plasmonic sDSCs 87
4.17 Photo-Induced Absorption (PIA) 89

5.1 Perylene diimide structure 100
5.2 Absorption and quantum efficiency spectra for perylene and TT1 101
5.3 TEM graphics and transmission spectra of gold@silica nanobars 104
5.4 Transmission spectra of various IR pulse-sintered films 106
5.5 Current-Voltage characterisation IR pulse sintered devices 107
5.6 Current-Voltage characterisation for devices without HTM 109
5.7 Spectral response characterisation for devices without HTM 111

5.8 Transport measurements for devices with and without HTM 112

Chapter 1

Introduction

An introduction to, and concise summary of, the work undertaken in this thesis is given, including a brief indication of the necessity and categorisation of photovoltaics, the function of dye-sensitized solar cells, their limitations and the research that has been done towards investigating and enhancing photoconversion efficiency.

1.1 Background

1.1.1 Energy Usage and Solar Incidence

In recent years there has been a significant and mounting interest in renewable energy research and uptake, in part due to realisation of the finite nature of fossil fuels as well as increasing concern for the carbon footprint created by most large-scale energy production methods and the subsequent anthropogenic warming of the climate that is discussed and debated comprehensively and exhaustively elsewhere.[1] Even negating the topic of climate change, current global energy usage has a very clear bias towards unsustainable fossil fuels with renewables, despite some investment, still trailing in terms of uptake. This is illustrated in Figure 1.1, clearly showing that the vast majority of energy is provided from sources that in the long term are unable to sustain this demand.[2,3] This has led to extensive investment in renewable technologies of all kinds, many of which, directly or indirectly, rely on the sun as the ultimate source of energy. The most direct of these technologies can be found in photovoltaics, implementing the direct conversion of sunlight into electricity. Photovoltaics (PV) already has a lengthy history, with silicon receiving the most attention early on and consistently being the most visible and investigated aspect of the field. Simply put, the global energy usage of modern civilisation far exceeds that which is sustainable with currently used generation systems. Although other forms of renewable energy source are available [4,5] and others such as fusion may prove vital, it is considered sufficient for this thesis to simply note that energy is a significant global consideration and that solar power may, in some form, aid this situation.

1.1.2 Photovoltaics

The average sunlight incidence on the earth's surface equates to around 120,000 TW,[6,7] while the current global energy requirements are estimated to be in the region of 15TW.[6] Even neglecting the 71% of the Earth's surface that is covered in water and the 40% of the remaining land which is assumed to be precluded for use due to necessary photosynthetic vegetation coverage, the approximately remaining 20,000 TW are far in excess of the energy demands of humanity, which currently corresponds to 15TW, but is ever-increasing. Indeed, it can be noted that worldwide photosynthesis is estimated to generate in excess of 100TW in its own right,[7] noted to be far greater than the energy demands of human activity. This simple estimation does

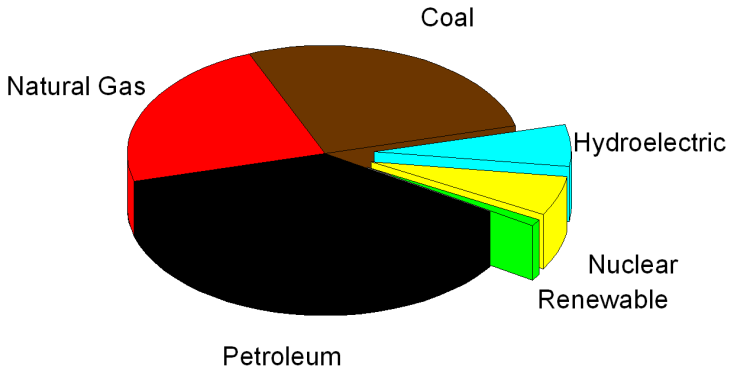

Figure 1.1: Illustrating the distribution of energy sources with respect to production capacity. *Data taken from the US Energy Information Administration. Annual Energy Review 2010*

not consider the effects of solar heating of the terrain, global albedo [8] or similar and is instead intended to be a rudimentary indication of the lengths to which the sunlight incident to the Earth exceeds the current and projected energy use of mankind. Despite this, it is understood to be significantly beyond the function of this thesis to discuss in any detail the ecological, engineering and political impacts of global energy use and any prospective usage increase of photovoltaics.

Significant amounts of money and research have been injected into projects exploring further new PV technologies, with concepts ranging from high efficiency and cost multijunction devices (part of the so-called "first generation") to low efficiency inorganic devices whose relatively poor energy output is compensated for by extremely competetive costs of materials and production (comprising, variously, the second and third generation).

1.1.2.1 Semiconductor Photovoltaics

In 1839 Becquerel observed the generation of a weak electrical current with the exposure of sunlight to a simple device of two metal plates separated by an electrolytic liquid; this was the first known observation of the photovoltaic effect.[9] The first recognisable p-n junction based solar cell was reported by Bells Labs in 1954;[10] semiconductor solar cells at their most basic consist of a p-n junction at which the absorption of photons excites electrons into the conduction band, where the band distortion imposed by the p-n junction fascilitates the separation

of electrons and holes. The first photovoltaics devices were developed concurrently with the birth of transisters, exploiting some of the same fundamental physics and sharing a comparable production method of semiconductor solar cells; the maturation of silicon transistor technology through the late 20th century paying dividends into silcon solar cells. Solar cells were then developed and optimised for the space programme, where cost was rendered insignificant compared to efficiency. In spite of the efficacy and established nature of this technology, there are many problems hindering semiconductor PV's widespread use. It is not unreasonable to consider silicon as the most commercially viable semiconductor PV devices, due to its ubiquity, the high cost of many alternatives and the experience of the silicon industry, which provides a readily available area of expertise and equipment for silicon PV. The limited uptake is perhaps caused by the high-capital silicon production method itself; indeed, the enormity of the silicon industry as relating to processing chips for consumer electronics has resulted in frequent shortages of the high-grade silicon necessary to produce solar cells.[?] The uptake is further hindered by the non-ideal response to low light conditions, which sees the output of silicon PV diminish faster than linearly with reduction in incident flux. Another of the limitations of conventional semiconductor devices is posed by their very nature: the Shockley-Queisser Limit [11] defines the absolute maximum efficiency a semiconductor device can reach and is dependant upon the bandgap of the semiconductor in question and the fixed solar spectrum itself. This is more clearly illustrated by figure 1.2. For example silicon, the semiconductor most commonly used in photovoltaic applications, has a bandgap of ~1.1eV and, as calculated by Shockley and Queisser in their original paper, a photoconversion efficiency limit of ~30%. The Shockley-Queisser limit can be exceeded by utilising the bandgaps of more than one semiconductor material; multijunction solar cells incorporating many layers of semiconductors with different band gaps have been fabricated, culminating in efficiencies in excess of 40% under concentration.[12] Unfortunately, despite these obviously impressive energy conversion efficiencies, the production complexity, cost and fragility of multijunction devices outweighs the performance for most uses other than that where cost is not a factor such as space applications.

1.1.2.2 Thin Film PV

Although the realisation of ever-greater efficiencies is a boon for the field of photovoltaics, it may also be that the route of reducing the cost may also lead to the increased uptake of

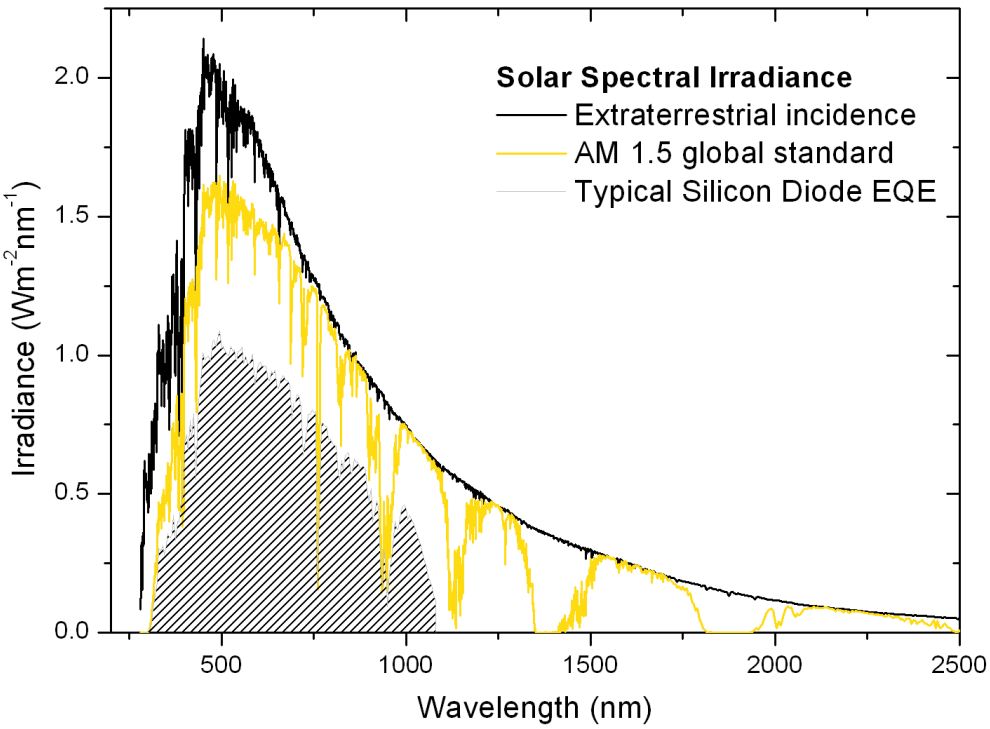

Figure 1.2: Spectrum for solar irradiance showing extraterrestrial (black) and standard terrestrial surface incidence at AM 1.5 (yellow). Also shown is an uptake spectrum for a typical silicon photovoltaic device as a proportion of the incident. Note the sharp turn off of the diode at ~1080nm, equivalent to the 1.1eV bandgap of silicon. *Data for solar spectrum taken from National Renewable Energy Laboratory database for ASTM G173-03 Reference Spectra Derived from SMARTS v. 2.9.2. Data for silicon diode derived from known quantum efficiency spectra for Centrionic Series 7 OSD5.8-7 UV matched photodetector.*

lower capital devices. Sometimes refered to as 'second generation', the field of thin-film PV endeavours to fabricate effective solar cells from less materials with lower production costs than are otherwise encountered by the production of semiconductor PV. The most sucessful example of this technology is evidenced by CIGS solar cells (Copper-Indium-Gallium-Arsenide) which are significantly thinner than tradiational silicon solar cells but can still boast efficiencies approaching 15%.[13] However, due to their similar crystalline nature to silicon, the fabrication processes and overall manufacture is still difficult and expensive,[14] as illustrated by their limited uptake heretofore.

1.1.2.3 Third Generation PV

The concept of "third generation PV" is one which attempts to conflate the impressive efficiencies of the first generation with the more tenable costs of the second. This would be an extremely advantageous state of affairs with a significant energy output for a more reasonable energy cost than has hitherto been realised. At the time of writing no system has been developed which can compete with the efficiency levels of traditional semiconductor photovoltaics whilst retaining the cost advantages of other systems. Amongst the new contenders, dye-sensitized solar cells (DSCs) show great promise, balancing good photovoltaic conversion efficiency whilst remaining cost effective. Indeed, there has been speculation that the photoconversion efficiency of these devices could approach 25% in which circumstance, if the low production cost were retained, DSCs would be rendered an extraordinarily viable energy resource.[15] To date the highest performing DSC achieves around 11% absolute efficiency (figure 1.2), leaving great scope for improvement in the field.

1.1.3 Dye-Sensitized Solar Cells

1.1.3.1 Electrolytes

Dye-sensitized solar cells have a long history, with a number of papers defining the work on zinc oxide [16,17] and tin sulphide electrodes.[18] It was only with the implementation of a titania (TiO_2) nanoparticle film and more stable ruthenium dye described by O'Regan and Grätzel [19] in 1991 that the performance of these devices began to show the performance that appeared possible. The field began in earnest after the publication of the TiO_2 work and, with the

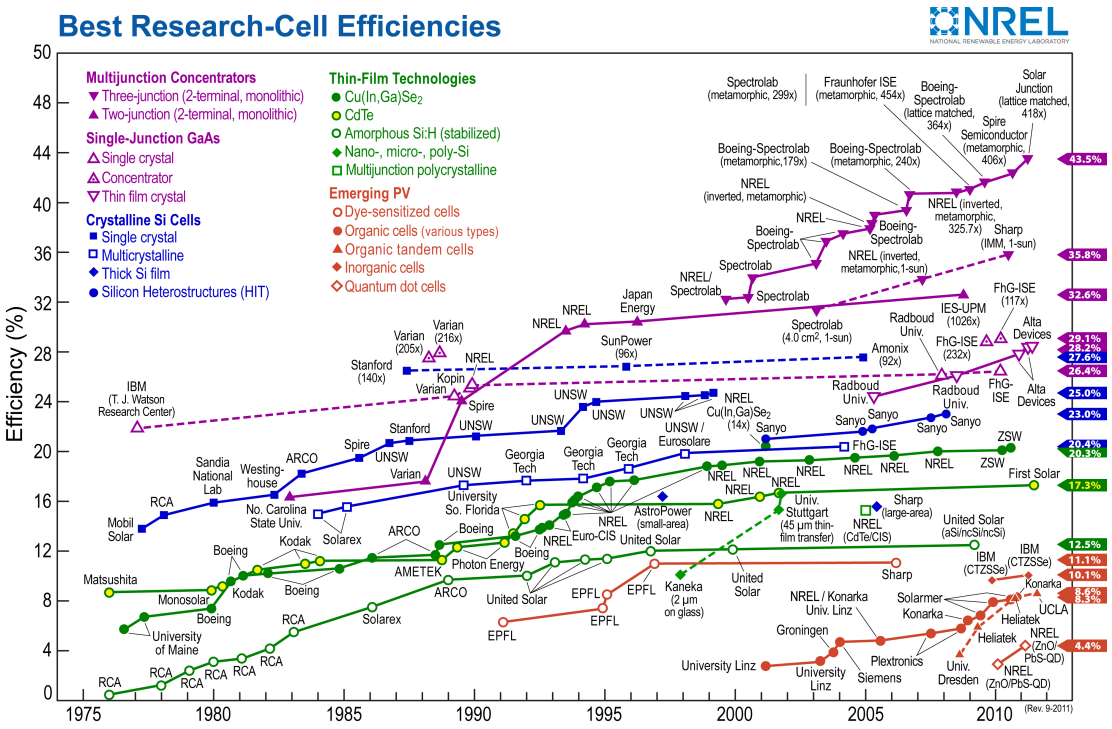

Figure 1.3: Progresssion of certified record efficiencies for a variety of PV technologies. *Data taken from the US National Renewable Energy Laboratory (NREL), September 2011*

continuing efforts of the group at the École Polytechnique Fédérale de Lausanne (EPFL), are sometimes known by the moniker 'Grätzel Cells'. The first devices from this paper achieved photoconversion efficiencies of around 7.1% using a ruthenium based sensitizer and were the first time that dye-sensitized devices had showed promise of their capability to compete with other photovoltaic technologies in development. The progress made by electrolyte DSCs since their inception is most clearly seen in the absolute performance increases that have been observed, as shown in figure 1.3. Although still unable to compete with the performance attained by semiconductor PV, the promise of a relatively low cost-performance ratio for DSCs makes them a promising commercial possibility.[20]

1.1.3.2 Solid State

There are a number of limitations of the established electrolyte devices, including the volatility and toxicity of the electrolyte itself [20] that make the investigation of a solid state replacement

of the hole transport medium (HTM) worthwhile. Moreover the challenges of scaling the orthodox devices are not insignificant, mainly due to the liquid aspect; many complexities arise in both engineering and performance areas that might preferable be avoided. Industrially, although significant work has been undertaken in the field of scaling and commercialising these devices,[21, 22] it may be more attractive to invest in research into the replacement of the liquid phase of the system with a gel, melt or solid state electrolyte. The first solid-state DSC (sDSC) were presented in 1997 by O'Regan et al. and Tennakone et al., utlizing copper-based inorganic semiconductors (copper(I) thiocyanate(CuSCN) and copper(I) iodide (CuI) respectively) [?, 23, 24] and, although promising, the stability limitations associated with copper-based solid-replacement HTMs prevent its wider uptake.[25] Despite a number of solid phase predecessors, it was the implementation of polymer and molecular HTMs in 1997 by Yanagida et al. and in 1998 by Bach et al. respectively [?, 26] that gave the first real possibility of replacing the non-ideal liquid component of the devices.

Although it was one of the first molecular HTMs to be incorporated into DSCs, 2,2',7,7'-tetrakis(N,N-di-p-methoxyphenylamine)-9,9'-spirobifluorene (Spiro OMeTAD) reported by Bach et al,[?] none have yet surpassed its versatility and performance in sDSCs. It is this HTM that is used throughout this thesis unless otherwise stated. The introduction of entirely solid-state devices, whilst circumventing the weaknesses inherent to liquid components, currently poses a number of alternative limitations. Photoconversion in sDSCs is limited to a large extent by poor light harvesting, both in extinction strength and bandwidth. This arises for a number of reasons, the most significant of which is the restriction on the thickness of the mesostructure that is imposed by the necessity to achieve satisfactory pore filling and limit recombination losses.[27] The result of this is that the absorption profiles of the dyes utilised become more significant in sDSCs. The ruthenium dyes commonly used in electrolyte DSCs [28, 29] tend to absorb broadly, but without a sufficient extinction coefficient to approach complete light harvesting from the thin films neccessary for sDSCs. It may be noted that, even if these dyes could be more heavily loaded or adsorbed to a thicker film and perform efficiently in a sDSC, being an exceptionally valuable metal and increasingly rare,[30] it would still be attractive to reduce the use of ruthenium-centred dyes. On the other hand, the organic dyes increasingly used such as the indolines or the porphyrins, tend to have narrower but stronger absorption profiles.

1.2 Energetic Phenomena

This section briefly introduces two energetic processes that are pivotal to the work done within this thesis. The first is molecular energy transfer, either by dipole resonance (FRET) or electron transfer (Dexter). The second is plasmonics, specifically surface plasmons occuring at metal-dielectric interfaces. All are more comprehensively introduced within their respective chapters.

1.2.1 Energy Transfer

1.2.1.1 Förster Resonant Energy Transfer

The resonant energy transfer process, first defined by Förster[31] and so often denoted Förster resonant energy transfer (FRET) occurs with the overlap of the donor molecule's flourescence profile with the absorption spectrum of an acceptor molecule but is a non-radiative process, instead depending upon dipole-dipole coupling between the two molecules.

The FRET rate ($k_{Förster}$), can be simply illustrated by the proportionality:

$$k_{Förster} \propto \frac{1}{\tau_d}\left(\frac{J}{r}\right)^6 \tag{1.1}$$

where τ_d is the radiative lifetime of the donor excitation, ϕ_d is the donor photoluminescence and J is the overlap integral, defined as:

$$J = \int f_D(\lambda)\epsilon_A(\lambda)\lambda^4 d\lambda \tag{1.2}$$

It can be noted that both Dexter electron transfer and FRET are dependant upon the overlap integral; that is, the absolute overlap between the flourescence profile of the donor and the absorption spectra of the acceptor molecule. Figure 1.4 shows the energetic processes associated with Förster resonant energy transfer, in contrast to the action of Dexter energy transfer.

1.2.1.2 Dexter Electron Transfer

In contrast to the direct energetic transfer that occurs by FRET, energy can also be transferred indirectly by electron transfer. In this case the transfer of an excited electron necessarily transfers the associated energy to the acceptor molecule. Dexter transfer has an energy transfer rate that follows as the exponential of the separation distance:

$$k_{Dexter} \propto J \cdot exp\left(-\frac{2r}{L}\right) \tag{1.3}$$

where L is the sum of the Van der Waals radii for the donor and acceptor molecule. Figure 1.4 illustrates Dexter energy transfer in comparison to FRET. As the Dexter rate follows a simple exponential decay unlike the sixth power associated with FRET, it may be possible to distinguish the two processes.

1.2.2 Surface Plasmon Polaritons

Surface plasmons are a quasiparticle interpretation for the occurance of guided waves at the inferface between a metal and dielectric. The free electonic nature of metals allows collective response to electromagnetic fields. This phenomena introduces an extremely high absorptive nature to certain metal nanostructures when in the medium of a dielectric material. The nature of plasmons can be formally derived mathematically from the Maxwell equations (section 4.1.2) and from thence, theoretical models can be derived. Note however that the overidding function of this thesis is the experimental application of this phenomena and as such no extensive modelling has been undertaken.

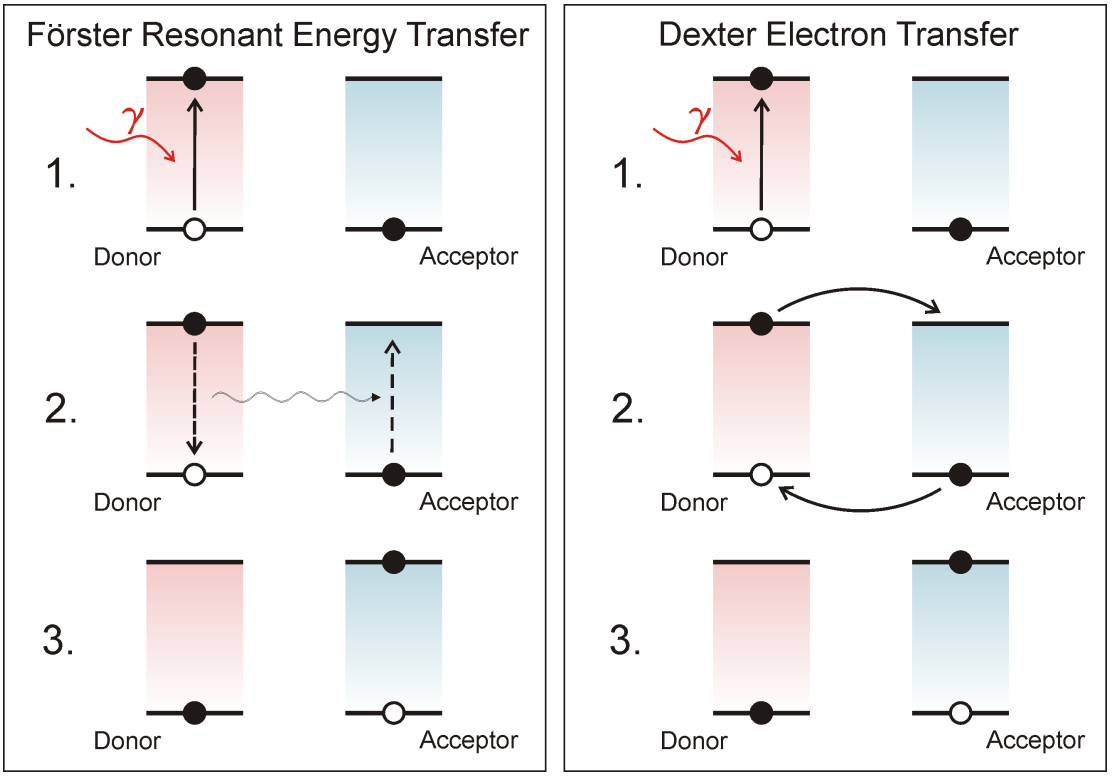

Figure 1.4: FRET and Dexter Energy Transfer Schematics. The left panel shows the energetics associated with FRET and the right shows those for Dexter electron transfer.

Förster resonant energy transfer: 1. donor excitation, 2. non-radiative donor relaxation, induced excitation in acceptor by FRET, 3. excited acceptor.

Dexter energy transfer: 1. donor excitation, 2. electron transfer - excited electron transferred donor to acceptor, ground state electron transferred acceptor to donor, 3. excited acceptor.

1.3 Thesis Outline

The primary aim of this thesis is to investigate the physics of dye-senstized solar cells (DSCs) with a mind to improving photoconversion efficiency and hence their possible uptake into energy provision. One of the most damaging limitations of dye-sensitized solar cells at present, and most significantly in the solid state branch of the field, is the light harvesting capabilities of the dye molecules themselves, all constrained by the necessity of also balancing these absorption characters with carrier handling properties. A comprehensive overview of the structure, fabrication and characterisation of a typical solid state DSC is undertaken in Chapter 2, followed by chapters 3-5 dealing with the experiments undertaken. Several routes for the enhancement of light harvesting in DSCs have been investigated during the course of this work and are delimited into two primary projects: Chapter 3 explores the effect of cosensitization of the devices with a secondary dye molecule, initially for the spectral expansion this provided but investigated further when an unanticipated energy transfer process was observed; Chapter 4 documents the inception, investigation and realisation of plasmonic hybrid DSCs through the incoporation of core-shell nanoparticles through a variety of routes. Chapter 5 documents a number of secondary projects that have not been developed to the same degree of fruition but whose preliminary findings or interim results suggest that further research would be well justified.

The projects undertaken are discussed and reconciled in the concluding chapter 6, where the possible impact of this work is noted as well as the outlook for the technology as a whole.

In both solid state and electrolyte DSCs the light harvesting is of primary importance to the efficient performance of the devices. The primary goal of this thesis is to investigate a number of routes by which the photouptake of complete devices can be increased without comprimising their function in any other manner. With sDSCs requiring the most enhancement in this area, it is therefore pragmatic to explore photoconversion enhancing methods in fully solid-phase devices, while some consideration is given that the systems developed through the course of this work are likely to be applicable to both solid- and electrolyte DSCs. It is hoped that this thesis act as a testament demonstrating the state of the field, at the time of writing, for DSCs incoporating plasmonic or energy transfer processes, as well as providing a brief inexhaustive account of the fabrication and research being undertaken in the field of dye-sensitized solar cells

and, in particular, solid state DSCs.

References

[1] A. Gore, *An Inconvenient Truth: The Planetary Emergency of Global Warming and What We Can Do About It.* Rodale Books, May 2006.

[2] A. Witze, "That's oil, folks...," *Nature*, vol. 445, no. January 2007, pp. 14–17, 2007.

[3] J. Giles, "Every last drop," *Nature*, vol. 429, no. June, 2004.

[4] F. Armstrong and K. Blundell, *Energy... Beyond Oil.* Oxford University Press, USA, Dec. 2007.

[5] D. J. C. MacKay, *Sustainable Energy - Without the Hot Air.* 2008.

[6] R. M. Nault, "Basic Research Needs for Solar Energy Utilization: Report on the Basic Energy Sciences Workshop on Solar Energy Utilization," tech. rep., Argonne National Laboratory, 2005.

[7] K. H. Nealson and P. G. Conrad, "Life: past, present and future.," *Philosophical transactions of the Royal Society of London. Series B, Biological sciences*, vol. 354, pp. 1923–39, Dec. 1999.

[8] P. R. Goode, J. Qiu, V. Yurchyshyn, and J. Hickey, "Earthshine Observations of the Earth's Reflectance," *Geophysical Research Letters*, vol. 28, no. 9, pp. 1671–1674, 2001.

[9] A. E. Becquerel, "Mémoire sur les effets électriques produits sous l'influence des rayons solaires," *Comptes Rendus des Séances Hebdomadaires*, vol. 9, pp. 561–567, 1839.

[10] D. M. Chapin, C. S. Fuller, and G. L. Pearson, "A New Silicon P-n Junction Photocell For Converting Solar Radiation Into Electrical Power," *Journal of Applied Physics*, vol. 25, pp. 676–677, 1954.

[11] W. Shockley and H. J. Queisser, "Detailed Balance Limit of Efficiency of P-n Junction Solar Cells," *Journal of Applied Physics*, vol. 32, p. 510, 1961.

[12] M. A. Green, K. Emery, Y. Hishikawa, and W. Warta, "Solar cell efficiency tables (version 37)," *Library*, no. version 37, pp. 84–92, 2011.

[13] O. Morton, "A New Day Dawning?," *Nature*, vol. 443, no. September, pp. 19–22, 2006.

[14] G. E. Jabbour and D. Doderer, "Quantum dot solar cells: The best of both worlds," *Nature Photonics*, vol. 4, pp. 604–605, Sept. 2010.

[15] H. J. Snaith, "Estimating the Maximum Attainable Efficiency in Dye-Sensitized Solar Cells," *Advanced Functional Materials*, vol. 20, pp. 13–19, 2010.

[16] M. Matsumura, Y. Nomura, and H. Tsubomura, "Dye-sensitization on the Photocurrent at Zinc Oxide Electrode in Aqueous Electrolyte Solution," *Bulletin of the Chemical Society of Japan*, vol. 50, no. 10, pp. 2533–2537, 1977.

[17] N. Alonso, V. M. Beley, P. Chartier, and V. Ern, "Dye sensitization of ceramic semiconducting electrodes for photoelectrochemical conversion," *Rev. Phys. Appl. (Paris)*, vol. 16, no. 1, pp. 5–10, 1981.

[18] F. Willig, R. Eichberger, N. S. Sundaresan, and B. A. Parkinsons, "Experimental Time Scale of Gerischer's Distribution Curves for Electron-Transfer Reactions at Semiconductor Electrodes," *Journal of the American Chemical Society*, vol. 112, no. 7, pp. 2702–2707, 1990.

[19] B. O. O'Regan and M. Gratzel, "A low-cost, high efficiency solar cells based on dye-sensitized colloidal TiO2 films," *Nature*, vol. 353, pp. 737–740, 1991.

[20] K. Kalyanasundaram, *Dye-sensitized Solar Cells*. CRC Press, 1 ed., 2010.

[21] T. Watson, I. Mabbett, H. Wang, L. Peter, and D. Worsley, "Ultrafast near infrared sintering of TiO 2 layers on metal substrates for dye-sensitized solar cells," *Progress In Photovoltaics*, pp. 482–486, 2011.

[22] E. Shiells, "A bright future for solar cells," *Highlights in Chemical Technology*, 2008.

[23] B. O. O'Regan and D. T. Schwartz, "Efficient Photo-Hole Injection from Adsorbed Cyanine Dyes into Electrodeposited Copper(1) Thiocyanate Thin Films," *Chem Mater*, vol. 7, pp. 1349–1354, 1995.

[24] B. O. O'Regan and D. T. Schwartz, "Efficient dye-sensitized charge separation in a wide-band-gap p - n heterojunction," *Journal of Applied Physics*, vol. 80, no. October, pp. 4749–4754, 1996.

[25] V. Perera and K. Tennakone, "Recombination processes in dye-sensitized solid-state solar cells with CuI as the hole collector," *Solar Energy Materials and Solar Cells*, vol. 79, pp. 249–255, Sept. 2003.

[26] K. Murakoshi, R. Kogure, Y. Wada, and S. Yanagida, "Solid State Dye-Sensitized TiO2 Solar Cell with Polypyrrole as Hole Transport Layer," *Chemistry Letters*, vol. 26, pp. 471–472, 1997.

[27] H. J. Snaith, R. Humphry-Baker, P. Chen, I. Cesar, S. M. Zakeeruddin, and M. Gratzel, "Charge collection and pore filling in solid-state dye-sensitized solar cells," *Nanotechnology*, vol. 19, p. 424003, 2008.

[28] M. K. Nazeeruddin, A. Kay, E. Miiller, P. Liska, N. Vlachopoulos, M. Gratzel, C. Lausanne, and R. April, "Conversion of light to electricity by cis-X2bis(2,2'-bipyridyl-4,4'-dicarboxylate)ruthenium(II) charge-transfer sensitizers (X = Cl-, Br-, I-, CN-, and SCN-) on nanocrystalline titanium dioxide electrodes," *Journal of the American Chemical Society*, no. 4, pp. 6382–6390, 1993.

[29] Y. Tachibana, K. Nazeeruddin, M. Gr, D. R. Klug, and J. R. Durrant, "Electron injection kinetics for the nanocrystalline TiO2 films sensitised with the dye (Bu4N)2Ru(dcbpyH)2(NCS)2," *Chemical Physics*, vol. 285, pp. 127–132, 2002.

[30] C. N. Chervin, A. M. Lubers, J. W. Long, and D. R. Rolison, "Making the Most of a Scarce Metal," *Naval Research Laboratory Review*, vol. 2, pp. 192–193, 2009.

[31] T. Forster, "Transfer Mechanisms Of Electronic Excitation," *Disc. Faraday. Soc*, no. 10, pp. 7–17, 1959.

Chapter 2

Methods and Experimental

The fabrication and subsequent characterisation of the devices investigated in this thesis are explored. A complete synthesis protocol for solid state dye-sensitized solar cells is given from constituent elements to finished device. The various methods of characterisation that will be used throughout this work are then outlined.

2.1 Solid State Dye Sensitized Solar Cell Function and Schematic

Dye-sensitized solar cells (DSCs) exploit the light absorptive properties of dye molecules by providing an architecture in which energetically excited electrons and holes in photoexcited dye molecules can be separated and so generate photocurrent. In order to provide the greatest interface area per incident area, the dye molecules are adsorbed to a high surface area 'mesostructure' of semiconducting metal oxide (usually, and throughout this thesis, titanium dioxide). This mesostructure and charge separation of this system is illustrated in a cross sectional device schematic of figure 2.1.

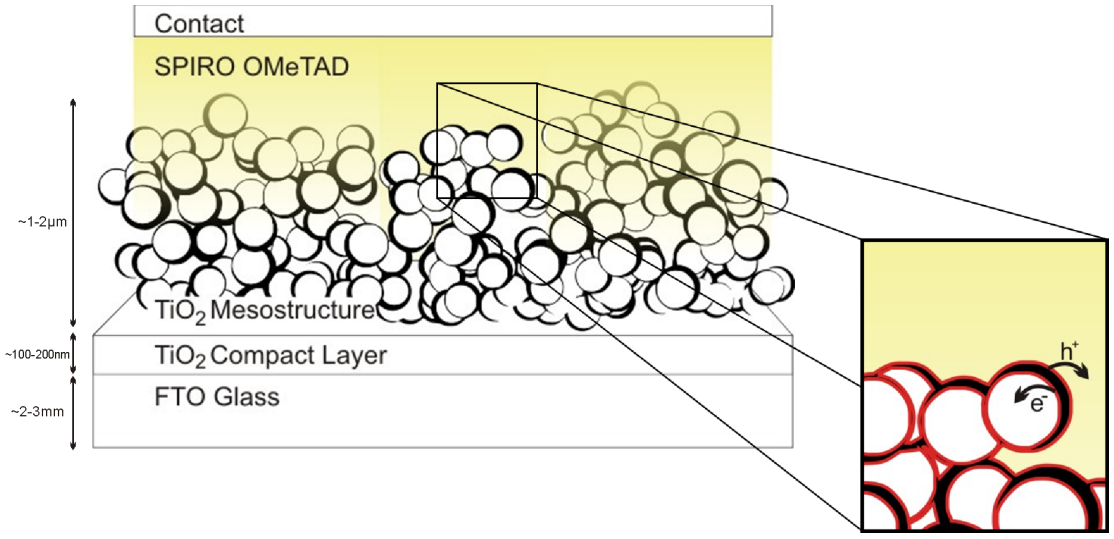

Figure 2.1: Simplified structural cross section of a typical solid-state DSC incoporating a transparent FTO substrate-electrode supporting a titanium dioxide (titania) mesostructure, sensitized with a photoactive dye infilitrated and capped with a solid state hole transporter (Spiro OMeTAD) covered by a metal counter-electrode. Inset shows the charge separation in the excited dye molecule with transfer of the electron(e^-) into the semiconducting titania and the hole (h^+) injected into the HTM

Typically DSCs utilise the injection of electrons into the metal oxide mesostructure and holes are transfered into a preferential hole transporting medium; in the case of electrolyte devices this is often a tri/iodide redox couple, whilst solid-state DSCs (sDSCs) utilise a molecular hole transporter such as 2,2',7,7'-tetrakis(N,N-di-p-methoxyphenylamine)-9,9'-spirobifluorene (often referred to as Spiro OMeTAD or, simply, Spiro).[?]

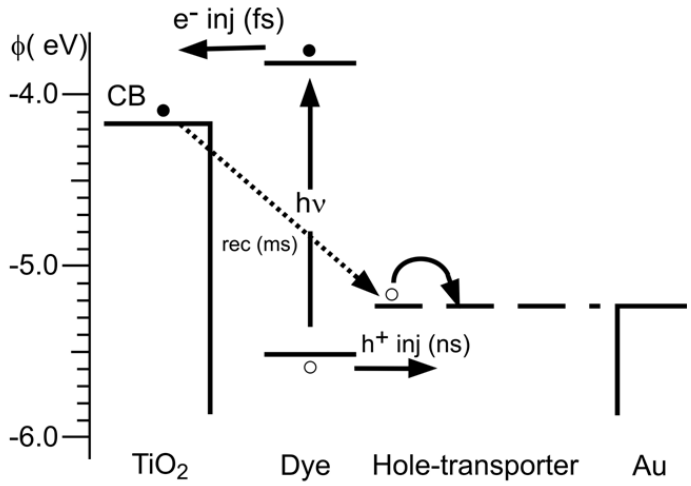

Figure 2.2: Energy level diagram for the junction as occuring in a functional dye-sensitized solar cell. Injection (inj) and recombination (rec) rates are indicated in parenthesis. *Adapted from* [6]. A further band diagram is shown in figure 3.4 of chapter 3.

There has been some work done into the fabrication of electron carrying mediums immersing a hole transporting metal oxide however, at the time of writing these investigations have not approached the performance of the orthodox system.[1, 2] Beyond titania, there have also been investigations into other metal-oxides such as tin oxide (SnO_2) [3, 4] and zinc oxide (ZnO) [4, 5] as a means of controlling the energy level structure of the devices and to potentially optimise the current and voltage balance of the devices. The energy level arrangement of a typical titania DSC is shown in figure 2.2.

2.2 Solid State Dye Sensitized Solar Cell Production

The techniques of sDSC production are noted in several manuscripts.[6, 7] The methods outlined here are by no means absolute but represent a typical route to solid state DSC fabrication utilised during the preparation of this thesis; unless otherwise stated the devices realised and investigated during the following chapters correspond broadly to the fabrication methods detailed within this chapter.

FTO Etch

Glass pre-treated with a layer of flourine-doped tin oxide (FTO), is used as the transparent substrate-electrode through which light passes to reach the active area of the complete devices. FTO supplied at 4mm thickness by Nippon Sheet Glass at TEC-15 specification, corresponding to a resistance of $15\Omega/\square$. To etch the FTO, the surface is simply reduced by hydrochloric acid (2M) in the presence of zinc powder. The FTO surface is negatively charged by the electrons of the zinc and the addition of hydrochloric acid evolves hydrogen as:

$$Zn + 2HCl \longrightarrow ZnCl_2 + 2H \tag{2.1}$$

at this point, hydrogen atoms reduce the tin of the FTO (Sn^{4+}) to metallic tin, etching the FTO by breaking the structure and so allowing it to be removed by mechanical action. The sheets are then cleaned with soap (2% halmanex in water), distilled water, ethanol and acetone.

Plasma Etch

Prior to deposition of layers, the FTO glass is plasma etched to remove any organic contaminants on the surface of the device as well as to introduce a degree of surface roughness which improves the compact and mesostructure layer adhesion to the otherwise pristine surface. The glass substrates are placed into a vacuum chamber pumped down to around 0.1 mBar, repressurised to 0.2-0.3 mBar with oxygen and subjected to 100W continuous microwave radiation, forming an oxygen plasma, etching the organic detritus from the glass surface as well as the glass itself, imposing a degree of roughness which later in the fabrication process facilitates the adhesion of the metal oxide layers to the glass surface. The system used is the Diener Electronic Pico UHP plasma etcher.

Spray Pyrolysis

Following the plasma etch of the FTO/glass surface, the substrate is heated to 400-500°C at which point a compact layer of TiO_2 is established by spray pyrolysis on the surface from a solution of di-iso-propoxy titanium-bis(acetylacetone) in ethanol (often termed titanium AcAc) as previously described by Kavan et al.[8] The intermediate layer ensures the delimitation of the conducting FTO layer from the HTM that will subsequently be infiltrated through the metal

oxide mesostructure. If the compact layer is neglected there results the possibility of direct contact between the HTM and the FTO, so providing an internal short circuit and so crippling the current generation of the final device. The hot plates used for heating processes in the preparation of this thesis are 240V 10A directed by model PR 5 3T controllers with NiCr-Ni(K) thermocouple probes produced by Detlef Gestigkeit Elektrotechnik.

Metal Oxide Mesostructure Fabrication

Two broadly equivalent mesostructure fabrication methods were utilised in the production of consistent metal oxide substrates. Unless otherwise stated all mesostructures discussed are based on a Dyesol produced paste of anatase TiO_2 nanoparticles buffered with ethyl-cellulose (DSL 18NR-T). The following methods discussed for film production are followed by a ramped sinter process to 500°C for 30 minutes, removing the ethyl-cellulose and attendant solvents.

Doctor Blading

Doctor blading describes the distribution of an thin, even layer of a film upon a substrate prior to sintering that will then provide a homogeneous layer. This is the method most regularly used in the following chapters. A TiO_2 nanoparticle paste is produced from the previously mentioned Dyesol (DSL 18NR-T) paste diluted with ethanol to a proportion between 1:2 and 1:3. The diluted paste is applied in a strip along one edge of the glass substrate and is then spread evenly across using a blade or other smooth edge, in most cases with a thickness dependant addition such as a height controlling micrometer for the blade edge or, more primitively, a tape of known thickness.[9]

Screen Printing

Although the doctor blade route to mesostructure fabrication can, with experience, produce consistent and homogeneous films, it is also susceptible to variation due to individual variation in application and interpretation of form. As such, a more standardised process provides greater capability for trustable comparison between different fabrication engineers and between fabrication runs themselves. To this end a second method of mesostructure fabrication was developed which to some extent removes the human inconsistency associated with previous doctor blading methods.

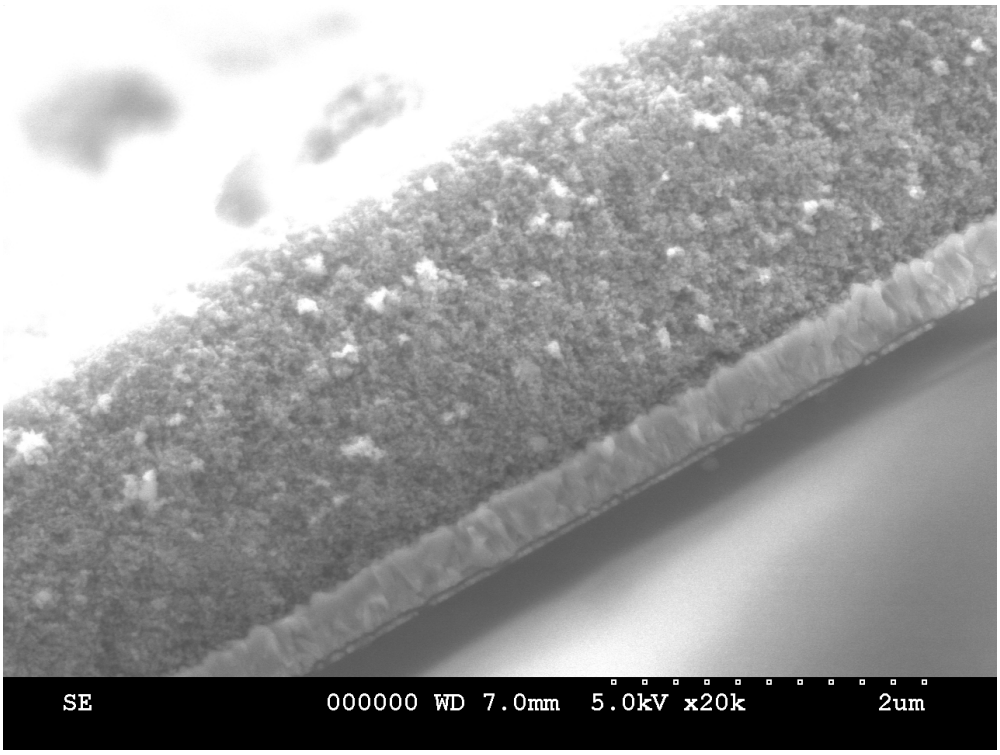

Figure 2.3: SEM image of a titania mesostructure prepared by screen printing. Note the thinner, lighter band representing the compact layer, as prepared by spray pyrolysis.

The paste is prepared differently to that which is doctor bladed, with the initial Dyesol TiO_2 paste having tepineol added as the primary solvent instead of ethanol. A fixed space mesh is 'loaded' with paste through transverse applied pressure after which the paste is then printed onto the surface of the prepared FTO by a second application of transverse pressure. A mesostructure typifying this preparation method is illustrated by the scanning electron micrograph (SEM) image given in figure 2.3. The mesostructures produced by screen printing and doctor blading are, despite the slightly different fabrication routes, entirely comparable in terms of final structure and electronic properties, with the screen print route representing a consistent yet wasteful method often used for larger runs while doctor blading can be more precise in terms of materials used and proves more adaptable.

Titanium Tetrachloride Surface Treatment

Substrates are immersed in a $TiCl_4$ solution (20mM in H_2O) for 60 minutes at 70°C, rinsed with deionised water and resintered to 500°C.

Dye Fabrication and Mesostructure Dye Loading

The actual fabrication of photoactive dyes is extremely complex, generating many theses every year in its own right, and it is therefore considered beyond the remit of this work to give more than a cursory outline of some of the most common dyes and their properties. Dye synthesis methods relevant to the work of this thesis will be referenced in full, except in the case that the molecule has been received through collaborators and is as yet unpublished. In can be noted that the appendix A.1 contains a full list of dye molecules used in the preparation of this thesis. Since the inception of DSCs there has been vast amount of work into fabricating dye molecules which can both absorb incoming light efficiently as well as allow the effective separation of charge carriers. The possibility of dissociating the photoabsorptive and carrier injection properties of dye molecules into a multi-dye system is considered extensively in chapter 3. In the majority of the early dye-sensitized devices the dye molecules were centred around a metal core that often resulted in dyes with broad absorptive properties whose absorption coefficients demanded relatively thick path lengths through the dye before complete (or near-complete) light extinction could occur.[10] This was not a significant barrier in the production of electrolyte based DSCs, however the later realisation of solid state electrolytes and subsequent requirement for thinner substrates made the relatively low absorption coefficients a limitating factor to overall device performance. Further to this, and perhaps more significantly, the rarity of the metals comprising the core of these molecules has led to increased interest in metal-free organic dyes whose absorption tends to be stronger but more spectrally constrained. Dyes are dispersed into solution, typically a 1:1 mix of acetonitril and tert-butanol, and the mesostrucured substrates are immersed in this solution for a pre-defined time, often on the scale of 1 hour for organic dyes and 18-24 hours for ruthenium dyes. Any note of dye loading within this thesis will be accompanied by concentration and immersion times.

Molecular Hole Transporter Synthesis and Application

Imediately after the dye loading process the devices are spin cast with Spiro OMeTAD (10-20% by weight in chlorobenzene, dependant upon film thickness); the hole transport medium (HTM) is applied to the stationary substrate with a pause before acceleration to promote infilitration. The devices are spun at between 1200-1500rpm depending on the thickness of substrate to provide a homogeneous top surface for the devices with a HTM cap of 50-100nm beyond the infiltrated mesostrucure. Substrate pore filling by this method has been estimated at 60-65%.[11] The molecular structure of Spiro OMeTAD is illustrated in figure 2.4.

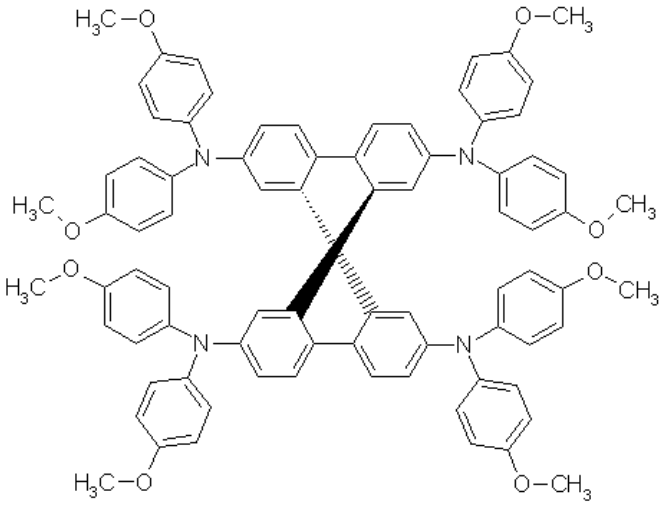

Figure 2.4: 2,29,7,79-tetrakis(N,Ndi-p-methoxyphenyl-amine)9,99-spirobifluorene (Spiro OMeTAD, often 'spiro') molecule.[?] Spiro is the HTM most regularly used in solid-state devices and is used exclusively in this thesis for sDSCs.

Evaporative Metal Contact Fabrication

Devices infiltrated and capped with the HTM are then appended contacts via evaporative metal application. Typically an optically thick contact of gold or silver (depending upon necessary stability[7]) is thermally evaporated against masked devices in a vacuum chamber at between 10^{-6} and 10^{-7} mBar. Devices produced in this thesis were contacted using an Edwards Auto 306 evaporator. At this point the devices are fully assembled and are ready for characterisation, although the contacts are in many cases electrically reinforced with Agar silver electrodag paint.

Figure 2.5 illustrates the final appearance of a fully fabricated solid state DSC, while figure 2.6 shows a photograph of the equivalent architecture of a real device.

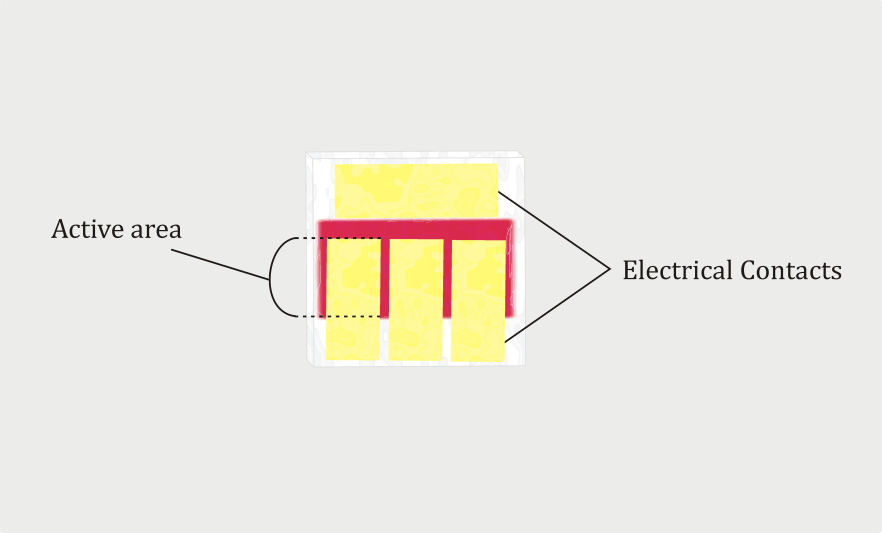

Figure 2.5: Graphic illustrating the appearance of a typical solid state DSC. The red, active area represents the dyed mesostructure atop a titania compact layer on FTO glass, infiltrated with HTM and topped with evaporative metal contacts.

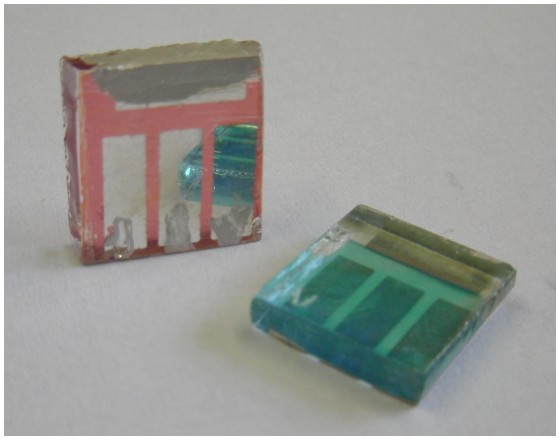

Figure 2.6: Two solid state dye sensitized solar cells fully-fabricated as outlined within this chapter. The left device incorporates the dye D102 whilst the right incorporates TT1, the different colours arising from the contrasting absorption spectra of the dye molecules adsorped.

2.3 Electrolyte Dye Sensitized Solar Cell Production

In addition to the solid state devices, a number of electrolyte devices were also fabricated for this thesis and a simple outline of their synthesis method follows. The elctrolyte design utilises opposing contacts rendering the FTO etch unnecessary. Otherwise the substrates are fabricated and treated in an identical manner to solid-state DSCs until the stage of the hole transport infiltration when, immediately following the removal from dye the substrate is counterfaced with a second conducting glass layer. Another layer of FTO glass is heat treated with chloroplatinic acid (50μM), to platinise the surface and form a transparent Pt counter electrode. The glasses are sealed together using a Surlyn stencil which is heat sealed to semi-permanently bind the two layers; a liquid electrolyte (typically an iodide-triodide redox couple [12]) is vacuum injected between the layers to infiltrate the mesostructure and the injection point sealed. At this point a glass microscope slide is affixed to device surface to prevent leakage using themosetting Binar plastic. The devices are characterised similarly to the solid state counterparts, with the differing device architecture taken into account.

Figure 2.7 illustrates the final appearance of a fully fabricated liquid phase DSC, while figure 2.8 shows a photograph of the equivalent architecture of a real device.

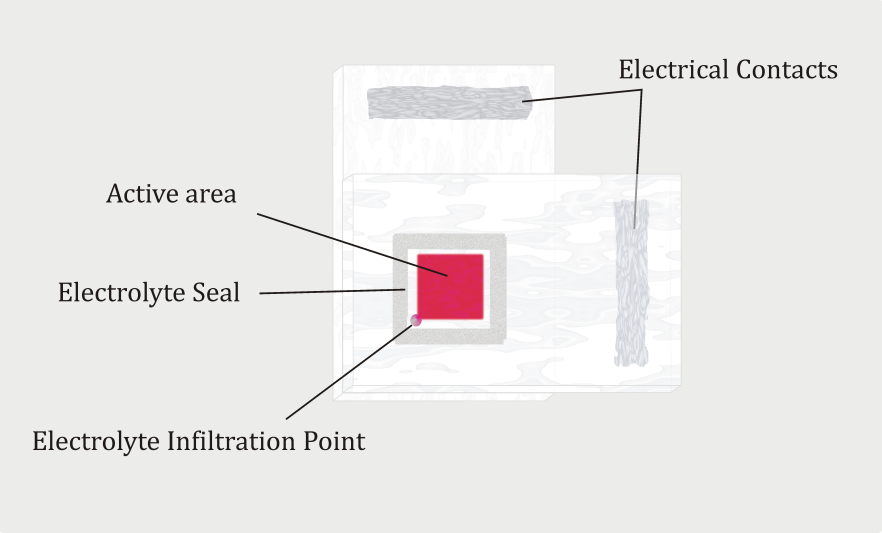

Figure 2.7: Graphic illustrating the appearance of a typical electrolyte DSC. The red active area represents the dyed mesostructure atop a titania compact layer on FTO glass, infiltrated with a liquid electrolyte, opposed and sealed with a platinized glass counter electrode.

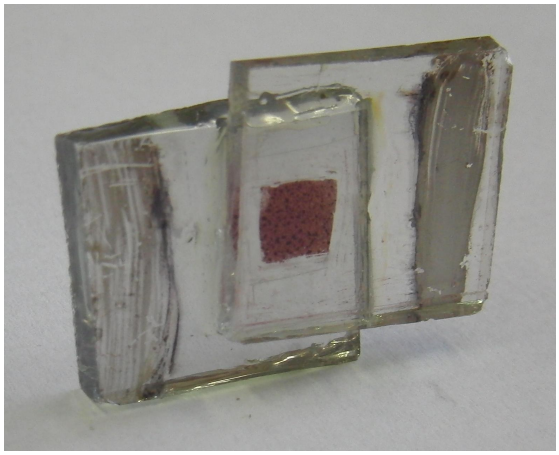

Figure 2.8: A fully-fabricated electrolyte dye-sensitized solar cell; in this case incorporating N719 [13] and sealed with the robust electrolyte.[12]

2.4 Device Characterisation

This section documents the most regularly used methods of device characterisation in the preparation of this thesis. Any further routes to characterisation not found within this section will be described at the pertinent juncture.

2.4.1 Current-Voltage and Photoconversion Efficiency Calculation

Typically a solar cell's performance is measured using a current - voltage plot (sometimes IV or JV, from current-density), from whence the peak power output and so photoconversion efficiency can be derived. For a more comprehensive exploration of the electronics (and action of semiconductor based solar cells) there are a number of specialised textbooks dealing with the topic such as Nelson's Physics of Solar Cells.[14] Solar cells under dark conditions perform electronically in an identical manner to a traditional diode, as depicted in figure 2.9.

In the case of solar cells under light conditions, the generation of photocurrent shifts the plot as shown in figure 2.10, the current-voltage characteristic of a light soaked photodiode.

It is worth observing that, typically, the current-voltage characteristic of a cell can be approximated by the addition of the short circuit current (J_{SC}) to the dark-IV response of the device. As such, to rephrase the ideal diode equation, the current density as a function of voltage can be denoted as:

$$J = J_{SC} - J_0(e^{qV/nk_BT} - 1) \tag{2.2}$$

Where q is the elementary chargem k_B is the Boltzmann constant, T the absolute temperature and n is the diode ideality factor. The resistance losses in solar cells can usually be categorised between series and parallel losses. Series losses occur due to the resistance of the device materials themselves to the generated photocurrent. Parallel losses (often termed shunt resistances) are generated by the architecture of the devices themselves, which can sometimes house routes for dissipation of generated photocurrent. These resistances as separate entities are more often observed in more developed solar technologies and in DSCs are often juxtaposed to the extent of being difficult to separate.

The maximum power point notations of figure 2.11 are predominantly used in modular PV arrays where the integration into a grid or other electrical system requires the consideration of

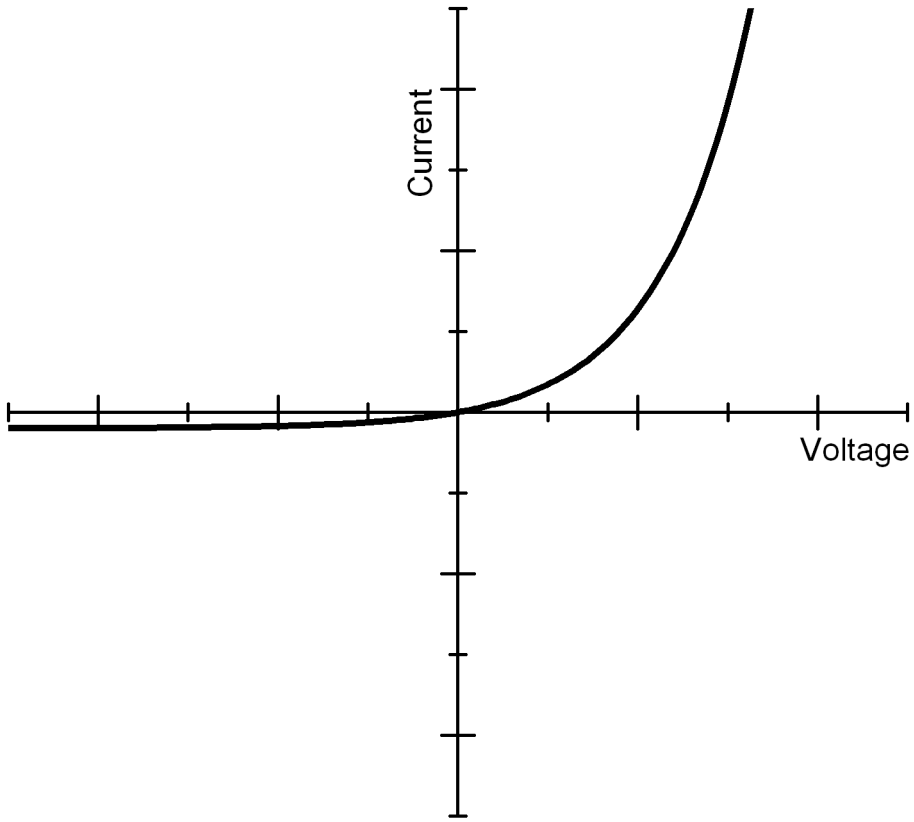

Figure 2.9: Typical diode response upon current-voltage characterisation. This response directly coincides with that of a solar cell under dark conditions.

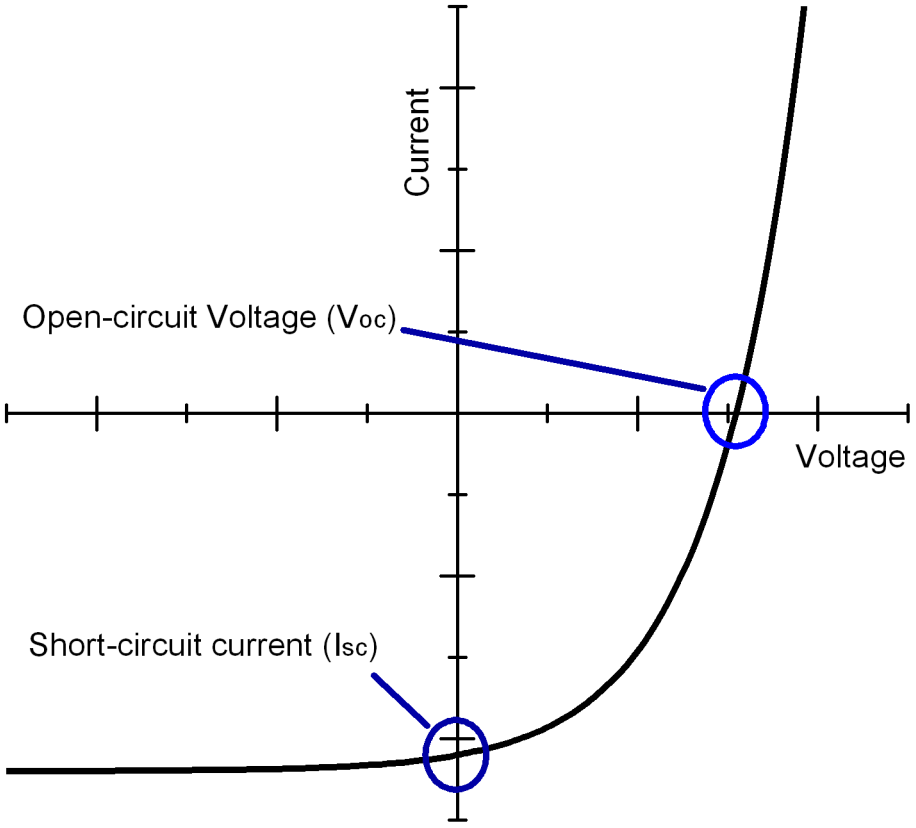

Figure 2.10: Simplified solar cell current-voltage characterisation showing short circuit photocurrent (I_{SC}) open circuit voltage (V_{OC}). Typically, for the purposes of comparison the current density (J) is plotted against voltage as this allows intepretation to be made independent of the area of the device.

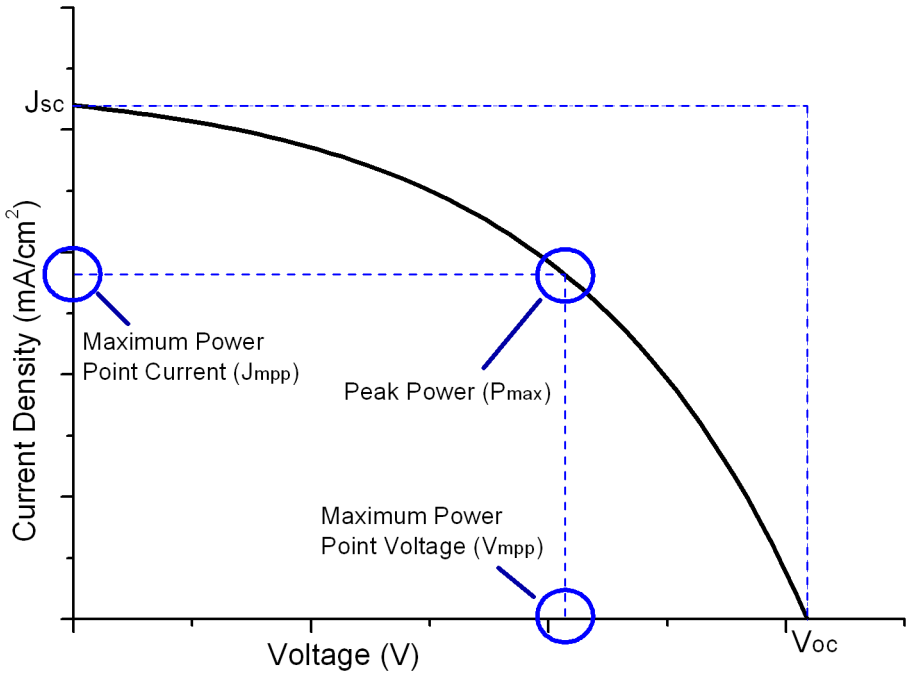

Figure 2.11: The fourth quadrant of a hypothetical current density-voltage curve is rotated into the traditional x-y axis format to allow ease of analysis. This arrangement is regularly used to interpret solar cell performances and all further current-density against voltage (JV) plots can be assumed to be arranged in this fashion unless otherwise stated.

electrical factors such as impedance matching. Between the limits of 0 and V_{OC} the solar cell delivers power as:

$$P = JV \tag{2.3}$$

The power variation and hence maximum power point can be more clearly observed by the adaption of this curve to display power against voltage, as figure 2.12. In this case the power rises with the voltage as the current stays largely constant; eventually the current begins to drop more precipitously, resulting in the power output of the device diminishing once again. The discrepency between the J_{SC} and V_{OC} and the J_{mpp} and V_{mpp} respectively, gives rise to the notion of the fill factor (FF) defined as:

$$FF = \frac{J_{mpp}V_{mpp}}{J_{SC}V_{OC}} \tag{2.4}$$

and is often seen as a measurement of the 'squareness' of the JV curve. The efficiency (η) of the device is governed as:

$$\eta = \frac{J_{mpp}V_{mpp}}{P_{inc}} \tag{2.5}$$

where P_{inc} represents the total incident light power flux. From this it is easily observed that the efficiency is also related to J_{SC} and V_{OC} through the Fill Factor (FF):

$$\eta = \frac{J_{SC}V_{OC}FF}{P_{inc}} \tag{2.6}$$

All devices outlined in this thesis that are noted to have had current - voltage characterisation were measured using a system designed in house illuminated by a spectrally matched ABET Technologies, class AAB, Sun 2000 Solar Simulator, measured by a Keithley 2400 sourcemeter and a number of bespoke Labview programs, callibrated against a NREL certified, KG5 filtered silicon reference diode. Figure 2.13 shows a simplified layout of this system. The applied voltage is scanned while the resultant photocurrent is measured and, from the known masked area of the devices, the photocurrent density. From these measurements the short-circuit current density (J_{SC}), open-circuit voltage (V_{OC}), fill factor (FF) and efficiency (η) of the device can be derived.

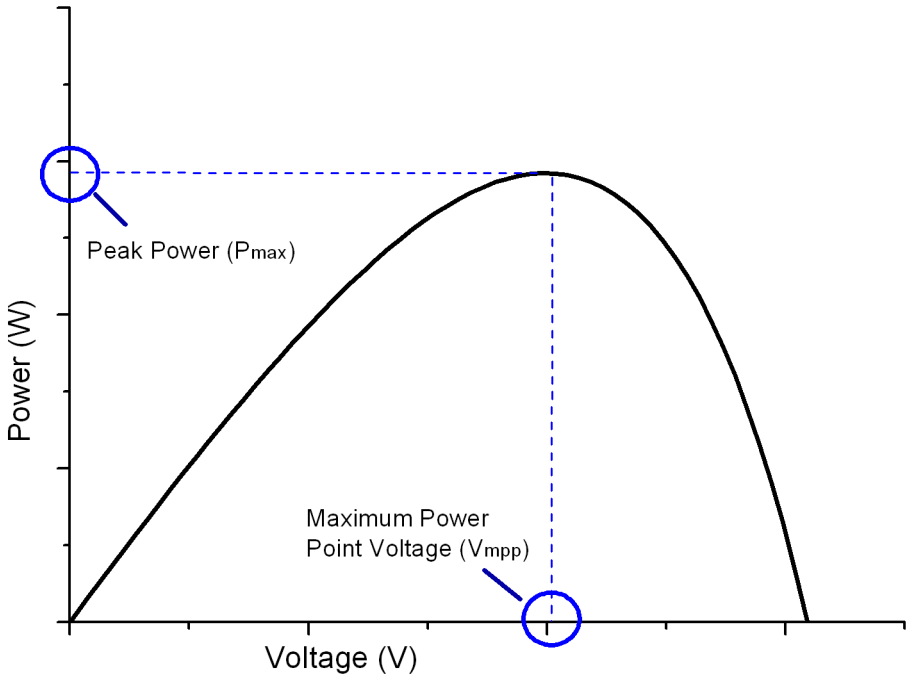

Figure 2.12: Power-voltage curve in equivalence to the current-voltage curves noted in figure 2.11. Upon derivation of the power from current and voltage, the power variation as a function of voltage is more clearly observed.

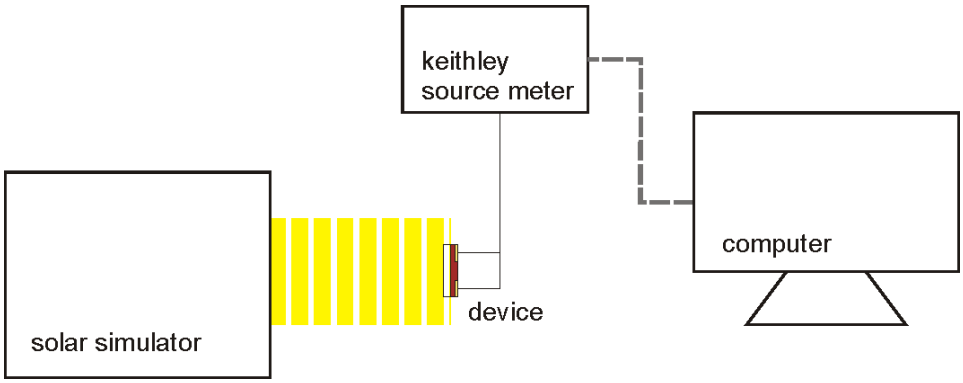

Figure 2.13: Simplified layout of solar simulation system measuring photoconversion efficiency. Devices are masked to accurately control photoactive area. The lamp intensity is callibrated against a known reference diode - an NREL certified, KG5 filtered silicon reference diode.

2.4.2 Spectral Response

The spectral response system designed and built by the author consists of a Princeton Instruments Acton SP2150i monochromator powered by an attached TS428 model Princeton Instruments 250W lamp which is used to illuminate devices housed in a self-made device holder array which allows the measurement of up to 48 devices chosen by a National Instruments NI SCXI-1000 channel selection system with a NI SCXI-1331 bolt-on; upon channel selection, the signal of the device is measured by a Keithley 2400 sourcemeter. The whole system is controlled by a National Instruments Labview program designed and written for this purpose. The composition of the system is documented in figure 2.14.

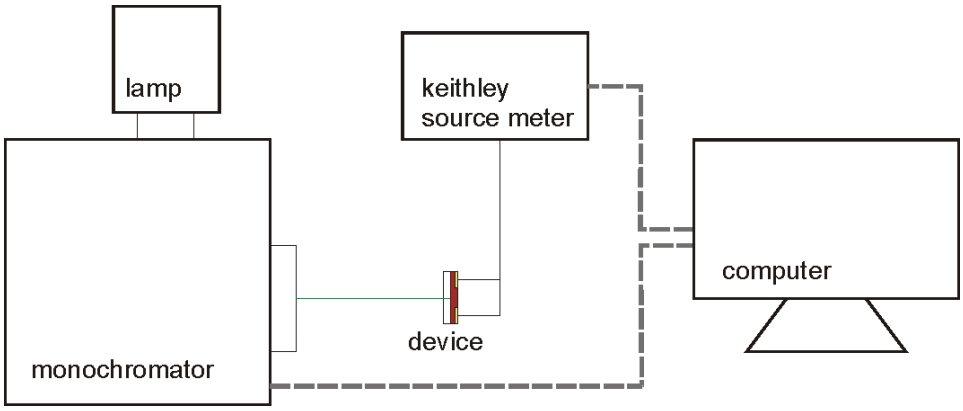

Figure 2.14: Simplified layout of spectral response system measuring external quantum efficiency as a function of wavelength. Devices are masked to accurately control photoactive area. The system is callibrated against a known responsivity of a Centrionic Series 7 OSD5.8-7 UV matched photodiode.

The external quantum efficiency (EQE) of the devices is callibrated from the known responsivity of a Centrionic Series 7 OSD5.8-7 UV matched photodetector. In direct terms the EQE can be derived as the ratio of photoexcited electrons to the number of incident photons, as:

$$\text{External Quantum Efficiency } (EQE) = \frac{\text{number of generated photoelectrons}}{\text{number of incident photons}} \tag{2.7}$$

or

$$EQE = \frac{\text{output current density}}{\text{input light flux}} \tag{2.8}$$

The ratio of generated photoelectrons to absorved photons is known as the *internal* quantum efficienct (IQE) and is often used an an indicator of the efficacy with which the devices utilise the generated photocurrent after absorption has occured.

$$\text{Internal Quantum Efficieny } (IQE) = \frac{\text{number of generated photoelectrons}}{\text{number of absorbed photons}} \tag{2.9}$$

and, as such, the internal quantum efficiency IQE can also be calculated as:

$$IQE = \frac{EQE}{absorptance} \tag{2.10}$$

As the absorptance will always limit between 0 and 1, the IQE must always be higher than the EQE. The difference between the IQE and EQE spectra can inform the understanding of the light uptake and use in the device. Both internal and extenal quantum efficiency figures are used extensively in this thesis to illustrate and clarify the interaction of incoming light and generated photocurrent in the devices studied. EQE is sometimes used interchangeably with incident photon-electron conversion efficiency (IPCE) and IQE with absorbed photon-electron conversion efficiency (APCE), although IPCE and APCE notation is purely a function of wavelength, while overall EQE and IQE for complete spectra are sometimes discussed.

2.4.3 Surface Profilometry

A Veeco Dektak 150 surface profilometer was used regularly during the prepartion of this thesis for mesostructure thickness and homogeneity measurements, HTM cap thickness measurements and evaporative metal contact thickness calibration. More qualitative surface and cross section profiling was also undertaken using scanning electron microscopy (SEM), as exampled by figure 2.3. The SEM used for these measurements is a Hitachi S-4300 field emission scanning electron microscope.

2.4.4 UV-Visible Spectrophotometry

Simple optical characterisation of both films and completed devices was achieved using a CARY 300 Bio UV-Visible spectrophotometer, which provides absorbance measurements as well as, with an integrating sphere attachment,[15] reflectance and transmission measurements. The absorbance (optical density) can be related to the ratio of incident radiative flux to transmitted flux from the Beer-Lambert law as:

$$A_\lambda = -log_{10}\left(\frac{I_0}{I}\right) = -log_{10}\left(\frac{1}{T}\right) \tag{2.11}$$

Where A_λ is the absorbance of the sample, I_0 is the total incident light flux, I is the transmitted flux and T is the transmission. The application of equation 2.11 assumes that *all* transmitted light is detected while most real systems will measure specular transmission and off-specular transmission separately. The use of angled facets and the integrating sphere allows the determination of the specular and off-specular aspects of both reflectance and transmission.

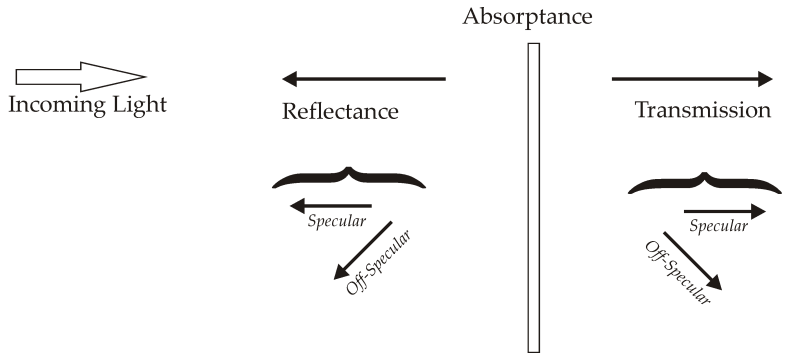

Figure 2.15: Relating absorptance (A), reflectance (R) and transmission (T). The R and T values are composed of specular and off-specular elements, which correspond to direct and scattered respectively.

Note that absorptance is subtly distinguished from absorbance as the direct ratio of radiant flux absorbed to that which is incident. This allows us to logically relate the reflectance, transmission and attenuation:

$$R + T + A = 1 \tag{2.12}$$

But, more completely, these variables can be separated into their specular and off-specular values and so figure 2.15 can also be clarified as:

$$(R_{specular} + R_{off-specular}) + (T_{specular} + T_{off-specular}) + Absorptance = 1 \tag{2.13}$$

Fully fabricated devices are typically silver contacted, providing a functional mirror backing the device which provides unattenuated light with a second pass with which to contribute to the photoharvesting of the device.

References

[1] E. a. Gibson, A. L. Smeigh, L. Le Pleux, J. Fortage, G. Boschloo, E. Blart, Y. Pellegrin, F. Odobel, A. Hagfeldt, and L. Hammarström, "A p-type NiO-based dye-sensitized solar cell with an open-circuit voltage of 0.35 V.," *Angewandte Chemie*, vol. 48, pp. 4402–5, Jan. 2009.

[2] a. Nattestad, A. J. Mozer, M. K. R. Fischer, Y.-B. B. Cheng, A. Mishra, P. Bauerle, U. Bach, and P. Bäuerle, "Highly efficient photocathodes for dye-sensitized tandem solar cells," *Nature Materials*, vol. 9, pp. 31–35+, Jan. 2010.

[3] P. Docampo and H. J. Snaith, "Obviating the requirement for oxygen in SnO2-based solid-state dye-sensitized solar cells.," *Nanotechnology*, vol. 22, p. 225403, June 2011.

[4] P. Tiwana, P. Docampo, M. B. Johnston, H. J. Snaith, and L. M. Herz, "Electron Mobility and Injection SnO 2 , and TiO 2 Films Used in Dye-Sensitized Solar Cells," *ACS Nano*, vol. 5, no. 6, pp. 5158–5166, 2011.

[5] M. Boucharef, C. Di Bin, M. S. Boumaza, M. Colas, H. J. Snaith, B. Ratier, and J. Boucle, "Solid-state dye-sensitized solar cells based on ZnO nanocrystals," *Nanotechnology*, vol. 21, p. 205203, 2010.

[6] K. Kalyanasundaram, *Dye-sensitized Solar Cells*. CRC Press, 1 ed., 2010.

[7] H. J. Snaith, R. Humphry-Baker, P. Chen, I. Cesar, S. M. Zakeeruddin, and M. Gratzel, "Charge collection and pore filling in solid-state dye-sensitized solar cells," *Nanotechnology*, vol. 19, p. 424003, 2008.

[8] L. Kavan and M. Grätzel, "Highly efficient semiconducting TiO2 photoelectrodes prepared by aerosol pyrolysis," *Electrochimica Acta*, vol. 40, 1995.

[9] C. J. Barbe, F. Arendse, P. Comte, M. Jirousek, F. Lenzmann, V. Shklover, and M. Gra, "Nanocrystalline Titanium Oxide Electrodes for Photovoltaic Applications," *J. Am. Ceram. Soc.*, vol. 71, pp. 3157–3171, 1997.

[10] M. D. Brown, T. Suteewong, Kumar, V. D'Innocenzo, A. Petrozza, M. M. Lee, U. Wiesner, and H. J. Snaith, "Plasmonic Dye-Sensitized Solar Cells Using Core-Shell Metal-Insulator Nanoparticles," *Nano Letters*, vol. 11, pp. 438–445, Feb. 2011.

[11] I. K. Ding, N. Tetreault, J. Brillet, B. E. Hardin, E. H. Smith, S. J. Rosenthal, F. Sauvage, M. Gratzel, and M. D. McGehee, "Pore-Filling of Spiro-OMeTAD in Solid-State Dye Sensitized Solar Cells: Quantification, Mechanism, and Consequences for Device Performance," *Advanced Functional Materials*, vol. 19, pp. 2431–2436, 2009.

[12] P. Wang, C. Klein, R. Humphry-Baker, S. M. Zakeeruddin, and M. Gratzel, "Stable >8% efficient nanocrystalline dye-sensitized solar cell based on an electrolyte of low volatility," *Applied Physics Letters*, vol. 86, no. 12, p. 123508, 2005.

[13] Y. Tachibana, K. Nazeeruddin, M. Gr, D. R. Klug, and J. R. Durrant, "Electron injection kinetics for the nanocrystalline TiO2 films sensitised with the dye (Bu4N)2Ru(dcbpyH)2(NCS)2," *Chemical Physics*, vol. 285, pp. 127–132, 2002.

[14] J. Nelson, *The Physics of Solar Cells (Properties of Semiconductor Materials)*. Imperial College Press, 2003.

[15] H. J. Snaith and C. Ducati, "SnO2-Based Dye-Sensitized Hybrid Solar Cells Exhibiting Near Unity Absorbed Photon-to-Electron Conversion Efficiency," *Nano Letters*, vol. 10, pp. 1259–1265, 2010.

Chapter 3

Molecular Coadsorption Leading to Unprecedented Surface Energy Transfer

---

This chapter discusses investigations into the extension of the spectral absorption range via the adsorption of more than one dye molecule with spectrally complimentary absorption profiles. Characterisation of device performance and subsequent quantum efficiency measurements indicate a performance increase greater than that likely due to simple spectral extension. Devices combining visible and near-infrared absorptive dyes are observed to attain photoconversion efficiencies in excess of 4.5%, with singly adsorped devices typically presenting around 3.5% and 1% respectively. An intermolecular resonant energy transfer process was speculated and photoluminescence studies were undertaken that led to the confirmation and characterisation of this process. The energy transfer efficiency was estimated by both theoretical and spectroscopic means and suggest a value of ~50%.

3.1 Spectral limitations of solid-state dye-sensitized solar cells

Solid-state DSCs (sDSCs) using molecular hole-transporters are an attractive alternative to liquid electrolyte based cells, but efficiency is limited to a large extent by poor light harvesting, both in extinction strength and bandwidth.[1] This is in contrast to semiconductor based photovoltaic technologies, where the absorption profile is driven by the band-gap of the semiconductor. This is most often illustrated by silicon PV, where the spectral response of silicon diodes typically follows a flatish shape through the visible portion of the spectrum before abruptly cutting off at around 1060nm, equivalent to the 1.1eV bangap of silicon itself.[2] The spectral response of a typical silicon diode is displayed in figure 1.2 of chapter 1 and illustrates this typical semiconductor shape.

The bandgap limitations of semiconductor PV gave rise to the idea of multijunction devices - as previously noted in Chapter 1. This use of multiple semiconducting materials allows the absorptive properties of the devices to be extended spectrally, based on the bandgaps of the various materials used and is therefore subject to a detailed balance limit imposed by a theoretical stacked device composed of three tandem layers of around 49% [3] although in practical terms the limit is likely to be significantly lower. Tandem devices are dependant upon the matching of electrical characteristics as well as the spectral ranges of the absorber. In this work only the concept of extending the spectral range through multiple absorptive materials is here applied to DSCs and the subsequent results are outlined and analysed, no overt attempt is made to control the electronic matching as devices are composed of only a single complete layer.

In sDSCs the film thickness is limited by the necessity for mesostructure infiltration by a molecular hole transporter, which can typically be effective up to substrate thicknesses of around 2μm, beyond which the pore filling proves inefficient and a shorter electron diffusion length dominates.[4] Due to the apparently inefficient pore filling of structures over 2-4 μm thick, optimizing absorption is critical in sDSCs and poses a significant challenge to dye chemists who must balance (and aim to idealise) the absorptive, adsorptive and injection characteristics of these dyes.

Some work has been done in the implementation of a nearly direct transfer of this multijunction concept, with layered tandem DSCs. These devices would comprise of a number of

layers (subcells), each containing a largely optimized DSC and each contributing to the current generation, matching the voltage of each dye layer, forming a number of distinct 'subcells'.[5,6] This would ideally be composed of a series of independent solar cells that would be required to be electronically matched to offer optimum efficacy. Despite the promise that this concept holds, no devices known to the author have been fabricated that exceed the performance capabilities of devices fabricated in the orthodox fashion. Hybrid tandem devices incorporating a dye-sensitized subcell with a higher performance Cu(InGa)Se (CIGS) subcell have been produced that improve on the efficiency of both subcells singly, but do not exceed the efficiency of the best CIGS devices.[7]

The more established sensitizers, usually based on a ruthenium centre such as Z907,[?] N719 [8] and N3,[9] tend to have a broad absorption profile with a relatively low extinction coefficient which sufficient for use in electrolyte devices incorporating thicker substrates, but is not ideal for solid state devices, whose solid state HTM nature demands a thinner metal oxide. This is in contrast to organic sensitizers such as the indoline based D012 [10] and D131 [11], the pthalocynanine based TT1 [12] and the squaraine based SQ02.[13] Note that the structures of all the dyes used within this work are illustrated in appendix A.1.

The coadsorption of complementary dyes has been shown to be promising for extending the photovoltaic response in electrolyte based cells,[?] but should be considerably more advantageous for sDSCs, where the limited extinction pathlength means that the optimization of light harvesting is critical. This chapter reviews the work heretofore done on multi-dye systems and then discusses the work undertaken on the topic in the preparation of this thesis.

3.2 Cosensitization of spectrally complementary dyes

Here, it is sought to extend the absorption spectrum of spiro-OMeTAD (spiro) based sDSCs by the cosensitization of a visible light absorbing indoline based organic dye, termed D102,[10,14] with a near-IR absorbing Zn-phthalocyanine dye, termed TT1.[12,15,16] SDSCs incorporating the indoline sensitizer exhibit a full sun conversion efficiency of 3.9%, incorporating the Zn-phthalocyanine sensitizer they exhibit 1.1%, and remarkably this is enhanced to 4.7% with an optimized cosensitized system. This by itself is noteworthy, but furthermore it is observed that the improvements with cosensitization amount to more than that expected from the superior

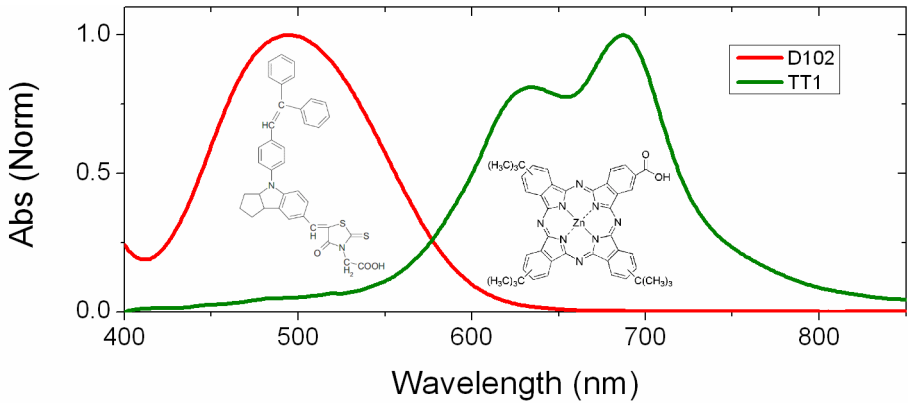

Figure 3.1: Absorption spectra for D102 and TT1 adsorped to 1.8μm TiO_2 films. Spectra are normalised for ease of spectral comparison.

light harvesting. Through photoluminescence investigations it is demonstrated that resonant energy transfer occurs from the visible absorbing dye to the Near IR sensitizer. The previously unobserved surface energy relay reported proves to be a more efficient channel for charge generation in this system than direct electron transfer from the photoexcited visible dye.

The cosensitization route outlined within this chapter ultimately improves the current density further still to 9.4 $mAcm^{-2}$, with the overall powerconversion efficiency improved to 4.7%, which is, at the time of record, the highest reported full sun efficiency for a SDSC incorporating an organic sensitizer.

3.2.1 Contemporary Literature

There has been some contemporary work detailing experiments with multi-dye systems that have illustrated spectral extension with the use of complimentary dye molecules.[?] Recently there has been some suggestion, concurrent to this work, that energy transfer can be achieved within DSCs with the use of a two-dye system with the energy transfering dye (referred to as the 'relay dye') being suspended within the electrolyte.[?] This was furthered later by a documented cosensitization of a two dye system in electrolyte devices,[17], published at the same time as the work outlined within this chapter. To the author's knowledge, the direct cosensitization of complimentary dyes had not been applied effectively to sDSCs prior to this work. In a comparable work, Driscoll et al have recently published work documenting an energy transfer process occuring

	Current (mA)	Voltage (mV)	Fill Factor (%)	Efficiency (%)
D102	7.82	800	61.4	3.85
SQ02	3.56	640	46.2	1.05
Cosensitized	8.08	800	64.8	4.19

Table 3.1: Typical photovoltaic characteristics of D102, SQ02 and cosensitized devices

between an altered Spiro OMeTAD complex (2,2',7,7'-tetrakis(3-hexyl-5-(7-(4-hexylthlophen-2-yl)benzo[c][1,2,5]thiadiazol-4-yl)thiophen-2-yl)-9,9'-spirobifluorene, known as spiro-TBT) and the pthalocyanine molecule TT1.[18]

3.3 Device fabrication

3.3.1 Squaraine-Indoline cosensitization

Solid state DSCs were prepared and characterized in a manner broadly consistent with the methods outlined in Chapter 2. Initially a number of devices were fabricated incorporating singly sensitized indoline (D102) [10] or squaraine (SQ02).[13] The D102 sensitization was optimised for a 1 hour immersion (0.2mM ACN:tert-Butanol 1:1) and the SQ02 for 30 minutes (20μM ethanol). Following this optimisation both of the dyes were dispersed into the some ethanol solution at the same molar concentration as their use singly and the resulting dual-dye solution used to sensitize similarly thick (1.8μm) titania films. The resulting sensitized films were completed as fully functional sDSCs and their performance characteristics were measured and are noted in table 3.1.

The current-voltage characteristic for these devices shows a typical sDSC performance for D102 and SQ02. Upon cosensitizing them on the same film a current is attained higher than either, initially deemed to be due to the extension of the spectral range from either dye's photoresponse individually. The enhancement in current density, with no detriment to either the V_{OC} or fill-factor, subsequently confers a significant increase in overall photoconversion efficiency, surpassing 4% and the performance of both the component dyes. The results observed in this investigation showed the promise of coadsorption as a means of enhancing photocurrent generation. Concurrent work with the pthalocyanine TT1 indicated that it may prove more

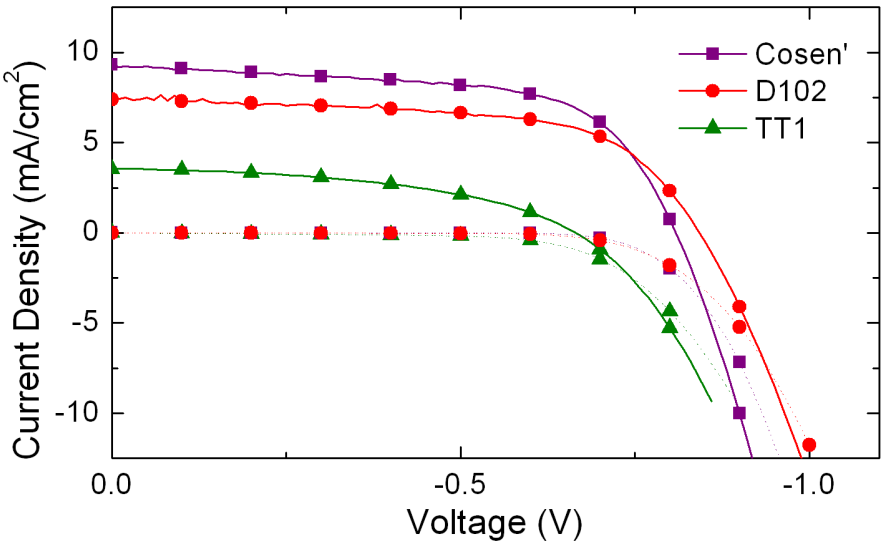

Figure 3.2: Current density-voltage (J-V) characteristics of SDSCs sensitized with D102 (circles), TT1 (triangles) and cosensitized with both D102 and TT1 (squares) measured under simulated AM1.5 sun light of 100 mWcm^{-2} and in the dark (same symbols with dotted lines).

efficient than SQ02 and, as such, further work on cosensitization was undertaken with the pthalocyanine acting as the near-IR component of the paired dyes.

3.3.2 Pthalocyanine-Indoline cosensitization

Single sensitizations to provide controls were performed with D102 for 1 hr (0.2mM ACN:tert-Butanol 1:1) and, on different substrates, TT1 for 1 hour (50μM in EtOH + 10mM chenodeoxycholic acid). For cosensitization the films were first sensitized with D102 for 48 minutes followed by TT1 for 12 minutes. Figure 3.2 shows current-voltage curves for sDSCs and table 3.2 notes their derived photovoltaic properties. Devices incorporating TT1 are observed to have a short-circuit current density of 3.5mAcm^{-2} and an efficiency of over 1%. Note that this performance is comparable with that previously reported for sDSCs incorporating Zn-phthalocyanines.[12] Devices incorporating D102 deliver a short-circuit current density of 7.6 mAcm^{-2} and convert 3.9% of the solar energy to electrical power, again, consistent with previous reports.[10]

In order to verify that the increased photocurrent in the cosensitized devices is due to increased light harvesting in the Zn-PC dye, spectral response measurements have been performed.

	Current (mA)	Voltage (mV)	Fill Factor (%)	Efficiency (%)
D102	7.6	840	61	3.9
TT1	3.5	660	47	1.1
Cosensitized	9.4	800	60	4.7

Table 3.2: Typical photovoltaic characteristics of D102, TT1 and cosensitized devices

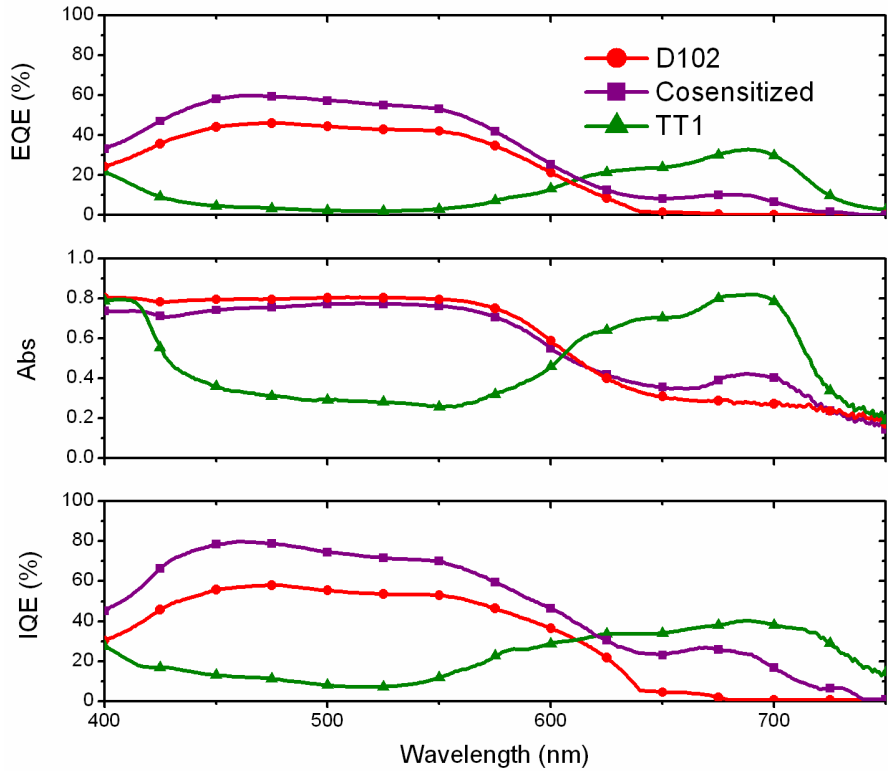

Figure 3.3: Quantum Efficiency Measurements for Co- and singly sensitized SDSCs. Photovoltaic action spectra for the same cells as presented in figure 3.2 showing external quantum efficiency (EQE - top), absorption (middle) and internal quantum efficiency (IQE - bottom). Note that the cosensitization dying times were optimized.

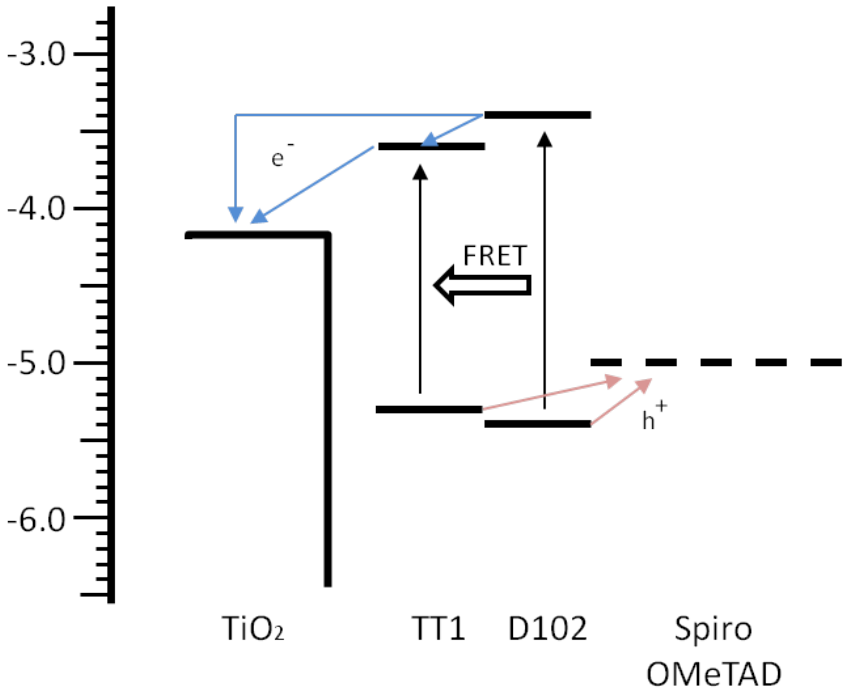

Figure 3.4: Energy level diagram for a two dye pthalocyanine-indoline system illustrating the apparent energy transfer route. Although no primary investigations of the energy levels of this system have been undertaken in the preparation of this thesis, contemporary literature suggests an energy level architecture for this system.[18–21] Blue and red lines indicate the possible routes of electron and hole injection respectively.

The photovoltaic action, presented in figure 3.3, does display an extension into the near IR for the cosensitized cell, as compared to "mono-sensitization" with D102, but the actual photoresponse in this extra IR region from 650 to 750 nm is relatively low. However, there is also an unexpected increase in the photo conversion efficiency in the visible region, where D102 already absorbs strongly. This suggests an altered energetic system, as illustrated in figure 3.4.

In order to disentangle the influence of enhanced light absorption, from improved operational processes, the absorbed photon-to-electron conversion efficiency (APCE) has been quantified. The light absorption in the device is estimated by measuring the reflectance spectra from silver backed devices in an integrating sphere,[22] and subsequently divided the IPCE by the fraction of light absorbed to determine the APCE (section 2.4.2). It is observed that the conversion

efficiency from the visible absorbing dye is panchromatically enhanced by the presence of the TT1 dye. Note a few peculiarities of the absorption spectra: for the TT1 only devices one would expect negligible absorption in the 450 to 550 nm region, however, from the reflectance measurements there is around 30% of the light absorbed in two passes of light through the film (reflectance). Furthermore, for the D102 only devices it would expected to see negligible absorption in the region >650nm, where actually around 20% absorption is measured in reflectance. This is likely to be due to partially oxidized spiro-OMeTAD, which absorbs in this region.[4] This implies that the APCE values derived are a lower estimation of the conversion efficiency from light absorbed in the dye, especially in the near IR region where the absorption from the sensitizer does not compete as strongly with the extrinsic absorptions than in the visible region of the spectrum.

3.4 Intermolecular energy transfer

The reason for the enhanced efficiency from D102, with the addition of the near IR absorbing Zn-PC sensitizer is not clear. However, the indoline based dyes (such as D102) are prone to aggregation and or formation of multi layers on the TiO_2 surface, and this may render electron-injection from photo-excited dye less than ideal.[?, 23] One possibility is that the co-sensitization process is breaking apart aggregates or desorbing non-bound dye. The TT1 dye solution contains approximately 2mM of chenodeoxycholic acid, specifically introduced to reduce aggregation of the TT1 molecules. To probe if this was also improving the D102, the D102 sensitized films were soaked in a 2 mM chenodeoxycholic acid solution for 12 minutes to mimic the effect under the co-sensitization process. In this instance however, no significant increase in photocurrent of the constructed solar cells is observed, indicating that the presence of the TT1 is directly influencing the photoinduced charge generation from light absorbed in the D102. It is postulated that energy transfer from D102 to TT1 could be responsible for enhancing the charge generation efficiency: If electron transfer from the photoexcited D102 is heterogeneous,[23] then the slower injecting species may not compete effectively with the natural decay of the excited state. If this "slow-injecting" phase can transfer its energy to the near IR dyes prior to exciton decay then this would, in essence, "recycle" the exciton and enable a second chance for electron transfer to the TiO_2 through the TT1 sensitizer. To probe whether surface energy transfer occurs in this system

time-resolved photo-luminescence (PL) measurements were performed on sensitized mesoporous TiO_2 and Al_2O_3 (the Al_2O_3 substrates acting as non-injecting references) substrates by time correlated single photon counting (TCSPC). The films were excited at 400nm under vacuum (further details of TCSPC are given in appendix A.2).

The photoluminescence spectra for D102, TT1 and co-sensitized films are shown in figures 3.5 and 3.6. D102 has a broad visible to near IR emission. On both TiO_2 and Al_2O_3, the visible emission from D102 is significantly quenched by cosensitization with TT1. The emission onset for the cosensitized film is almost identical to pure TT1, consistent with highly efficient energy transfer occurring from the emissive species in D102 to TT1. The PL spectra for D102 after soaking in an equivalent solution of CDCA was also measured; which, in contrast, shows a marginal increase in PL intensity and no change to the spectral shape. This confirms that CDCA does not play a significant role in quenching of the luminescence, though it may further aid energy transfer to the TT1 by increasing the PL intensity from the D102. It is noted that the light absorption in TT1 at 400nm is very weak and the absolute emission at 700 nm has increased ~10 fold in the cosensitized films as compared to pure TT1 sensitization. The PL tail observed in pure TT1 films is due to reduced sensitivity combined with very low emission signals. This is clarified by figures 3.5 and 3.6 The results on TiO_2 and Al_2O_3 follow the same trend though the overall PL intensity is higher on Al_2O_3 due to elimination of the electron transfer channel.

The transient PL decay curves for sensitized Al_2O_3 are shown in figure 3.7, while figure 3.8 illustrates the ratios of decay of the two dyes between their singly and coadsorbed states and the correlation between the two suggesting a direct energy transfer process. The D102 emission (at 650nm) decays significantly faster in the cosensitized film than in the mono-sensitized film. The TT1 PL (at 705nm) decays faster in the mono-sensitized film than when cosensitized with D102. This is consistent with excitation energy transferring from D102 to TT1 by dipole-dipole interactions, "replenishing" the TT1 excitons as they undergo their natural decay, slowing down the overall observed decay. The PL decay trends are identical, the decays are faster on TiO_2 than on Al_2O_3 consistent with electron transfer to the TiO_2. Importantly here, the D102 emission decays significantly faster in the cosensitized film on TiO_2, indicating that long-lived D102 excited states contributing to the emission are more effectively quenched via energy transfer to TT1 than via electron transfer to TiO_2 for times longer than 10ps. The decay observed in

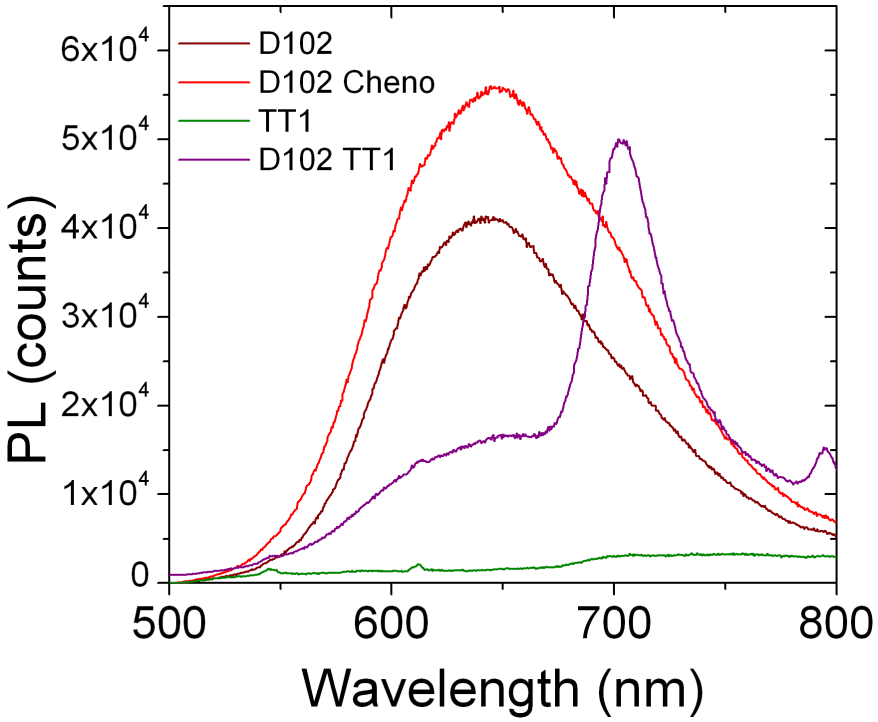

Figure 3.5: Photoluminescence spectra for relevant molecules singly and in various coadsorptive combinations. PL spectra performed on substrates resembling functioning devices on TiO_2 substrates. It can be noted that the effect of coadsorption of the spacer molecule with D102 only (optically matched to the spectral absorption profile of D102 singly at 500nm), results in no quenching of the PL spectra and, indeed, shows minor enhancement of the photoluminescent efficacy. This is in contrast to the PL spectra of substrates coadsorbed with both D102 and TT1 (again, optically matched at 500nm to D102 singly) which shows a significant quenching of the PL spectra in the visible, D102, range. The TT1 response is noted to be comparatively weak on the TiO_2 substrate, which is indicative of efficient charge injection into the metal oxide. This is confirmed by PL spetra observed on Al_2O_3 which shows a considerably enhanced response, this is shown in figure 3.6. The D102 panel also shows the time-resolved PL for D102 containing Substrates containing both chenodeoxycholic acid (CDA).

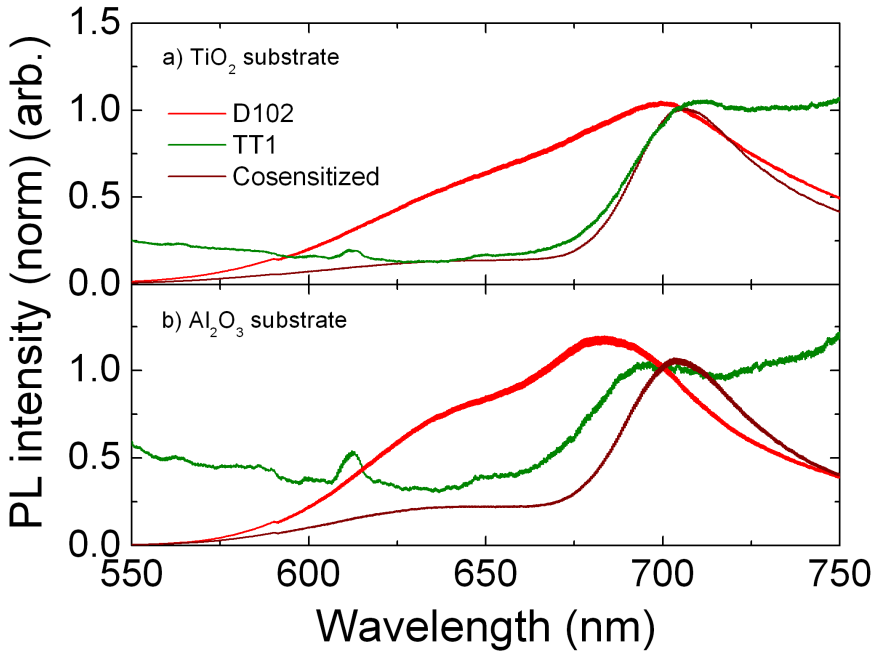

Figure 3.6: Normalised photoluminescence spectra for relevant molecules singly and in various coadsorptive combinations. PL spectra performed on substrates resembling functioning devices on TiO_2 and Al_2O_3 substrates (**a** and **b** frames respectively). Further to figure 3.5 the spectra is normalised to highlight the quenching of the PL in the visible range. Normalisation also clarifies the agreement of the TT1 peaks singly and under coadsorption, otherwise occluded by the relatively poor PL response of TT1 without normalisation. PL spectra performed on substrates resembling functioning devices.

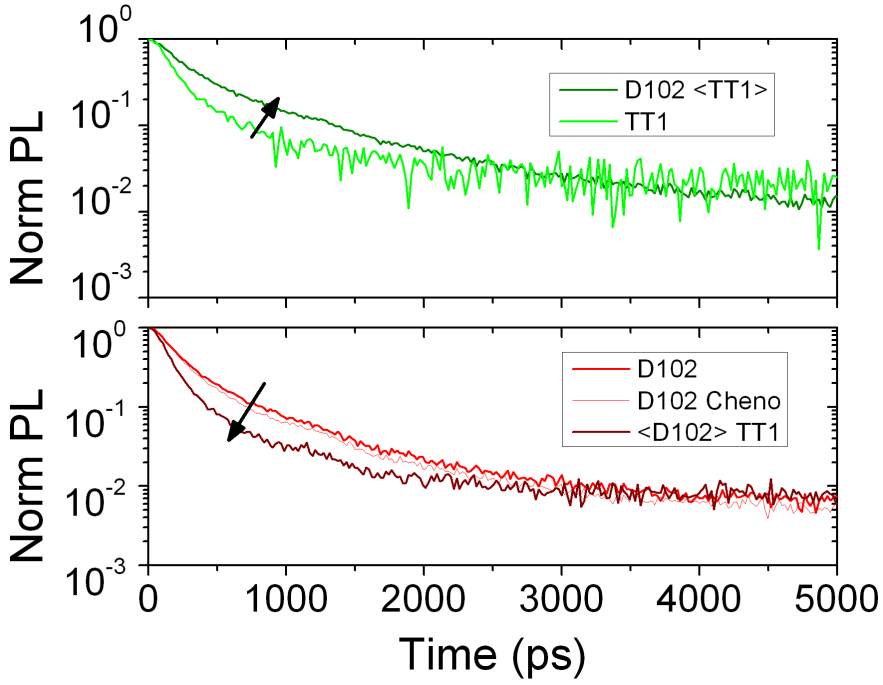

Figure 3.7: Normalised PL decay spectra for relevant molecules singly and in various coadsorptive combinations. Time-resolved photoluminescence from species at 705nm (TT1 - top, green) and 650nm (D102 - bottom, red) is shown for the case of mono-sensitized (light line) and cosensitized (dark line). All measurements were performed with Al_2O_3 as a substrate to avoid ambiguity due to electron injection. The arrows show the trend upon cosensitization. The D102 panel also shows the time-resolved PL for D102 containing chenodeoxycholic acid (CDA) in equivalent concentration to a cosensitized film (thin line).

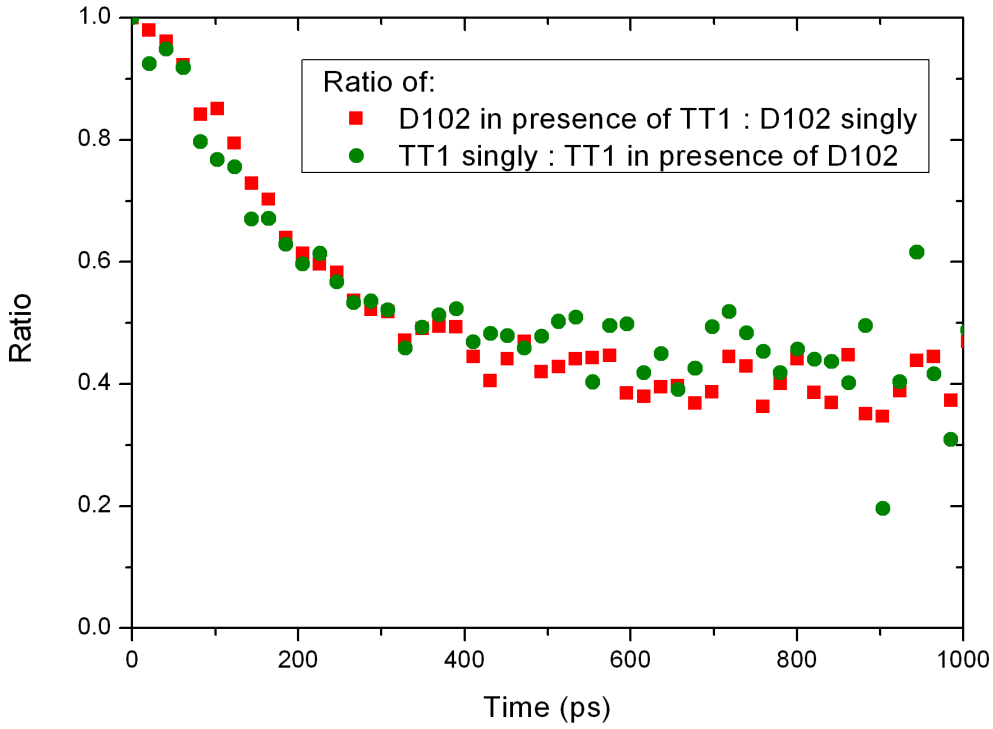

Figure 3.8: Ratios of PL emission for chromophores singly- and co-sensitized, on a device equivalent TiO_2 substrate. The ratio of emission from the 650nm species (D102) in the cosensitized to monosensitized films and, conversely, the ratio of emission of the 705nm species (TT1) in monosensitized to consensitized film. The decays are indicative of energy transfer, with an exponential life-time of 210ps (line).

figures 3.7 and 3.8 suggests an energy transfer lifetime of 210 ps.

3.4.1 Förster Resonant Energy Transfer Theory

Förster resonant energy transfer is the process by which energy can be transfered between adjacent molecules via dipole-dipole interactions. This is clarified by figure 3.9 which illustrates the energetic transitions associated with Förster and Dexter energy transfer. In these devices it is likely that both FRET and Dexter processes are occuring, but due to the PL decay effects observed in section 3.4 it is believed that the action of FRET is more significant.

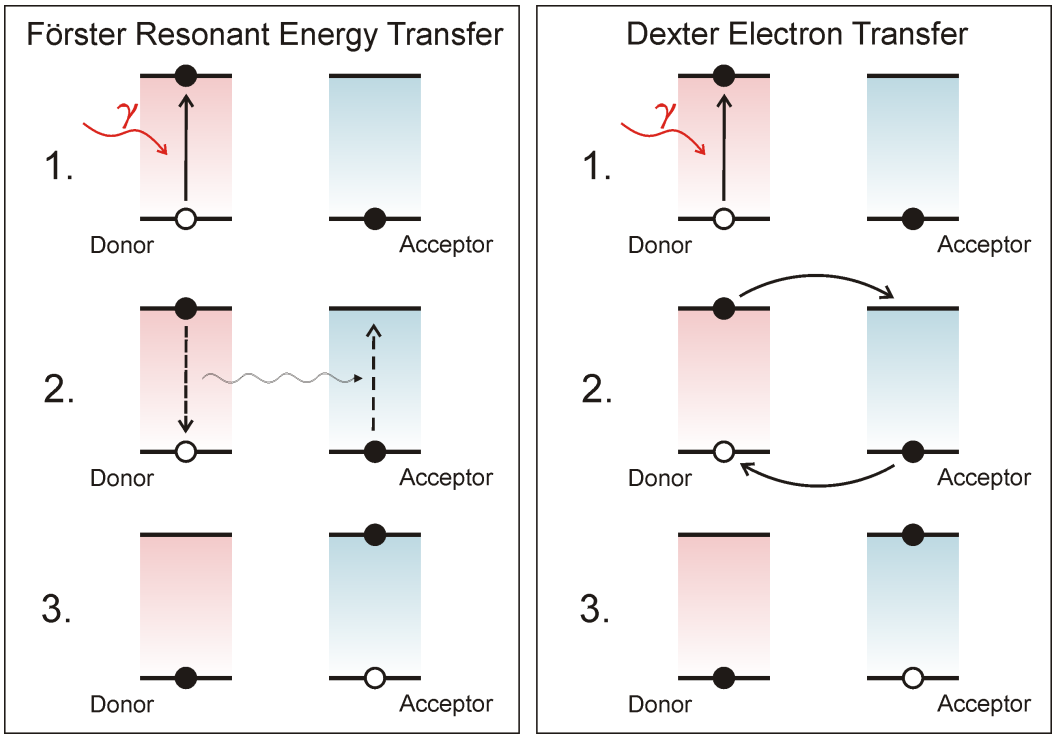

Figure 3.9: FRET and Dexter Energy Transfer Schematics. The left panel shows the energetics associated with FRET and the right shows those for Dexter electron transfer.

Förster resonant energy transfer: 1. donor excitation, 2. non-radiative donor relaxation, induced excitation in acceptor by FRET, 3. excited acceptor.

Dexter energy transfer: 1. donor excitation, 2. electron transfer - excited electron transferred donor to acceptor, ground state electron transferred acceptor to donor, 3. excited acceptor.

The Förster radius equation defines the distance at which intermolecular energy transfer is 50% effective.[1]

$$R_0{}^6 = \frac{9000(ln10)\kappa^2\phi_d}{128\pi^5 N n^4}\int_0^\infty \epsilon_a(\lambda)F_d(\lambda)\lambda^4 d\lambda \tag{3.1}$$

Where κ^2 is the orientation parameter, typically taken to be $^2/_3$ for random orientation; N_A is Avogadro's number; ϕ_d is the quantum yield of the donor; F_d is the normalized fluorescence profile of the donor and ϵ_a is the molar extinction profile of the acceptor molecule. The integral in equation 3.1 only attains any significant value when there is a non-negligible degree of overlap between the emission spectrum of the donor and the absorption spectrum of the acceptor, therefore defining the efficiency of the energy transfer process itself. Note that in this and all further FRET discussion in this section, the subscripts **d** and **a** correspond to donor and accepter molecules, respectively. The rate of transfer between a donor-accepter pair (k_{da}) is dependant upon their separation and is defined by:

$$k_{da} = \frac{1}{\tau_d}\left(\frac{R_0}{r}\right)^6 \tag{3.2}$$

where τ_d is the radiative lifetime of the donor excitation. It must be considered that the original theory and simple formulation of the Förster radius given in equation 3.1 simply predict the excitation transfer for a single donor and transfer molecule in an ideal system. In the case of our system there is a interspersed distribution of two dye molecules that is assumed to tend toward homogeneous when scaled up. Due to the sixth power dependency of R_0 however, the FRET interaction of molecules quickly tends towards negligible. Estimates of FRET rates from *average* molecular separation must therefore be understood as rough as $\frac{1}{<R^6>} \neq \frac{1}{<R>^6}$.

As such, although an estimate can be made of dye coverage of each molecule using absorption profiling and an estimated folding ratio for the mesostructure, the average separation derived can only lead to a crude estimate of the FRET rate.

From the time-integrated photoluminescence spectra, the steady state absorption spectra, an estimated fluorescence quantum yield of 2%.[?] A FRET rate of ~7 x 10^{10} s^{-1} is calculated,

[1] Note that several different reproductions of the Förster equation are observed to contain some degree of inaccuracy. Lakowicz' "Principles of Fluorescence Spectroscopy" denotes the π term of equation 3.1 as having a fourth power contribution [24] and, indeed, two of Förster's own papers cite a sixth power dependence for the π term [25, 26] leading to some confusion on the topic.

which, taken as a rough estimate, is consistent with the measured value of ~5 x 10^{10} s^{-1}. Both the modeled and measured FRET rate estimates suggest a FRET efficiency of around 50%.

The energy transfer dynamic has been explored more comprehensively by Hoke et al.[27] for the system in which the donor molecule is suspended in the hole transport medium and acts as a somewhat abstracted relay molecule, as discussed by Hardin et al.[?]

3.5 Conclusions

In summary, cosensitization has been utilized as a tool to significantly enhance the optical bandwidth and efficiency in solid-state DSCs with respect to the lone visible absorbing system. Efficient energy transfer is observed to occur from the visible absorbing dye to the near IR sensitizer, with subsequent conventional charge generation from both of the dyes described. This novel charge generation route proves to be remarkably useful, since it gives a second chance for charge generation to species which would have otherwise decayed prior to electron transfer.

Traditional single dye sensitization is restricted by the overall goal of realising a single molecule in which the processes of light absorption and charge injection are both optimised. This is not a trivial challenge of chemical engineering as, by linking these energy conversion aspects into a single molecule, there is no way of avoiding that the energetically active components will interact and so each affect the performance of the other. This is not necessarily a detrimental situation, but likely limits the efficacy of the performance in both fields to some degree. If, instead, discrete dye molecules could be used that each specialise in the area of light harvesting and carrier injection, it is possible that a significant overall performance enhancement could be achieved.

This energy transfer mechanism broadens possibilities to enhance the performance of existing visible sensitizers, potentially relaxes issues with aggregation of visible sensitizers, but more excitingly opens the design criteria for visible sensitizers: With this energy relay mechanism it should be possible to create surface tethered dyes optimized for light absorption strength and band width, neglecting the previous requirement to maximize their electron transfer efficiency.

Publication:

The concept, execution and results outlined in this chapter have been published in part in the Journal of Physical Chemistry C in 2011[28] as well as presented at conference; this is detailed further on page 118.

References

[1] H. J. Snaith and L. Schmidt-Mende, "Advances in liquid-electrolyte and solid-state dye-sensitized solar cells," *Advanced Materials*, vol. 19, pp. 3187–3200, 2007.

[2] J. Nelson, *The Physics of Solar Cells (Properties of Semiconductor Materials)*. Imperial College Press, 2003.

[3] A. D. Vos, "Detailed balance limit of the efficiency of tandem solar cells," *Physics*, vol. 839, 1979.

[4] H. J. Snaith, R. Humphry-Baker, P. Chen, I. Cesar, S. M. Zakeeruddin, and M. Gratzel, "Charge collection and pore filling in solid-state dye-sensitized solar cells," *Nanotechnology*, vol. 19, p. 424003, 2008.

[5] B. Mahrov, G. Boschloo, a. Hagfeldt, L. Dloczik, and T. Dittrich, "Photovoltage study of charge injection from dye molecules into transparent hole and electron conductors," *Applied Physics Letters*, vol. 84, no. 26, p. 5455, 2004.

[6] I. Bruder, M. Karlsson, F. Eickemeyer, J. Hwang, P. Erk, A. Hagfeldt, J. Weis, and N. Pschirer, "Efficient organic tandem cell combining a solid state dye-sensitized and a vacuum deposited bulk heterojunction solar cell," *Solar Energy Materials and Solar Cells*, vol. 93, pp. 1896–1899, Oct. 2009.

[7] S. Wenger, *Strategies to Optimizing Dye-Sensitized Solar Cells : Organic Sensitizers , Tandem Device Structures , and Numerical Device Modeling*. PhD thesis, EPFL, 2010.

[8] Y. Tachibana, K. Nazeeruddin, M. Gr, D. R. Klug, and J. R. Durrant, "Electron injection kinetics for the nanocrystalline TiO2 films sensitised with the dye (Bu4N)2Ru(dcbpyH)2(NCS)2," *Chemical Physics*, vol. 285, pp. 127–132, 2002.

[9] M. K. Nazeeruddin, A. Kay, E. Miiller, P. Liska, N. Vlachopoulos, M. Gratzel, C. Lausanne, and R. April, "Conversion of light to electricity by cis-X2bis(2,2'-bipyridyl-4,4'-dicarboxylate)ruthenium(II) charge-transfer sensitizers (X = Cl-, Br-, I-, CN-, and SCN-) on nanocrystalline titanium dioxide electrodes," *Journal of the American Chemical Society*, no. 4, pp. 6382–6390, 1993.

[10] L. Schmidt-Mende, U. Bach, R. Humphry-Baker, T. Horiuchi, H. Miura, S. Ito, S. Uchida, M. Grï¿œtzel, and M. Gratzel, "Organic Dye for Highly Efficient Solid-State Dye-Sensitized Solar Cells," *Advanced Materials*, vol. 17, pp. 813–815, Apr. 2005.

[11] R. Jose, a. Kumar, V. Thavasi, and S. Ramakrishna, "Conversion efficiency versus sensitizer for electrospun TiO(2) nanorod electrodes in dye-sensitized solar cells.," *Nanotechnology*, vol. 19, p. 424004, Oct. 2008.

[12] P. Y. Reddy, L. Giribabu, C. Lyness, H. J. Snaith, C. Vijaykumar, M. Chandrasekharam, M. Lakshmikantam, J. H. Yum, K. Kalyanasundaram, M. Graetzel, and M. K. Nazeeruddin, "Efficient Sensitization of nanocrystalline TiO2 films by a near-IR-absorbing unsymmetrical zinc phthalocyanine," *Angewandte Chemie*, vol. 46, pp. 373–376, 2007.

[13] T. Geiger, S. Kuster, J.-H. Yum, S.-J. Moon, M. K. Nazeeruddin, M. Grdtzel, and F. Esch, "Molecular Design of Unsymmetrical Squaraine Dyes for High Efficiency Conversion of Low Energy Photons into Electrons Using TiO2 Nanocrystalline Films," *Advanced Functional Materials*, vol. 19, pp. 2720–2727, 2009.

[14] T. Horiuchi, H. Miura, K. Sumioka, and S. Uchida, "High efficiency of dye-sensitized solar cells based on metal-free indoline dyes," *Journal of the American Chemical Society*, pp. 12218–12219, 2004.

[15] J. J. Cid, M. Garcia-Iglesias, J. H. Yum, A. Forneli, J. Albero, E. Martinez-Ferrero, P. Vazquez, M. Gratzel, M. K. Nazeeruddin, E. Palomares, and T. Torres, "Structure-Function Relationships in Unsymmetrical Zinc Phthalocyanines for Dye-Sensitized Solar Cells," *Chemistry-a European Journal*, vol. 15, pp. 5130–5137, 2009.

[16] J. H. Yum, S. R. Jang, R. Humphry-Baker, M. Gratzel, J. J. Cid, T. Torres, and M. K. Nazeeruddin, "Effect of coadsorbent on the photovoltaic performance of zinc pthalocyamine-sensitized solar cells," *Langmuir*, vol. 24, pp. 5636–5640, 2008.

[17] B. E. Hardin, A. Sellinger, T. Moehl, R. Humphry-Baker, J.-E. Moser, P. Wang, S. M. Zakeeruddin, M. Gratzel, and M. D. McGehee, "Energy and Hole Transfer between Dyes Attached to Titania in Cosensitized Dye-Sensitized Solar Cells," *Journal of the American Chemical Society*, vol. 133, pp. 10662–10667, July 2011.

[18] Driscoll, F. Jf, Humphry-Baker, Torres, H. Wts, S. Hj, and F. Rh, "Enhanced Photoresponse in Solid-State Excitonic Solar Cells via Resonant Energy Transfer and Cascaded Charge Transfer from a Secondary Absorber," *Nano Letters*, vol. 10, pp. 4981–4988, 2010.

[19] K. Kalyanasundaram, *Dye-sensitized Solar Cells*. CRC Press, 1 ed., 2010.

[20] R. Zhu, C.-Y. Jiang, B. Liu, and S. Ramakrishna, "Highly Efficient Nanoporous TiO 2 -Polythiophene Hybrid Solar Cells Based on Interfacial Modification Using a Metal-Free Organic Dye," *Advanced Materials*, vol. 21, pp. 994–1000, Mar. 2009.

[21] T. Leijtens, I.-k. Ding, T. Giovenzana, J. T. Bloking, M. D. Mcgehee, and A. Sellinger, "Hole Transport Materials with Low Glass Transition Temperatures and High Solubility for Application in Solid-State Dye-Sensitized Solar Cells," *ACS Nano*, vol. 6, no. 2, pp. 1455–1462, 2012.

[22] H. J. Snaith and C. Ducati, "SnO2-Based Dye-Sensitized Hybrid Solar Cells Exhibiting Near Unity Absorbed Photon-to-Electron Conversion Efficiency," *Nano Letters*, vol. 10, pp. 1259–1265, 2010.

[23] B. Wenger, M. Gratzel, J. E. Moser, Wenger, Gratzel, and M. Je, "Rationale for kinetic heterogeneity of ultrafast light-induced electron transfer from Ru(II) complex sensitizers to nanocrystalline TiO2," *Journal of the American Chemical Society*, vol. 127, pp. 12150–12151, Sept. 2005.

[24] J. R. Lakowicz, *Principles of Fluorescence Spectroscopy*. Springer, 2nd ed., June 1999.

[25] T. Forster, *Fluoreszenz Organischer Verbindungen*. Vandenhoeck and Ruprecht, Gotingen, 1951.

[26] T. Forster, "Transfer Mechanisms Of Electronic Excitation," *Disc. Faraday. Soc*, no. 10, pp. 7–17, 1959.

[27] E. T. Hoke, B. E. Hardin, and M. D. McGehee, "Modeling the efficiency of Förster resonant energy transfer from energy relay dyes in dye-sensitized solar cells.," *Optics express*, vol. 18, pp. 3893–904, Feb. 2010.

[28] M. D. Brown, P. Parkinson, T. Torres, H. Miura, L. M. Herz, and H. J. Snaith, "Surface Energy Relay Between Cosensitized Molecules in Solid-State," *The Journal of Physical Chemistry C*, vol. 115, no. 46, pp. 23204–23208, 2011.

Chapter 4

Plasmonic Nanostructures Incorporated into DSCs to Enhance Photocurrent Generation

---

Presenting an investigation into incorporating core-shell Au-SiO_2 nanoparticles into dye-sensitized solar cells. Plasmon enhanced light absorption is consistently observed, leading to overall increases in photocurrent and efficiency for both iodide/triiodide electrolyte based and solid-state dye-sensitized solar cells. Spectroscopic investigation indicates that plasmon enhanced photocarrier generation competes well with plasmons oscillation damping within the first tens of fs following light absorption.

4.1 Plasmonics Introduction

For many hundreds of years the optical properties of various metal nanoparticles had been unwittingly used and appreciated in many areas of culture, the most readily observable of which is stained glass windows. For many centuries the production of coloured glasses was developed and used while little physical comprehension of the optical properties being exploited. The understanding of the vivid colours acheived was largely empirical until Raleigh began to define the scattering for small [1] and large particles.[2, 3] The scattering from spherical nanoparticles was formally and exactly described by Mie in 1908.[?]

In the early 1950s, during investigation of high velocity electron scattering by thin metal foils, there was some confusion over characteristic energy losses that arose unexplained by then-current theory.[4, 5] Following Ritchie's 1957 description of how plasma oscillations (plasmons) could be responsible for this energy loss,[6] there followed corroborating experimental observations reported by Powell and Swan in 1960.[7] Later, Vicent and Silcox[8] and Pettit et al.[9] analyzed the full dispersion relation of surface plasmon polaritons. Since this point, significant research began into the possible applications of plasmonics in several fields including biosensing,[10] all-optical integrated circuits [?, 11] and, recently, solar cells.[12–15]

4.1.1 Physical Explanation of Surface Plasmon Polaritons

Surface plasmons are a quasiparticle interpretation for the occurance of guided waves at the inferface between a metal and dielectric. The free electonic nature of metals allows collective response to electromagnetic fields. This can be illustrated most simply with a flat interface, as figure 4.1, which illustrates the electromagnetic field amplitude associated with a surface plasmon traveling along this interface. It can be observed that the field of the plasmon decays exponentially from the boundary into the dielectric and into the metal and, further, that the decay length is significantly lower in the metal due to the free charges screening the field.[16]

Although a flat interface topography is the simplest in terms of illustration, surface plasmons cannot be *directly* generated at a flat metal-dielectric interfact by incident sunlight. This is because the surface plasmon has a wavevector greater than that of the photon in the adjacent dielectric, precluding coupling of the incident light to the surface plasmon.[?] The field generation around a spherical nanoparticle is significantly more complex, as figure 4.2 illustrates, yet

Figure 4.1: Amplitude of surface plasmon field at a metal-dielectric interface for illustrative purposes.

provides a possible architecture with which to integrate plasmonic effects into solar cells.

4.1.2 Mathematical treatment

The nature of plasmon appearance can be described formally from Maxwell's equations:

$$\Delta \cdot \mathbf{D} = \rho_{ext} \tag{4.1}$$

$$\Delta \cdot \mathbf{B} = 0 \tag{4.2}$$

$$\Delta \times \mathbf{E} = -\frac{\delta \mathbf{B}}{\delta t} \tag{4.3}$$

$$\Delta \times \mathbf{H} = \mathbf{J_{ext}} + \frac{\delta \mathbf{D}}{\delta t} \tag{4.4}$$

linking the four macroscopic electromagnetic fields: **D**, the dielectric displacement; **E**, the electric field; **H**, the magnetic field and **B**, the magnetic induction. In the absence of external charge or current densities, equations 4.3 and 4.4 can be combined to form the wave equation:

$$\Delta \times \Delta \mathbf{E} = -\mu_0 \frac{\delta^2 \mathbf{B}}{\delta t^2} \tag{4.5}$$

when treated to have negligible variation of the dielectric profile ε below sub-wavelength distances and assuming a harmonic time dependance $\mathbf{E}(\mathbf{r},t) = \mathbf{E}(\mathbf{r})e^{-i\omega t}$ in general, this can be revised as the Helmholtz equation:

$$\Delta^2\mathbf{E} + k_0^2\varepsilon\mathbf{E} = 0 \tag{4.6}$$

where k_0 is the wave vector $(\frac{\omega}{c})$. By solving independantly for regions of constant dielectric profile and implementing appropriate boundary conditions the Helmholtz equationcan be used to formulate models for plasmon modes, such as that illustrated in figure 4.2.[17] The formulation of the Helmoltz equation and the nature of plasmonics is more comprehensively outlined by Maier.[18]

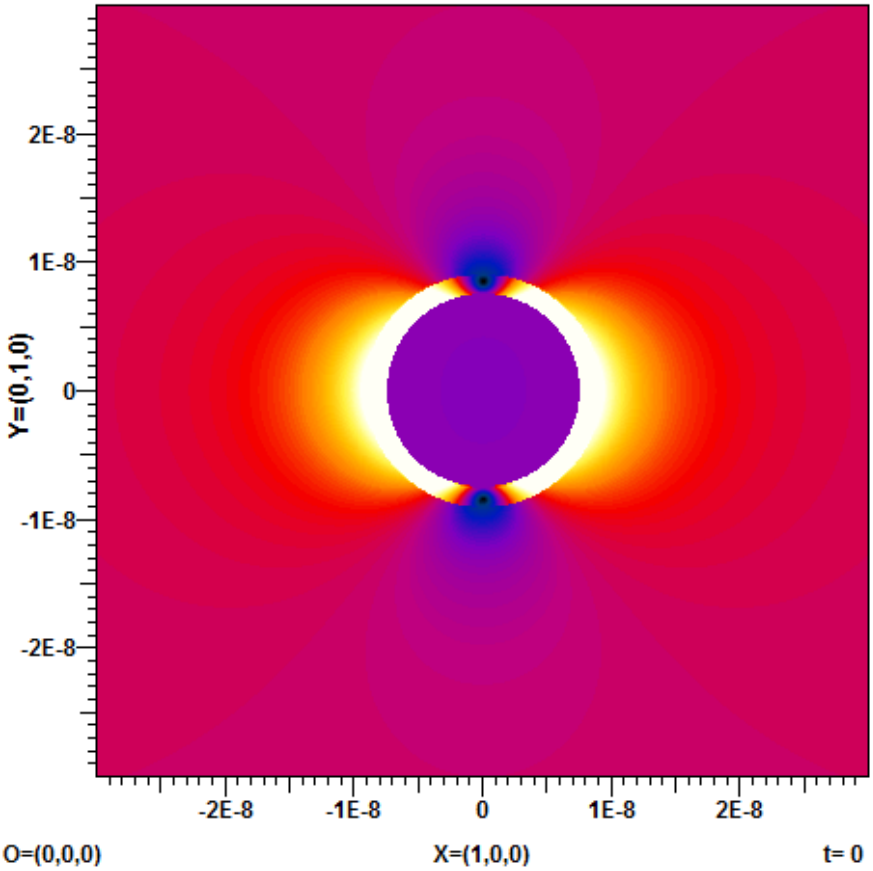

Figure 4.2: Amplitude of surface plasmon field at and in proximity to a silica-coated gold nanoparticle. *Model and graphic courtesy of Michael Saliba, Oxford 2011*

4.2 Plasmonic Solar Cell History and Contemporary Literature

The broad applications for controlling light at sub-wavelength dimensions in optoelectronic and photonic devices have created a vibrant field of nanophotonics and plasmonics.[?, 10–19] Surface plasmon resonance from metallic nanostructures can deliver significant control over the optical field and the prospective utilization of metallic nanostructures to enhance the light absorption in thin film and organic based solar cells is a pursuit which is attracting mounting interest.

For some time researchers have been working towards "plasmonic solar cells" but the recent advances in control of metal nanoparticle synthesis and self assembled metallic nanostructures is resulting in a rapid growth of this new field. Although there has been much discussion of 'plasmonic solar cells', the moniker is perhaps misleading, as surface plasmonic effects can be used to absorb sunlight but, with no native route to generating separated carriers, cannot form a functioning solar cell without being integrated into another system. 'Hybrid plasmonic solar cell' is a more accurate term but for the sake of brevity 'plasmonic solar cell' is often used to indicate any device, theoretical or realised, that incorporates plasmonic effects with the intention of enhancing light absorption with the eventual goal of improving photocurrent generation.

Perhaps the first plasmonic solar cell was reported by Hayashi et al in 1991;[19] however, although some evidence of photocurrent enhancement was illustrated, this was an improvement in the regime of nA that was only documented for a single laser-illuminated wavelength and so does not realistically constitute an effective exhibition of the performance enhancements possible. Enhancement in light absorption and photocurrent generation in thin film inorganic solar cells has already been demonstrated,[20–23] and in this field plasmonics has the potential to significantly reduce the quantity of material required and hence the fabrication costs of thin film photovoltaics. In wafer-based silicon devices anisotropic etching can be undertaken to form pyramid like structures, enhancing scattering and recycling of incoming light, improving light uptake by integrated means.

With relevance to dye-sensitized solar cells: enhanced light absorption in conventional dyes employed in these devices has been demonstrated on flat TiO_2 films when silver islands are thermally evaporated upon the TiO_2 prior to dye adsorption.[24] More recently, enhancement of charge carrier generation and photocurrent generation in dye-sensitized solar cells (DSC)

has also been reported for dye monolayers on flat TiO_2 films incorporating silver islands or sparse coatings of metal nanoparticles.[25, 26] Concerning organic photovoltaics, an unexpected enhancement in light absorption and charge generation in tandem solar cells was observed by Rand et al. utilizing silver nanoparticle clusters as the recombination boundary between the active layers of the tandem device.[27] They identified that surface plasmon modes on the silver clusters were responsible for enhanced photocurrent in the solar cells. More recently, Kulkarni et al. have demonstrated enhanced charge carrier generation in optically thin polymer blend photovoltaic films adjacent to silver nanoprisms via photo-induced absorption spectroscopy.[28]

4.3 Realisation of Plasmonic Dye Sensitized Solar Cells

4.3.1 Concept

Though there have been a number of demonstrations of plasmon enhanced charge generation as noted in the previous section (4.2) to the author's best knowledge these have all been fabricated on unconventional device structures, which will not be easily incorporated to enhance the current state-of-the-art technologies. The architecture developed within this chapter provides a route that appears compatible with current DSC production methods.

4.3.2 Evaporative metal island Incorporation

In the beginining stages of this work a prototype method for plasmonic hybridisation was developed wherein extremely thin films of gold would be thermally evaporated into the device structure following the dye steps and preceding the HTM infiltration. The motivation being that the low volume of gold evaporated would consolidate into discrete metal islands whose dimensions may induce plasmonic effects. The concept is entirely unguided and simply depends upon the cohesivity of the liquid-phase metal to affliate and form a sphere or spheroid topography. Comparable evaporative metal-island films have been investigated by Westphalen et al,[29] although the absence of characterisation implicitly suggests that no absolute performance enhancements were achieved.

The first stage of this investigation involved the precise callibration of the evaporation system by comparison of 'estimated depth' of the evaporated metal with the 'measured depth'; where 'estimate depth' is derived from the variation of the frequency of the vibrating crystal in the roof

of the evaporation chamber; 'measured depth' is directly measured with a surface profilometer. In light of the ambiguity of these results and rudimentary nature of the system itself, it must be noted that this preliminary investigation into plasmonic structure incorporation is included only for completeness and transparency and is not meant to be considered in any way a complete investigation in its own right. The route is noted in the main for its early indication of the apparent futility of incorporating a significant volume of pure metal into the device architecture due to the electrical detriment imposed by the internal incorporation of carrier recombination sites afforded by the free carrier nature of metals themselves.

4.3.3 Nanoparticle based Plasmonic Incorporation

In the course of this work is was proposed to integrate Au metal nanoparticles, which exhibit intense absorption due to surface plasmon resonance in the visible region of the spectrum, into dye-sensitized solar cells employing both the iodide/triiodide redox couple and the solid-state hole-transporter 2,2',7,7'-tetrakis-(N,N-di-p-methoxyphenylamine)-9,9'-spirobifluorene (spiro-OMeTAD).[?] Incorporating "bare" metal nanoparticles into the bulk of dye-sensitized solar cells is shown to be detrimental due to both corrosion and the metal acting as a charge recombination centre. It is then demonstrated that by coating the Au nanoparticles with a thin shell of silica, they can be incorporated into the TiO_2 mesoporous paste and are capable of sustaining the sintering process of the TiO_2 with negligible influence to the optical properties. Furthermore, they are corrosion resistant in the iodide/triiodie electrolyte, and have no apparent detrimental electronic consequence in the solar cells, as far as charge recombination is concerned. Beyond this, through both an electronic and spectroscopic investigation enhanced photocurrent generation and solar cell performance is demonstrated as a result of light harvested by the metal nanoparticles.

4.3.4 Incorporation methods

Au nanoparticles with and without a thin sodium silicate shell were prepared according to previously published methods with slight modification.[30, 31] A fabrication description is provided in appendix A.3. For incorporating the Au or Au-SiO_2 nanoparticles into the solar cells the water dispersed nanoparticles were first precipitated by centrifugation and then redispersed in ethanol. Two methods of incorporating nanoparticles into DSSCs were employed with the intention of dispersing the nanoparticles in close proximity to the dye molecules whilst retaining homogene-

ity. The first method involved blending a Au nanoparticle solution directly into the titania paste and then using this altered "plasmonic paste" in an otherwise standard device fabrication protocol. The second approach involved the direct spin coating of Au-SiO_2 nanoparticles on to dye sensitized titania prior to application of the hole transport material (HTM). These routes are simply illustrated in figure 4.3

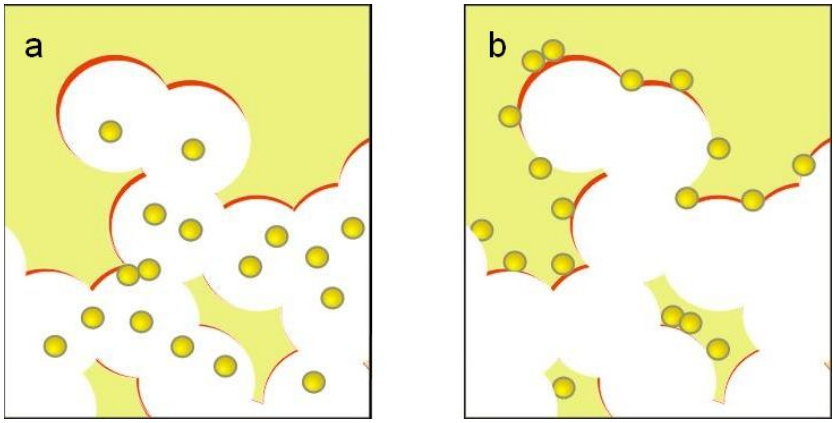

Figure 4.3: Simple schematic of spin coat or doctor blade incorporation routes. Panel **a** (left) illustrates the gold nanoparticles incorporated directly into the titania paste pre-sinter and then continuing the fabrication process as normal, panel **b** (right) illustrates the incorporation of nanoparticles by the spin casting of a highly concentrated nanoparticle solution directly onto the dyed mesostrucure.

4.3.4.1 Nanoparticle Fabrication and Encapsulation

The fabrication of nanoparticles is not the focus of this thesis and, indeed, the majority of the nanoparticles utilised during the investigations outlined were fabricated at request by collaborators in the Wiesner group at Cornell University. In order to electronically and chemically insulate the metal, synthesised Au core-silica shell (Au-SiO_2), nanoparticles were used. A fabrication outline is given in appendix A.3. In figure 4.4 transmission electron microscopy (TEM) images of 'bare' Au (a) and Au-SiO_2 core-shell nanoparticles (b) are shown.

The presence of the silica shell encapsulating the gold core nanoparticles allows un-attenuated propagation of the optical field around the nanoparticles. The core-shell architecture is considered to provide a number of potential effects that may be beneficial for the final performance of

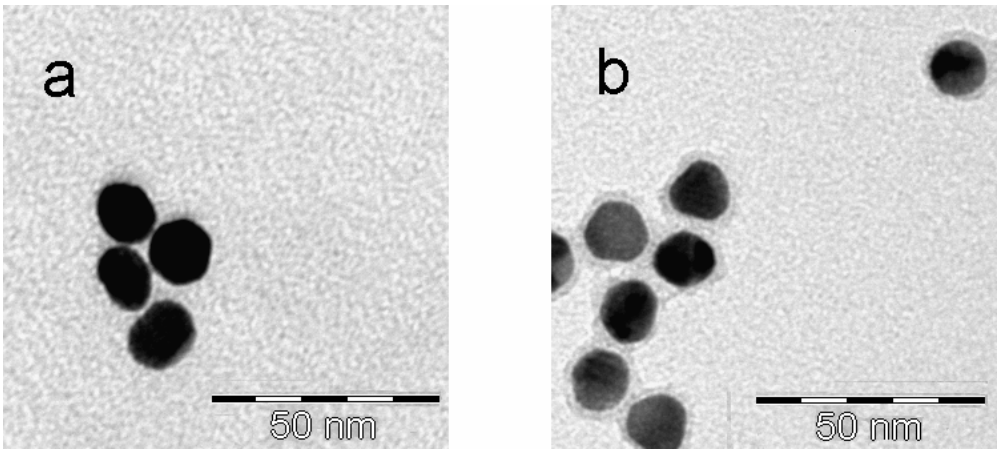

Figure 4.4: TEM images showing: a) ~15nm diameter bare gold nanoparticles, and b) Au-SiO_2 core-shell nanoparticles with ~15nm Au cores encapsulated by ~3nm silica shells. *TEM images were obtained with a FEI Tecnai T12 Spirit microscope operated at an acceleration voltage of 120kV. Images courtesy of T. Suteewong, Cornell 2009*

the fabricated hybrid DSC:

1. As a wide bad-gap insulator, and with a sufficient thickness, the SiO_2 shell electronically insulates the metal core from the surrounding device morphology and thus prevents them acting as internal recombination centres for photogenerated charge carriers.

2. The presence of the core-encasing shell also ensures the physical separation of the metal from the HTM, inhibiting corrosion in oxidising or corrosive media. Any optical enhancements in the dye chromophores are likely to be sensitively dependent upon the physical separation between them and the metal nanoparticle surface.[32]

3. The spatial separation of the nanoparticle core from the dye molecules themselves may provide some degree of control over the interaction between the photoaction of both. If the chromophore is too close, it is foreseeable that energy transfer from the excited dye to the plasmon mode of the nanoparticle may dominate; whilst,as separation increases, the generation of near-field absorption enhancements in the dye becomes unlikely. The silica shell encapsulating the metal core proveds some degree of control over this distance.

4. As will be demonstrated in section 4.3.4.2, the silica shells provide a significant degree of thermal and structural stability, most significantly in the prevention of Ostwald ripening (whereby over time or with input heat, small crystals and particles can change shape, distort or amal-

gamate to form larger particles[33]), allowing use of orthodox thermal processing routes during device fabrication.

4.3.4.2 Nanoparticle Response to Sintering

As a route to uniformly mix the nanoparticles throughout the bulk of the photo-active layer they were redispersed in a common solvent to the TiO_2 paste (ethanol) and subsequently blended with the TiO_2 paste. In order to determine if the Au nanoparticles can be mixed with the conventional mesoporous TiO_2 and sustain the standard device processing protocol, the absorption profile at various stages in the thin film fabrication has been examined. In figure 4.5 this is shown for both bare Au and Au-SiO_2 core-shell nanoparticles. The solution absorption maximum of the colloidal nanoparticles was at ~524 nm in water (where $n_{water} = 1.33$) and ~551 nm when redispersed in ethanol (where $n_{ethanol} = 1.36$). The shift in the absorption peak of the plasmon mode is due to the increased dielectric constant of the solvent.[34] The peak absorption of the plasmon mode on the bare Au nanoparticles incorporated into the TiO_2 paste is similar to that in the ethanol, but there is a long tail to the absorption, suggesting a significant degree of nanoparticle aggregation. Upon sintering the paste containing the bare Au nanoparticles, the peak absorption maximum undergoes a significant red shift to ~ 600nm, and the intensity has also significantly increased. For Au nanoparticles to exhibit a surface plasmon mode with an absorption peak at 600nm, the diameter must be greater than 100 nm if spherical,[34] whilst, if elongated, the aspect ration must be on the order of 2:1,[35] suggesting that the original 15nm particles have Ostwald ripened into larger objects during the heat treatment. When dyed, the films containing the bare nanoparticles show two distinctive peaks, one for the sensitizer and one for the Au nanoparticles. In contrast, there is little shift to the peak absorption position of the films incorporating the core-shell nanoparticles, illustrating that the SiO_2 shell stabalises the Au nanoparticles to thermal processing. Due to the similarity of the absorption maxima for the dye (525 nm) and Au-SiO_2 nanoparticles (525 to 540 nm), the dyed films exhibit a single peak around 525nm.

4.3.5 Characterisation of Nanoparticle-Incorporating DSCs

In principle metal nanoparticles could enhance the absorption in the solar cell by either scattering light enabling a longer optical path-length, by a dipole-dipole interaction and resonant

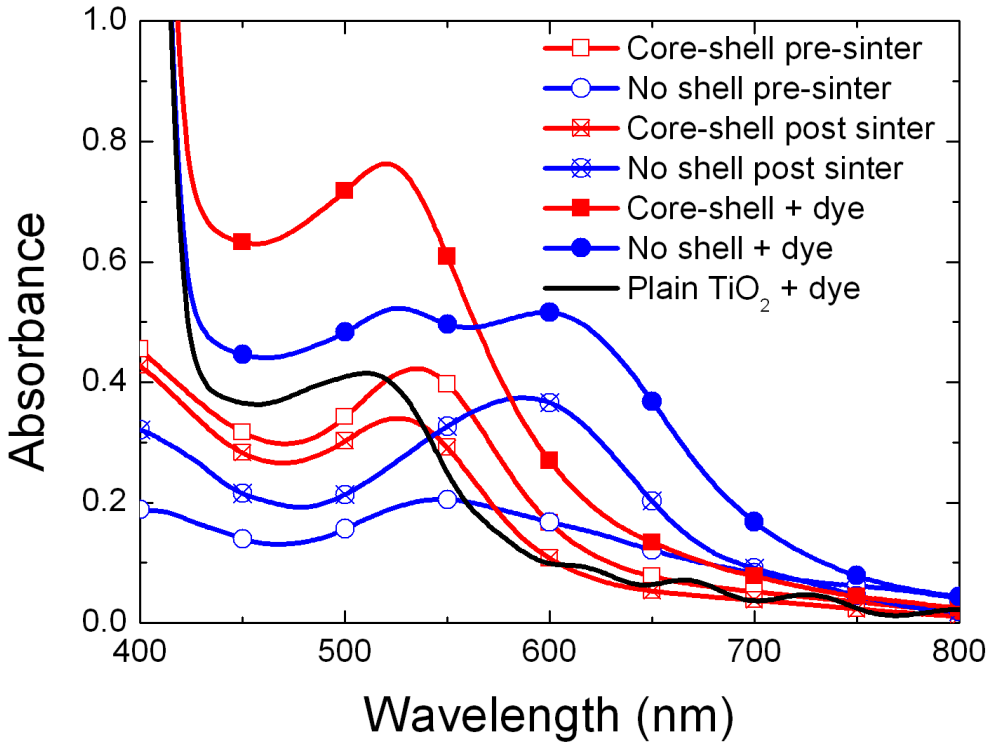

Figure 4.5: Absorption spectra of thin films (~1 mm) processed with conventional mesoporous TiO_2 paste at different stages in the fabrication process; directly after doctor blade coating (open-symbols, "pre-sinter"), after two thermal sintering cycles at 500 $^\circ$ C and a chemical $TiCl_4$ treatment (open-symbols with cross-through, "post-sinter"), and with final dye-sensitization with Z907 ruthenium complex (solid-symbols). These are for TiO_2 paste incorporating bare Au nanoparticles (blue circles) and Au-SiO_2 core shell nanoparticles (red squares). Also shown is the absorption spectra of a standard mesoporous TiO_2 film sensitized with Z907 (solid-line)

energy transfer or by near-field coupling between the surface plasmon polariton and the dye excited state. In order to measure the fraction of scattering versus absorption from the mesoporous TiO_2 electrodes containing the Au-SiO_2 nanoparticles UV-vis transmission and reflection measurements in an integrating sphere have been performed. The spectra are shown in figure 4.6. All light, which is either scattered from or transmitted directly through the film, is detected in the total transmission. Hence the deviation from 100% transmission indicates light absorbed in the film or reflected. In this instance the total transmission (T_{tot}) is 36% at the peak absorbing wavelength of the nanoparticles (525nm) and the total reflection (R_{tot}) is 8% indicating total absorption (A_{tot}) in the film, $A_{tot}(\%)$ = 100-R_{tot}-T_{tot}, of 56%. The off specular, or scattered transmission through the film, is measured by taking the transmission spectra with a diffuse reflector absent from the exit port on the integrating sphere. For the film measured here, the off specular transmission at 525nm is only 0.47%, while the off specular reflected light is 2.2%. The sum of the off specular transmitted and reflected light (forward and backwards scattering) amounts to less than 3% of the incident light as compared to 56% which is absorbed in the metal nanoparticles. This indicates that enhancements in light absorption or photocurrent generation in the solar cells incorporating these metal nanoparticles is likely to be due to resonant energy transfer or near field coupling and not scattering.

In order to incorporate metal nanoparticles as light harvesting components in dye-sensitized solar cells, there were initial attempts to employ 'bare' gold or silver nanoparticles as a means to generate enhanced light absorption and photocurrent generation. To incorporate the nanoparticles into the devices, the metal nanoparticle colloids were dispersed in ethanol and mixed them directly with the mesoporous TiO_2 pastes, with subsequent thin film processing and sintering as is usually conducted with conventional devices.

Although the light absorption was monotonically increased with incorporating increasing amounts of metal nanoparticles into the mesoporous TiO_2, at the same time the photocurrent, photovoltage and fill factor of the ensuing devices were significantly and linearly decreased for both solid-state and liquid electrolyte based DSCs. This is illustrated by figure 4.7 and is also noted to be typical of the response observed by evaporative incorporation of metal islands as outlined in section 4.3.2. This is likely due to the nanoparticles acting as recombination centres within the device itself, in essence creating internal short-circuits throughout the bulk of the photoactive layer. From initial studies it was concluded that in order to integrate the metal

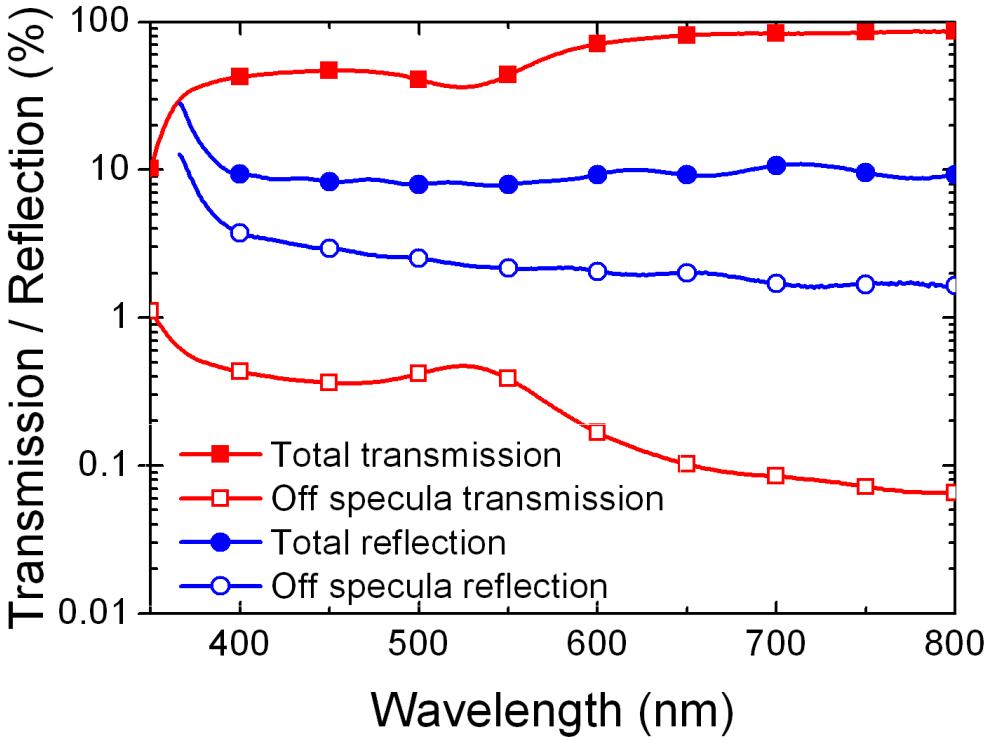

Figure 4.6: Transmission and reflection spectra for mesoporous TiO_2 films incorporating core-shell nanoparticles of similar concentration to those shown in 4.5

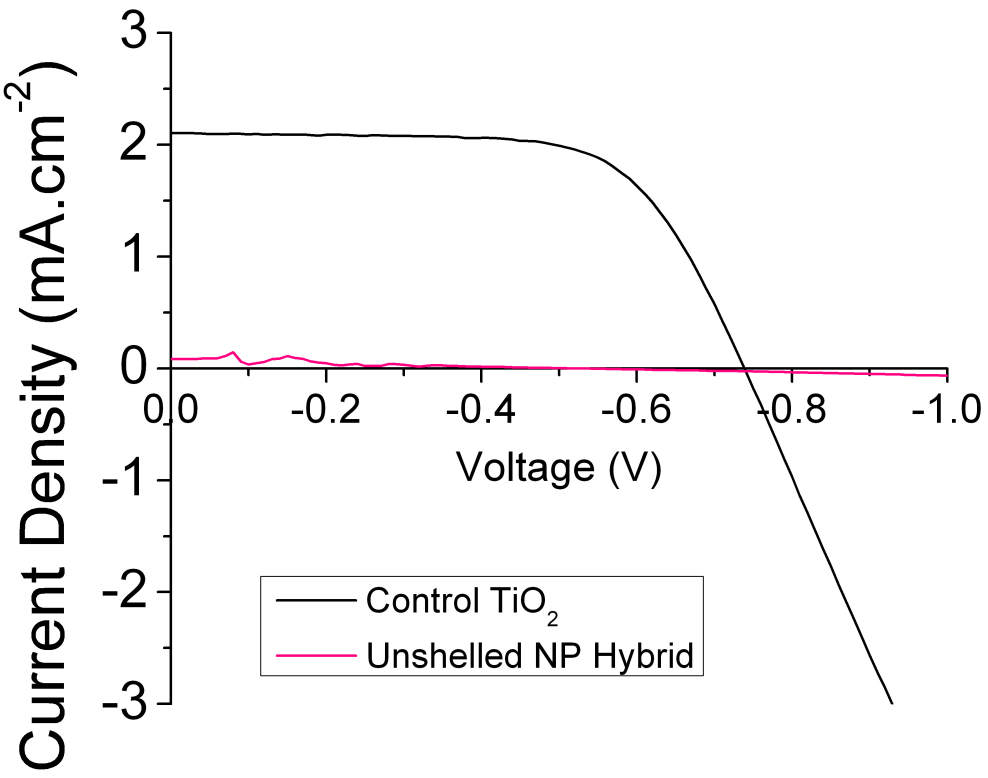

Figure 4.7: Current-voltage characteristics for eDSCs with and without bare nanoparticle incorporation. It is readily observed that the all the electronic characteristics are severely impaired with the simple inclusion of bare nanoparticles, likely by the provision of internal recombination sites.

nanoparticles within the bulk of the active layer, it is necessary to electronically and chemically insulate them from the semiconducting or ionic components. Standridge et al.[36] have also come to a similar conclusion when incorporating metal nanoparticles into flat junction liquid electrolyte based DSSCs, however, their main concern with electrolyte based DSSCs was not the electronic consequence of the presence of the metal, but the metal being corroded by the electrolyte.

As described above and illustrated in figure 4.7, in all cases the inclusion of the bare Au nanoparticles into the dye-sensitized solar cells significantly deteriorated the performance. Predominantly reducing the device open-circuit voltage and fill factor for the solid-state DSSCs and totally inhibiting photocurrent in the electrolyte DSSCs employing the iodide/triiodide redox

couple. To scrutinize the influence of the Au-SiO_2 nanoparticles on solar cell performance the metal nanoparticles were incorporated into the devices via two routes discussed in section 4.3.4.

From ablative X-ray photoelectron spectroscopy (XPS) depth profiling, it was identified that the 'plasmonic paste' method produced films uniformly distributed gold nanoparticles throughout the depth (figure 4.8). However, for the spin-coating method, the nanoparticles were predominantly on the top surface of the films (figure 4.9). The cross sectional SEM image in figure 4.10 is also consistent with the suggestion that the plasmonic paste method results in uniform mixing of the components.

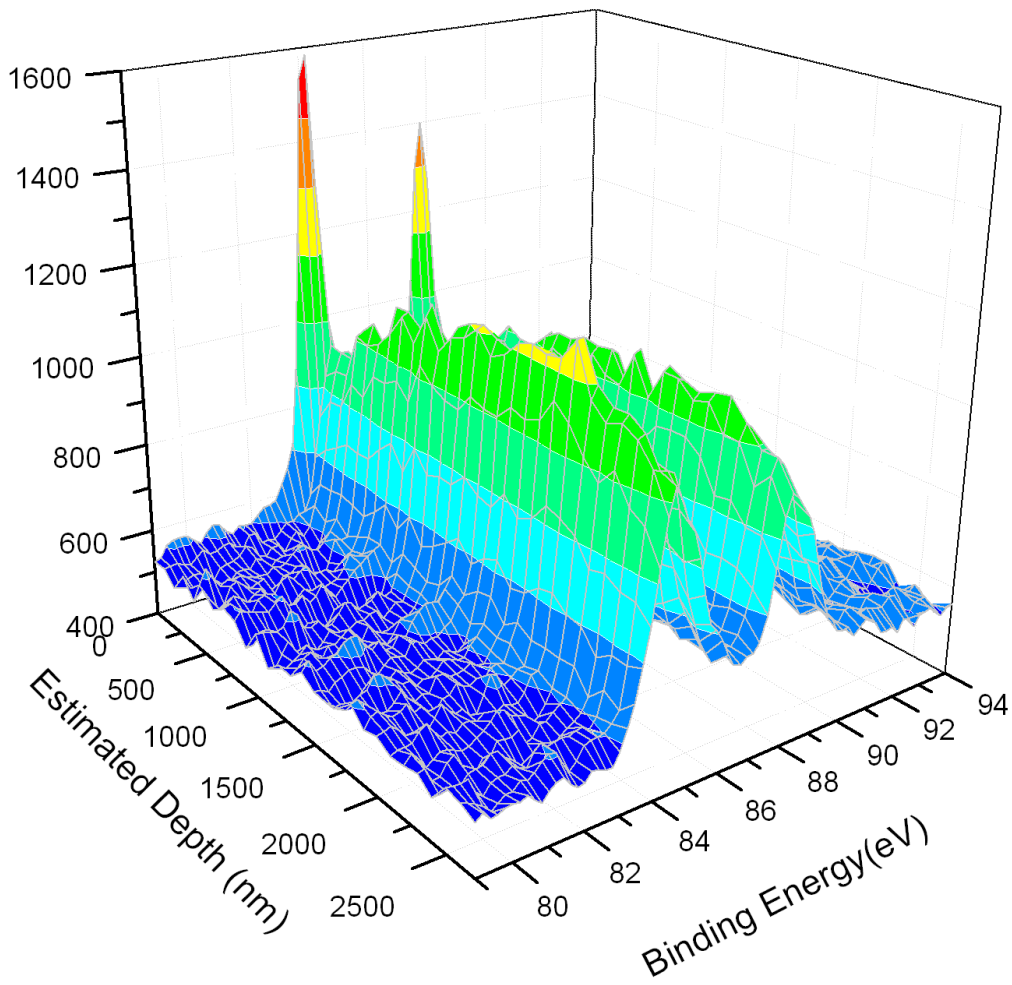

Figure 4.8: Doctor blade nanoparticle incorporation: ablative XPS depth profile. The core-level binding energies are noted in figure 4.9 and, in this case, are observed at a stable signal strength at all depths through the substrate implying a homogeneous distribution of gold nanoparticles throughout the mesostructure. *XPS data courtesy of I-K. Ding, Stanford 2010*

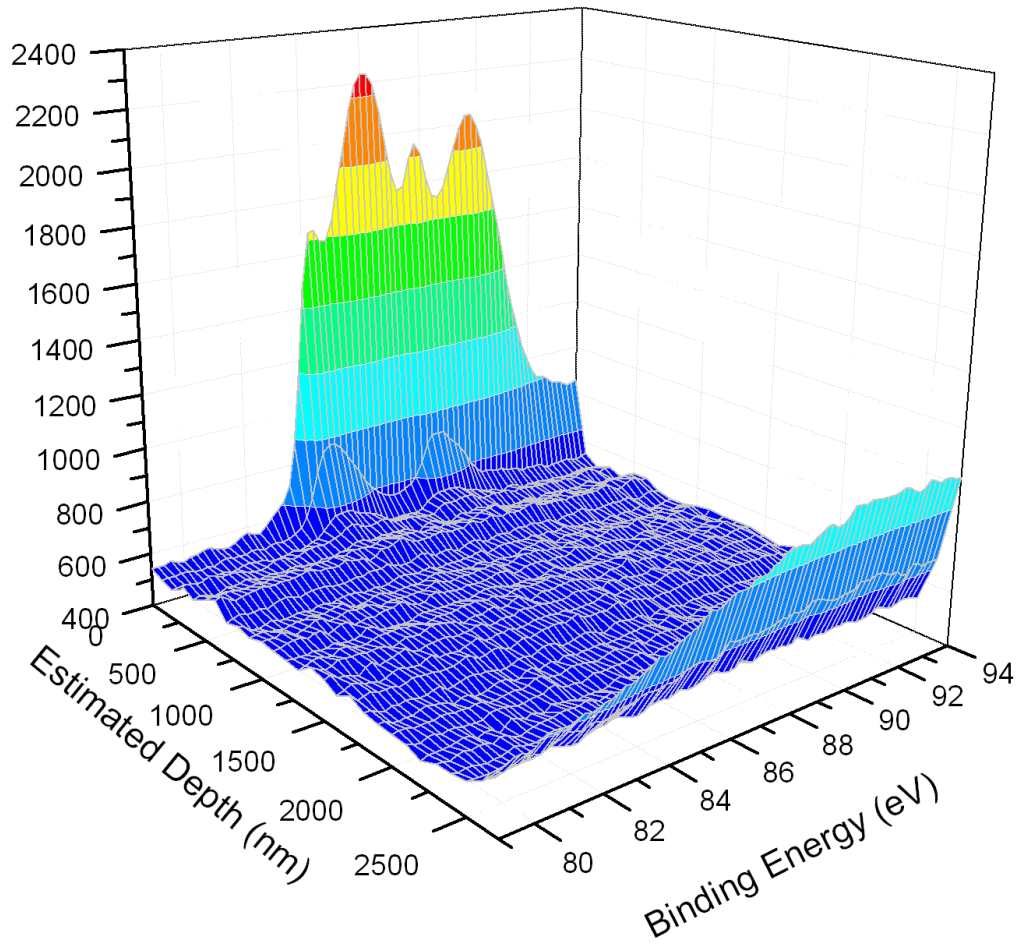

Figure 4.9: Spin coat nanoparticle incorporation: ablative XPS depth profile. The core-level binding energy of the $4f_{7/2}$ and the $4f_{7/2}$ are at 83.9eV and 87.6eV respectively.[37] The signal for these energies is observed to be strong at the immediate surface of the mesostructure but fade within the first 300nm, implying that the nanoparticles do not infiltrate the pores significantly. *XPS data courtesy of I-K. Ding, Stanford 2010*

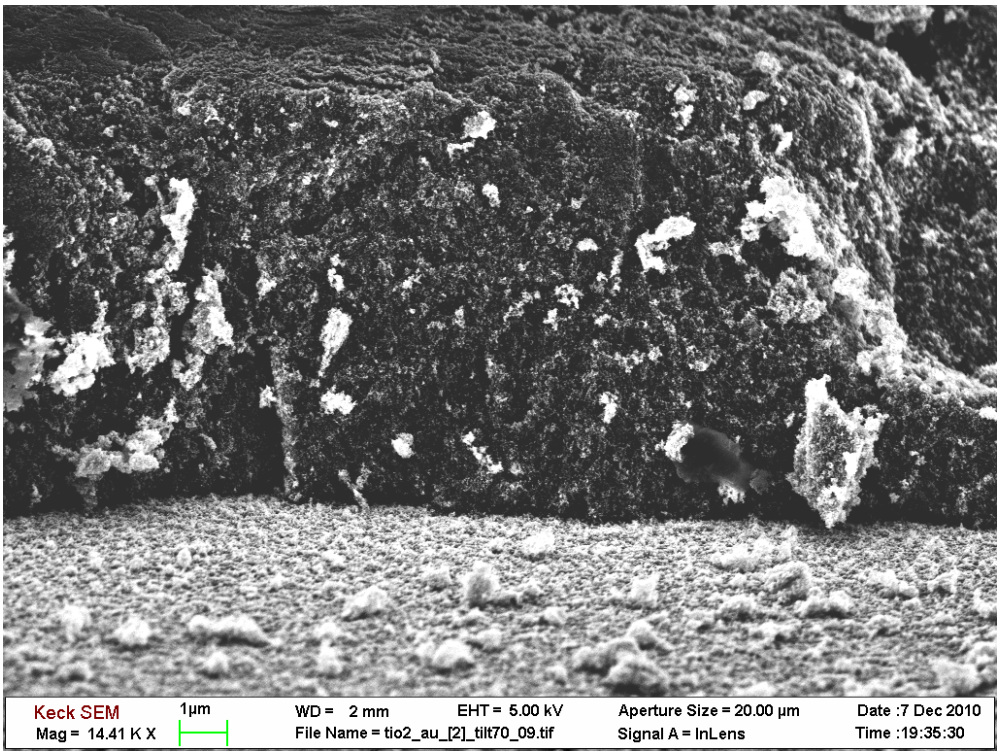

Figure 4.10: SEM of gold np integrated TiO_2 mesostructure. The lighter shapes in the mesostructure are understood to be Au-SiO_2 nanoparticles, corroborating the findings of figure 4.8 that imply a homogeneous distribution of gold throughout the substrate. *SEM courtesy of I-K. Ding, Stanford 2010*

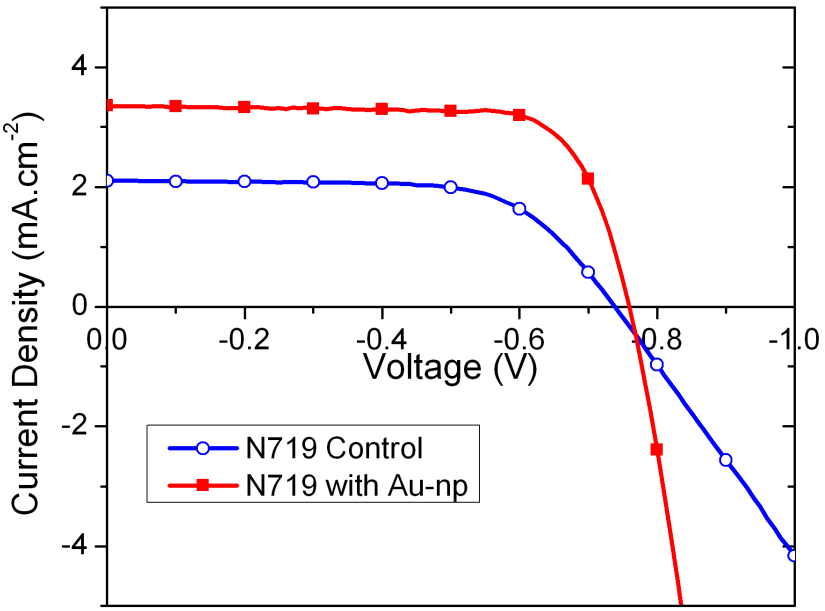

Figure 4.11: Current voltage characterisation of liquid-phase HTM plasmonic hybrid devices. The derived electronic characteristics are defined in table 4.1. . The disparity in R_{series} is an unrelated artifact of device variance.

In figure 4.11 it is shown that the current voltage curves for electrolyte based DSSCs employing N719 [38] ruthenium sensitizer and "robust" iodide/triiodide based liquid electrolyte [39] with 1.1μm thick mesoporous TiO_2:Au-SiO_2 electrodes. Before the photocurrent is discussed, the first and striking observation is that the fill factor of the devices incorporating the Au-SiO_2 nanoparticles is exceptionally good (0.73), and the open-circuit voltage is also high (0.76V). It is thus apparent that the metal nanoparticles are not acting as recombination centers in these solar cells, hence the 3 nm thick silica shells are suitably thick so as to prevent significant electron or hole tunneling onto the metal core. Furthermore, though no rigorous stability measurements have been done, the devices performance remains unaltered with ageing under ambient conditions for more than one month indicating that the silica shells are also sufficiently thick and continuous as to inhibit corrosion from the iodide/triiodide redox couple. Whilst thicker shells were investigated, no significant performance changes were observed with shells up to 8nm in thickness, hence only 3nm thick shells were used for this study. To compare to Standridge et al.[36] they required approximately 7nm thick titania shells deposited by atomic layer deposition to suitably inhibit corrosion form the iodide/triiodide redox couple.

	Current (mA)	Voltage (mV)	Fill Factor (%)	Efficiency (%)
N719	2.14	740	66	1.05
N719 w/ Au-SiO_2 np	3.37	760	76	1.95

Table 4.1: Typical photovoltaic characteristics of 1.1μm thick N719 electrolyte DSCs with and without Au-SiO_2 nanoparticle incorporation, as illustrated in figure 4.11

The photocurrent of the thin, liquid electrolyte based DSSCs is significantly enhanced with the presence of the Au-SiO_2 nanoparticles, indicating that the light harvested from these 'plasmonic' components is directly contributing to the photocurrent generation within the devices. The devices presented had a mesoporous TiO_2 film thickness of ~1.1μm, significantly thinner films than those used in fully optimized electrolyte based DSSCs. The OD was 0.42 (62.0% abs equivalent)for the mesoporous Au-SiO_2 films after sintering, the OD was 0.75 (82.3% abs equivalent) for a conventional TiO_2 film sensitized with N719, and was 1.03 (90.6% abs equivalent) for Au-SiO_2 films sensitized with N719. For optically thick devices (~8μm) the conventional DSSCs generated more photocurrent than the plasmonic DSSCs, indicating that per absorbed photon, the metal nanoparticles are not converting the photons to charge as efficiently as light absorbed in the dye, but nevertheless they are converting a significant fraction of photons to charge. Indeed, it is observed that, likely due to screening effects, the efficiency of the overall devices containing nanoparticles reduces as the thickness approaches a more optimised dye absorption thickness. A comparison of optically thick and thin electrolyte devices and the effect of these screening effects, is given in figure 4.12.

The absorption maximum of the N719 sensitized TiO_2 is around 525nm, similar to the 15nm Au-SiO_2 nanoparticles, making it difficult to differentiate the spectral response from light absorbed in the nanoparticles versus the dye. To circumvent this issue, liquid electrolyte based DSSCs employing the 'black dye' termed N749,[40] which has an absorption peak beyond 600nm, have also been fabricated. In figure 4.13 it is shown the UV-vis absorption spectra normalized at 630nm for ~4 mm thick mesoporous TiO_2 films sensitized with black dye, with and without Au-SiO_2 nanoparticles. For the dye only film, the absorption maximum is at ~630nm, but for the film with both dye and Au-SiO_2 nanoparticles, the absorption becomes much flatter at the top with the peak shifting to 540 nm due to the contribution from the metal nanoparticles.

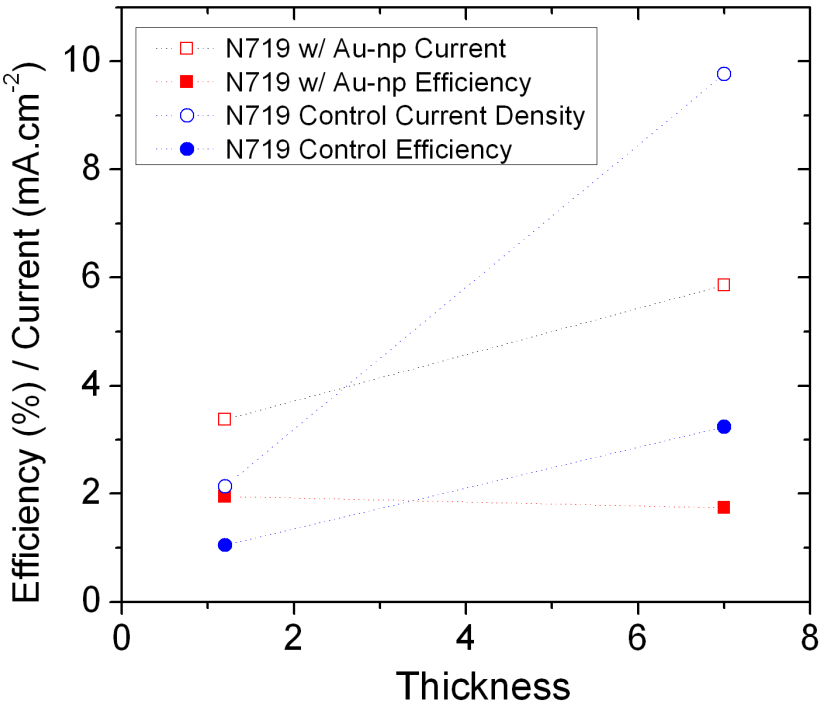

Figure 4.12: Optically thin and thick films with (red) and without (blue) nanoparticle incorporation. Efficiency (filled shape) as a function of film thickness is illustrated. The dependence of photocurrent density (hollow shape) on film thickness is also shown. It is observed that in both control and plasmonic devices the photocurrent generation is enhanced with thicker films (although more significantly for the control devices), but that the efficiency of plasmonic devices is observed to remain or even decrease with increasing substrate thickness.

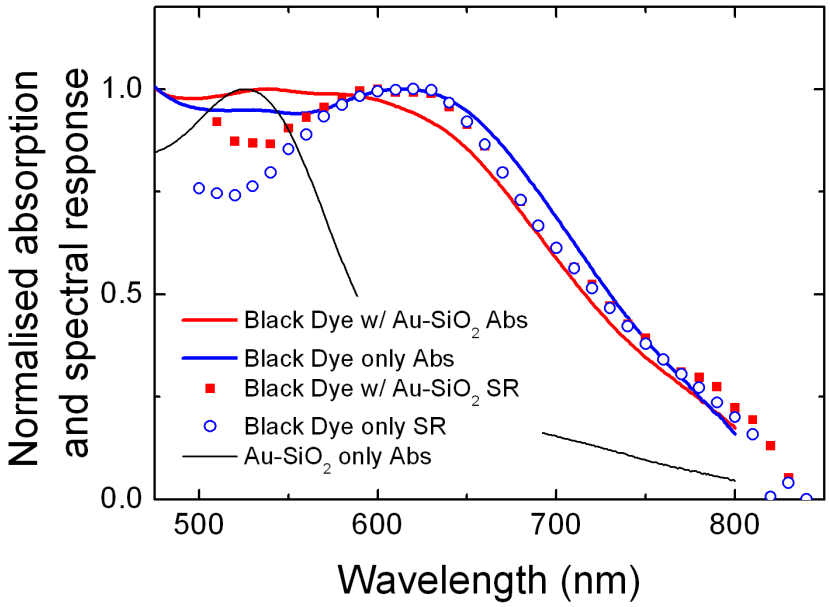

Figure 4.13: Normalised absorption (as 1-transmission-reflectance) and spectral response of electrolyte DSCs sensitized with black dye, with and without Au-SiO_2 nanoparticles. The spectral response and absorption are normalized at 630nm to aid comparison

It is also shown the normalized spectral response of the solar cells incorporating such films. For both with and without the Au-SiO_2 nanoparticles, the spectral response is a maximum at around 630nm, indicating superior conversion from the dye. However, the spectral response is significantly enhanced in the green region of the spectrum (500 to 575nm) indicating that there is indeed photo-conversion from light harvested by the Au nanoparticles.

Liquid electrolyte based DSSCs are a good test-bed to probe and verify the influence of plasmonic effects in the solar cells. However, with the conventional mesoporous films produced for these devices, the dyed cells are optically dense enough to absorb most of the incident light over the absorbing region of the dye, reducing the impact of 'plasmonic' enhancements. Though, it is noted that enhanced light harvesting in thinner cells should result in improved open-circuit voltages and fill factors. In contrast, the solid-state DSSCs employing molecular hole-transporters are severely impaired by a lack of light absorption with conventional dyes, since the performance usually diminishes when the device thickness exceeds 2μm, significantly less than the optical depth of the composite. As noted in section 4.3.4, to probe the influence of the Au-SiO_2 nanoparticles in solid-state DSSCs two approaches have been pursued: The first

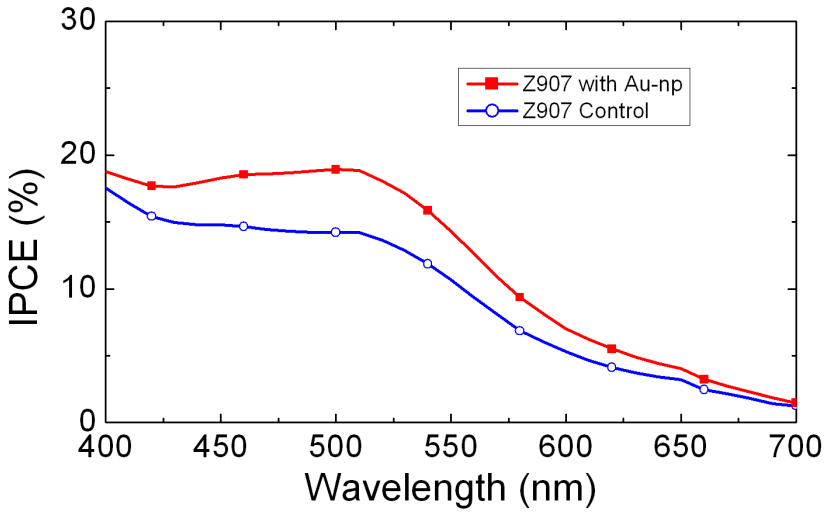

Figure 4.14: Spectral response for typical 1μm thick Z907 sDSC with and without Au-SiO_2 nanoparticles

is identical to that for the electrolyte based cell where the nanoparticles were mixed into the TiO_2 paste prior to film fabrication. For the second approach an ethanol based nanoparticle solution was spincoated into conventional dye-sensitized mesoporous TiO_2, prior to coating with the hole-transporter. For these experiments it was found that the second method gave superior results and the findings are presented below.

Figure 4.14 shows the spectral response for typical 1μm thick solid-state DSSCs fabricated with only Z907 sensitizer, and also with the incorporation of Au-SiO_2 nanoparticles (core 15nm, shell 3nm). The overall incident photon-to-electron conversion efficiency (IPCE) is increased considerably in the visible region with the presence of the Au-SiO_2 nanoparticles, indicating photocurrent generation from light harvested by the Au nanoparticles. Figure 4.15 shows the current voltage curves measured under simulated AM1.5 sun light for cells with and without Au-SiO_2 nanoparticles, showing curves for both typical and the best performing cells from each type. Similarly to the electrolyte cells, with the inclusion of the core-shell nanoparticles there is no degradation, neither in fill factor nor open-circuit voltage. More notably still there is a significant increase in short-circuit photocurrent, with the best 'plasmonic' cell exhibiting a power conversion efficiency of 4.0%.

These solar cells were fabricated with Z907 purchased from Dyesol, used as received. Solid-

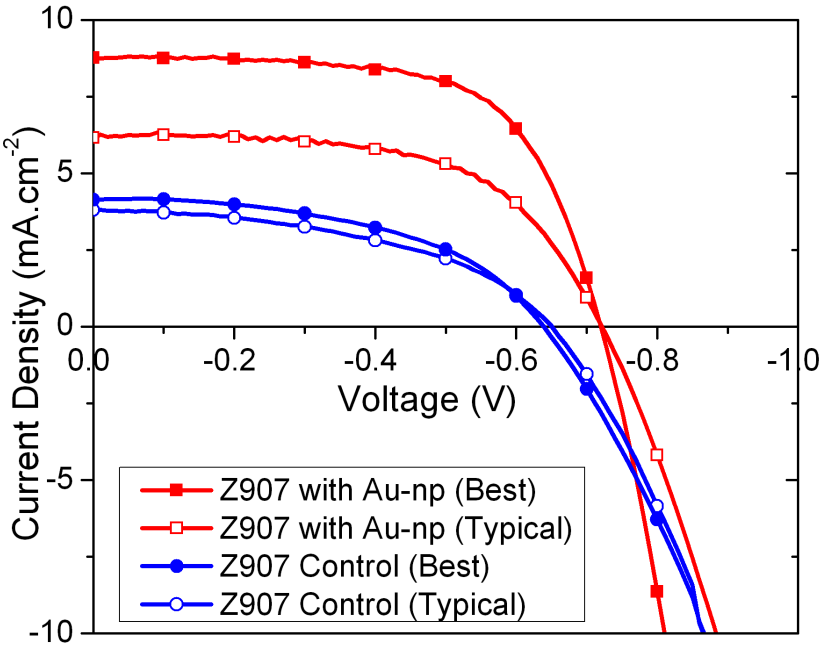

Figure 4.15: Current voltage characterisation of solid state plasmonic hybrid devices

state DSSCs fabricated with this specific dye have been found to be exceptionally variable, and this is further compounded with the incorporation of the metal nanoparticles. To verify that the enhancements presented in figures 4.11 and 4.15 are a fair representation there were fabricated extensive series of devices and figure 4.16 shows the solar cell performance parameters for a series of just over 60 cells for both those sensitized with Z907-only and also with the incorporation of Au-SiO_2 nanoparticles and dye. The average photocurrent is observed to increase from 3.0 $\pm$ 0.8 to 5.0 $\pm$ 2 mAcm-2. The open-circuit voltage remains unchanged but the fill factor increases on average from 0.51 $\pm$ 0.13 to 0.59 $\pm$ 0.06 and the overall power conversion efficiency increases from 1.2 $\pm$ 0.5 % to 2.2 $\pm$ 1.0%. The optical density in the films increases on average from 0.24 to 0.42 which represents a 46% increase in light absorption. The photocurrent increase is approximately 67% which is more than expected, but within the margin of error. The increase in fill factor is unexpected, and significant, indicating that the inclusion of the Au-SiO_2 nanoparticles may have a broader influence than purely enhancing the light absorption. These 'beyond expected' observed enhancements with the inclusion of Au nanoparticles are not unprecedented. Chen et al. observed increases in fill factor of polymer devices with Au nanoparticles sparsely coated on one of the electrodes[41] and Pegg et al. recently reported significant increases in

V_{OC} in organic devices incorporating surface-oxidized Au nanocrystals.[42] Though the origin of the improvements in fill factor observed here are not certain, it is suspected they may be related to improvements in the spiro-OMeTAD capping layer due to the presence of the SiO_2-Au nanoparticles on top of the TiO_2 film, reducing shorting points between the top silver electrode and the mesoporous TiO_2. To clarify this, a number of control devices were fabricated with purely SiO_2 nanoparticles coated on top (no gold within), and there were no observed systematic enhancements in fill factor or voltage, nor indeed photocurrent, with respect to the normal controls.

4.3.6 Spectroscopy

Quasi steady-state and transient photoinduced absorption spectroscopy were performed for sample characterization. Photo-induced absorption (PIA) spectroscopy is a quasi-cw pump-probe technique sensitive to the absorption of photo-generated long-lived species (from μs to ms). Pump excitation was provided by diode laser at 560nm. A 4mm diameter laser beam was realized using a telescope in order to guarantee a good overlap with the probe beam. The probe used was generated from a 100W halogen lamp. The changes in transmission under photoexcitation, detected by a Si and InGaAs photodetector, were measured by a lock-in amplifier referenced to the modulation frequency. Changes were then normalized to the unmodulated transmission for every wavelength (ΔT/T). All samples were measured in a vacuum chamber. The ultra fast transient absorption spectroscopy was carried out as described elsewhere.[43]

The film under study was photoexcited by a short "pump" pulse and its subsequent dynamic evolution detected by measuring the transmission (T) changes of a delayed "probe" pulse as a function of pump-probe delay time τ given by the differential transmission:

$$\Delta T/T = \frac{T_{pump-on} - T_{pump-off}}{T_{pump-off}} \tag{4.7}$$

The pump pulses were centered at 555 nm with spectral width of 20 nm, time-duration of ~180 fs, an energy of 90nJ/pulse; the beam spot size was about 250 µm and a white-light supercontinuum served as the probe pulse. A short-pass filter with 760-nm cutoff wavelength was used to filter out the residual 800 nm pump light thus limiting the probing window to the 450-760 nm region.

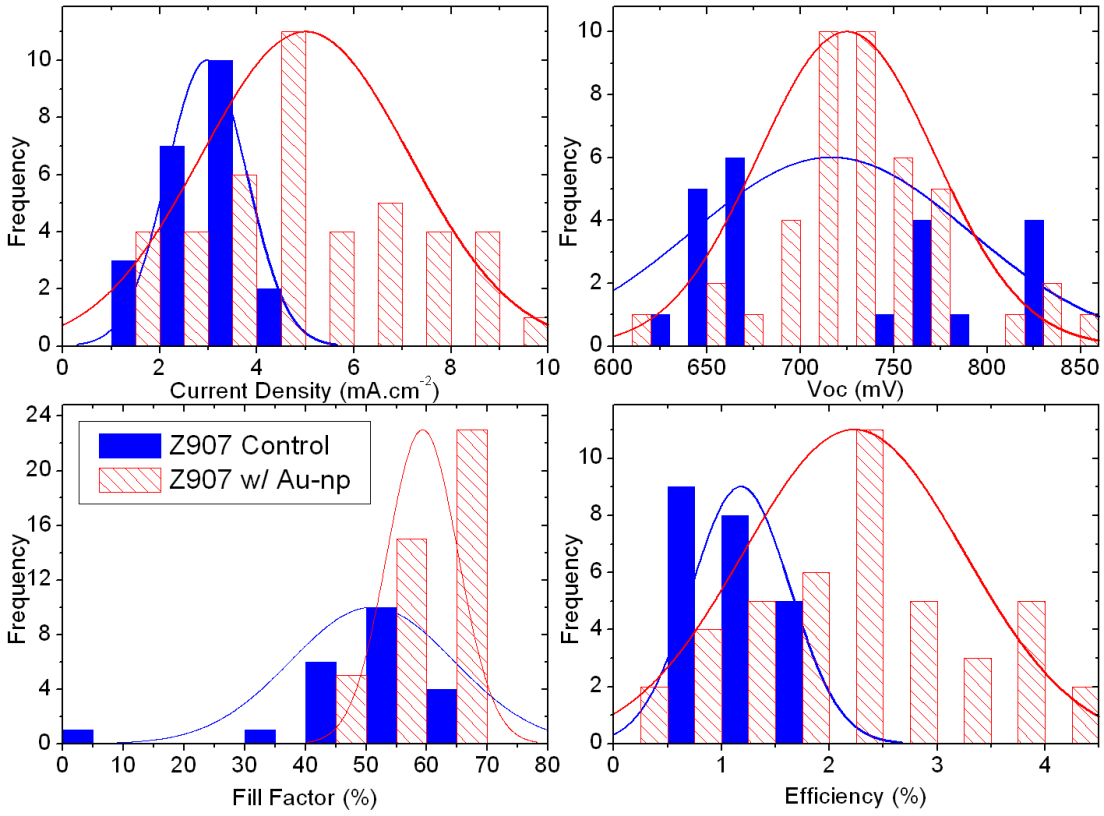

Figure 4.16: Histograms showing the number of devices versus the electrical performance parameters (**a** Jsc, **b** Voc, **c** FF, and **d** η) extracted from JV curves measured under AM1.5 simulated sun light of 100 mWcm-2 for a series of around 60 devices for both dye-only and dye with Au-SiO2 nanoparticles. The histograms are fitted with normal distribution curves for the purpose of interpretation. The optical density of the Au-SiO2 nanoparticles within the solid-state DSSCs was around 0.24 and the optical density due to Z907 sensitization was around 0.18, with an average film thickness of 1.2µm. All numerical errors quoted are standard deviations of the mean.

Figure 4.17 shows the results of photo-induced absorption (PIA) spectroscopy and ultra-fast transient absorption spectroscopy on the solid-state DSSCs presented in figure 4.15, with the metallic electrodes peeled off to enable probing in transmission mode. Figure 4.17**a** shows the in-phase quasi-continuous wave (cw) photoinduced absorption spectra from a standard Z907-only device and a device incorporating the Au-SiO_2 nanoparticles. For both samples, at wavelengths shorter than 600nm the tail of the photo-bleach (PB) of the dye can be observed. The band peaking around 830nm is assigned to the oxidized dye while the broad band in the IR is assigned to the oxidized Spiro-OMeTAD. Finally, the weak band around 620nm can arise from the overlap of the two previous absorption species. These spectra indicate an overall enhancement of the PIA signal from the sample with the Au-SiO_2 nanoparticles as compared to the Z907-only device in the μs-ms time window. It is worth mentioning that by estimating the charge recombination lifetime by the ratio of the in-phase to out-of phase PIA signal, as described by Westerling et al.,[44] a marginal increase in the signal lifetime can also be estimated, from 1.20 to 1.49 ms for the device incorporating the Au-SiO_2 nanoparticles as compared to the Z907-only device. Since the PIA signal is "time integrated" it is proportional to the density of generated excitations and to their lifetime, hence it is difficult to fully disentangle the contribution of these two factors to the measured spectra.

To look at the early time photo-induced species and to probe the charge generation in more detail, ultrafast transient absorption spectroscopy in the fs-ps time range was performed. Figure 4.17**b** shows the spectra for the fractional change in transmission 400 fs after excitation from the Z907-only device and the device incorporating the Au-SiO_2 nanoparticles. For the Z907-only device, at wavelengths shorter than 610 nm a positive fractional change is observed which is assigned to a photobleaching (PB). At longer wavelengths a broad photo-induced absorption (PA) band appears. For the device incorporating the Au-SiO_2 nanoparticles a positive fractional change is observed in the spectral range between 490nm and 600nm; two photo-induced absorption bands can be observed at wavelengths shorter than 490nm and longer than 600nm and the signal is generally over 3 times as intense than the dye-only sample. At 400fs after excitation the photobleaching band for the Z907-only device can be ascribed to the presence of singlet excited states and oxidized species on the dye where the dye has already undergone ultrafast electron transfer into the TiO_2.[45] In contrast, the sample containing both the dye and Au-SiO_2 nanoparticles could have a contribution from the photobleaching of both the dye

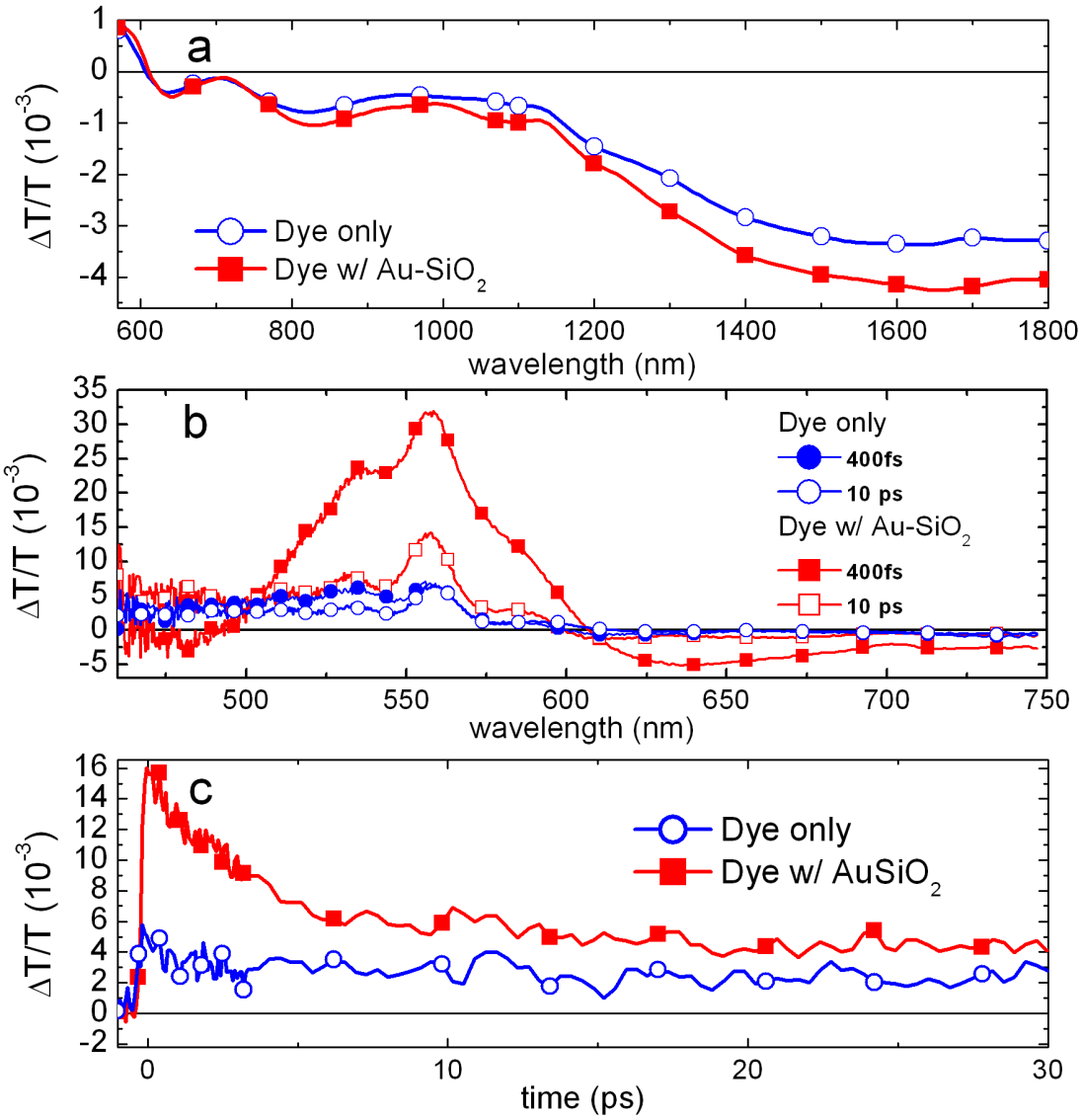

Figure 4.17: Spectroscopic characterization of the Z907-only device and the device incorporating the Au-SiO_2 nanoparticles. **a** in-phase quasi-cw photoinduced absorption (PIA) spectra from the dye-only device (blue line) and the device including Au nanoparticles (red line). Excitation at 560nm, power intensity 40mW/cm2. **b** Fractional change in transmission from the dye-only device (blue line) and the device including the Au nanoparticles (red line) taken 400fs and 10ps after excitation, respectively (note: 50ps response is near indistinguishable from 10ps). **c** Transient absorption kinetics at 520 nm. Note that the transient absorption signals at 660nm, where only PA bands are observed, showed identical trends to the signals at 520 nm. Excitation was at 555nm. *PIA data courtesy of A-M. Petrozza, Milano 2010*

and the Au nanoparticles. The molecular absorption coefficient of 15nm Au nanoparticles is on the order of 10^9 to 10^{10} $M^{-1}cm^{-1}$ as compared to the dye, in this case 1.3 10^4 $M^{-1}cm^{-1}$. This implies that the photobleaching of the photoexcited Au nanoparticles is expected to be much stronger than that of the dye alone. On top of this, the Au nanoparticles are expected to show a photo induced absorption at wavelengths below 500nm, which is indeed observed for the Au-SiO_2 samples. Comparing the 400fs spectrum from this sample with the spectra measured by Watanabe et al.[46] from 13nm Au nanoparticles, one can assign the photobleaching band to the photobleaching of the plasmonic mode from the Au nanoparticles. It is very interesting to notice in figure 4.17**c** that after about 10 ps the transient absorption spectrum from the device including the Au nanoparticles undergoes a rapid decay, becoming almost identical in shape, but about twice as intense, as the Z907-only device. It is noted that the excitation power is the same for the two samples. This suggests that the presence of the Au nanoparticles has increased the dye photobleaching signal and thus enhanced the charge generation.

In figure 4.17**c** the transient absorption kinetics of the photobleaching band sitting at 520 nm is probed from the same samples as above. At very early times the sample with Au-SiO_2 nanoparticles shows a much more intense signal than the Z907-only sample, as expected from the results in figures 4.15 and 4.14. A rapid signal decay can be observed within the first 10 ps after which a plateau is reached. Fitting the initial rapid decay with a simple mono-exponential function gives a decay time of about 5 ps. It is noted that the electron-phonon relaxation time for 13 to 15nm Au nanoparticles is in the range of 3ps which is very close to the rapid decay time observed here. Therefore the TA features in the first 10 ps can be assigned to the hot electron population relaxation.

The precise means by which charge is generated from light harvested by the nanoparticles is still not apparent. From the UV-Vis measurements illustrated in figure 4.6, it is known that scattering is minimal and can therefore be neglected in this system. The two remaining possibilities are discrete energy transfer from the plasmon mode to the dye excited state, or direct near field coupling. For either of these to occur the energy must transfer prior to de-coherence of the plasmon mode. The total plasmon resonance damping constant, T, can be estimated by a simple model as:

$$2/T = \pi c\Gamma = 1/T_1 + 1/T_2 \tag{4.8}$$

where Γ is the plasmon absorption band width, T1 is the population relaxation time (radiative and non-radiative processes) and T2 is the pure dephasing time, i.e. the time taken to change the plasmon wave vector but not its energy. From the plasmon absorption band of Au-SiO_2 core shell nanoparticles on TiO_2 (post thermal sintering and chemical treatment) one can estimate a total plasmon resonance damping of the order of 10 fs which is much shorter than the inelastic electron-phonon relaxation probed by transient absorption. This suggests that plasmon enhanced photocurrent generation can be observed only if the photoexcited dye can undergo electron transfer into the TiO_2 in the first tens of femtoseconds; after this time window, resonant plasmons are very likely to loose their coherence. Since there is ultra fast electron transfer from photoexcited Z907 into TiO_2[47] and the solar cell measurements indicate an enhancement in charge generation in the presence of Au nanoparticles, it is feasible that effective charge generation does occur prior to the dephasing times in the nanoparticles.

In light of these results, further studies can be undertaken in order to fully understand and control the nature of the damping and loss mechanisms. Specifically the influence of the metal nanoparticles on the dye injection time can be investigated to maximize charge generation from plasmon light harvesting antenna.

4.4 Conclusions

In summary, this work has outlined a successful strategy for incorporating metal nanoparticles with strong surface plasmon resonance into dye-sensitized solar cells which overcomes four main issues of introducing metal into the bulk of a solar cell: charge recombination within the metal, thermal stability during processing, chemical stability, and control of metal nanoparticle dye chromophore separation to inhibit non-radiative quenching. Most significantly this new plasmonic photovoltaic system has led to enhanced light absorption and photocurrent generation in dye-sensitized solar cells. Through optical spectroscopy it has been identified that for this system, plasmon enhanced photogeneration of charge carriers can only occur when the electron transfer from the photoexcited dye to the TiO_2 is faster than around 10 fs. Speeding up electron transfer from the dye and inhibiting possible collisions, which may change the plasmon wave vector in the metal nanoparticles, are key issues to further efficiency enhancements with this concept. The readily tunable optical properties of metallic nanoparticles, through use of struc-

tures such as nanobars,[48] nanostars,[49] or other complex shapes, provides extensive scope for further work to fully optimise the technology and greatly develop an understanding of charge generation in this new class of solar cells. Finally, the incorporation of thermally and chemically stable core-shell metal nanoparticles into other forms of solar cells, such as other organic and thin film technologies should be readily adopted.

Publication:

The concept, execution and results outlined in this chapter have been published in part in Nano Letters in 2011[50] as well as presented at conference; this is detailed further on page 118.

References

[1] D. Rayleigh, "On the light from the sky, its polarization and colour," *Phil. Mag.*, vol. 61, pp. 107–20 and 274–9, 1871.

[2] D. Rayleigh, "On the electromagnetic theory of light," *Phil. Mag.*, vol. 12, pp. 81–101, 1881.

[3] P. Debye, "Zerstreuung von Roentgenstrahlen," *Ann. Phys.*, vol. 46, pp. 809–823, 1915.

[4] D. Pines and D. Bohm, "A Collective Description of Electron Interactions: II. Collective vs Individual Particle Aspects of the Interactions," *Physical Review*, vol. 85, pp. 338–353, June 1952.

[5] D. Pines, "Collective Energy Losses in Solids," *Reviews of Modern Physics*, vol. 28, no. 3, pp. 184–198, 1956.

[6] R. H. Ritchie, "Plasma Losses by Fast Electrons in Thin Films," *Physical Review*, vol. 184, no. 5, pp. 874–881, 1957.

[7] J. B. Powell and C. J. Swan, "Effect of Oxidation on the Characteristic Loss Spectra of Aluminum and Magnesium," *Physical Review*, vol. 118, no. 3, pp. 640–643, 1960.

[8] J. Vincent and R. Silcox, "Dispersion of Radiative Surface Plasmons in Aluminum Films by Electron Scattering," *Physical Review Letters*, vol. 31, no. 25, pp. 1487–1490, 1973.

[9] R. Pettit, J. B Silcox, and R. Vincent, "Measurement of surface-plasmon dispersion in oxidized aluminum films," *Physical Review B*, vol. 11, no. 8, pp. 3116–3123, 1975.

[10] J. McPhillips, A. Murphy, M. P. Jonsson, W. R. Hendren, R. Atkinson, F. Hook, A. V. Zayats, and R. J. Pollard, "High-Performance Biosensing Using Arrays of Plasmonic Nanotubes," *ACS Nano*, vol. 4, pp. 2210–2216, 2010.

[11] M. L. Brongersma and V. M. Shalaev, "Applied physics. The case for plasmonics.," *Science*, vol. 328, pp. 440–1, Apr. 2010.

[12] A. Polman, "Plasmonics Applied," *Science*, no. November, pp. 868–869, 2008.

[13] H. A. Atwater and A. Polman, "Plasmonics for improved photovoltaic devices," *Nature Materials*, vol. 9, pp. 205–213, 2010.

[14] J. A. Schuller, E. S. Barnard, W. S. Cai, Y. C. Jun, J. S. White, and M. L. Brongersma, "Plasmonics for extreme light concentration and manipulation (vol 9, pg 193, 2010)," *Nature Materials*, vol. 9, 2010.

[15] K. R. Catchpole and a. Polman, "Design principles for particle plasmon enhanced solar cells," *Applied Physics Letters*, vol. 93, no. 19, p. 191113, 2008.

[16] T. W. Ebbesen, C. Genet, and S. I. Bozhevolnyi, "Surface-plasmon circuitry," *Physics Today*, vol. 61, no. 5, p. 44, 2008.

[17] M. Hentschel, M. Saliba, R. Vogelgesang, H. Giessen, a. P. Alivisatos, and N. Liu, "Transition from isolated to collective modes in plasmonic oligomers.," *Nano Letters*, vol. 10, pp. 2721–6, July 2010.

[18] S. Maier, *Plasmonics: Fundamentals and Applications*. Springer, 2007.

[19] S. Hayashi, K. Kozaru, and K. Yamamoto, "Enhancement of Photoelectric Conversion Efficiency by Surface Plasmon Excitation: A Test with an Organic Solar Cell," *Physical Review*, vol. 79, no. 9, pp. 763–767, 1991.

[20] S. Pillai, K. R. Catchpole, T. Trupke, and M. A. Green, "Surface plasmon enhanced silicon solar cells," *Journal of Applied Physics*, vol. 101, p. 093105, May 2007.

[21] K. Nakayama, K. Tanabe, and H. A. Atwater, "Plasmonic nanoparticle enhanced light absorption in GaAs solar cells," *Applied Physics Letters*, vol. 93, p. 121904, 2008.

[22] H. R. Stuart and D. G. Hall, "Enhanced dipole-dipole interaction between elementary radiators near a surface," *Physical Review Letters*, pp. 5663–5666, 1998.

[23] D. M. Schaadt, B. Feng, and E. T. Yu, "Enhanced semiconductor optical absorption via surface plasmon excitation in metal nanoparticles," *Applied Physics Letters*, vol. 86, p. 063106, 2005.

[24] M. Ihara, K. Tanaka, K. Sakaki, I. Honma, and K. Yamada, "Enhancement of the absorption coefficient of cis-(NCS)(2) bis(2,2'-bipyridyl-4,4'-dicarboxylate)ruthenium(II) dye in dye-sensitized solar cells by a silver island film," *Journal of Physical Chemistry B*, pp. 5153–5157, 1997.

[25] C. Hagglund, M. Zach, B. Kasemo, C. Hägglund, and M. Zäch, "Enhanced charge carrier generation in dye sensitized solar cells by nanoparticle plasmons," *Applied Physics Letters*, vol. 92, no. 1, p. 013113, 2008.

[26] K. Ishikawa, C. J. Wen, K. Yamada, T. Okubo, K. I. Shikawa, and C.-j. W. En, "The photocurrent of dye-sensitized solar cells enhanced by the surface plasmon resonance," *Journal of Chemical Engineering of Japan*, vol. 37, no. 5, pp. 645–649, 2004.

[27] B. P. Rand, P. Peumans, and S. R. Forrest, "Long-range absorption enhancement in organic tandem thin-film solar cells containing silver nanoclusters," *Journal of Applied Physics*, vol. 96, pp. 7519–7526, 2004.

[28] A. P. Kulkarni, K. M. Noone, K. Munechika, S. R. Guyer, and D. S. Ginger, "Plasmon-Enhanced Charge Carrier Generation in Organic Photovoltaic Films Using Silver Nanoprisms," *Nano Letters*, vol. 10, pp. 1501–1505, 2010.

[29] M. Westphalen, U. Kreibig, J. Rostalki, H. Luth, and D. Meissner, "Metal cluster enhanced organic solar cells," *Solar Energy Materials & Solar Cells*, vol. 61, pp. 97–105, 2000.

[30] L. M. LizMarzan, M. Giersig, and P. Mulvaney, "Synthesis of nanosized gold-silica core-shell particles," *Langmuir*, pp. 4329–4335, 1996.

[31] B. V. Enustun and J. Turkevich, "Coagulation of Colloidal Gold," *Journal of the American Chemical Society*, vol. 85, p. 3317, 1963.

[32] N. G. Liu, B. S. Prall, and V. I. Klimov, "Hybrid gold/silica/nanocrystal-quantum-dot superstructures: Synthesis and analysis of semiconductor-metal interactions," *Journal of the American Chemical Society*, pp. 15362–15363, 2006.

[33] W. Ostwald, *Lehrbuch Der Allgemeinen Chemie, Volume 2, Part 1.* Engelmann, 1893.

[34] C. F. Bohren and D. R. Huffman, *Absorption and scattering of light by small particles.* New York: Wiley, 1983.

[35] S. Link and M. a. El-Sayed, "Spectral properties and relaxation dynamics of surface plasmon electronic oscillations in gold and silver nanodots and nanorods," *Journal of Physical Chemistry B*, vol. 103, pp. 8410–8426, Oct. 1999.

[36] S. D. Standridge, G. C. Schatz, and J. T. Hupp, "Toward Plasmonic Solar Cells: Protection of Silver Nanoparticles via Atomic Layer Deposition of TiO2," *Langmuir*, vol. 25, pp. 2596–2600, 2009.

[37] J. C. Fuggle and N. Må rtensson, "Core-level binding energies in metals," *Journal of Electron Spectroscopy and Related Phenomena*, vol. 21, pp. 275–281, 1980.

[38] Y. Tachibana, K. Nazeeruddin, M. Gr, D. R. Klug, and J. R. Durrant, "Electron injection kinetics for the nanocrystalline TiO2 films sensitised with the dye (Bu4N)2Ru(dcbpyH)2(NCS)2," *Chemical Physics*, vol. 285, pp. 127–132, 2002.

[39] P. Wang, C. Klein, R. Humphry-Baker, S. M. Zakeeruddin, and M. Gratzel, "Stable >8% efficient nanocrystalline dye-sensitized solar cell based on an electrolyte of low volatility," *Applied Physics Letters*, vol. 86, no. 12, p. 123508, 2005.

[40] M. K. Nazeeruddin, P. Pechy, T. Renouard, S. M. Zakeeruddin, R. Humphry-Baker, P. Comte, P. Liska, L. Cevey, E. Costa, V. Shklover, L. Spiccia, G. B. Deacon, C. A. Bignozzi, and M. Gratzel, "Engineering of efficient panchromatic sensitizers for nanocrystalline TiO2-based solar cells," *Journal of the American Chemical Society*, vol. 123, pp. 1613–1624, 2001.

[41] F.-C. Chen, J.-L. Wu, C.-L. Lee, Y. Hong, C.-H. Kuo, and M. H. Huang, "Plasmonic-enhanced polymer photovoltaic devices incorporating solution-processable metal nanoparticles," *Applied Physics Letters*, vol. 95, p. 013305, 2009.

[42] L. J. Pegg, S. Schumann, and R. A. Hatton, "Enhancing the Open-Circuit Voltage of Molecular Photovoltaics Using Oxidized Au Nanocrystals," *ACS NanoNano*, vol. 4, pp. 5671–5678, 2010.

[43] G. Cerullo and S. De Silvestri, "Ultrafast optical parametric amplifiers," *Review of Scientific Instruments*, vol. 74, pp. 1–18, 2003.

[44] M. Westerling, C. Vijila, R. Osterbacka, and H. Stubb, "Optical studies of excited-state relaxation in poly(9,9-dihexylfluorene-co-benzothiadiazole)," *Physical Review B*, vol. 67, p. 195201, 2003.

[45] B. Wenger, M. Gratzel, J. E. Moser, Wenger, Gratzel, and M. Je, "Rationale for kinetic heterogeneity of ultrafast light-induced electron transfer from Ru(II) complex sensitizers to nanocrystalline TiO2," *Journal of the American Chemical Society*, vol. 127, pp. 12150–12151, Sept. 2005.

[46] K. Watanabe, D. Menzel, N. Nilius, and H. J. Freund, "Photochemistry on metal nanoparticles," *Chemical Reviews*, vol. 106, pp. 4301–4320, 2006.

[47] P. Tiwana, P. Parkinson, M. B. Johnston, H. J. Snaith, and L. M. Herz, "Ultrafast Terahertz Conductivity Dynamics in Mesoporous TiO2: Influence of Dye Sensitization and Surface Treatment in Solid-State Dye-Sensitized Solar Cells," *Journal of Physical Chemistry C*, vol. 114, pp. 1365–1371, 2010.

[48] B. J. Wiley, Y. C. Chen, J. M. McLellan, Y. J. Xiong, Z. Y. Li, D. Ginger, and Y. N. Xia, "Synthesis and optical properties of silver nanobars and nanorice," *Nano Letters*, vol. 7, pp. 1032–1036, 2007.

[49] P. S. Kumar, I. Pastoriza-Santos, B. Rodriguez-Gonzalez, F. J. de Abajo, and L. M. Liz-Marzan, "High-yield synthesis and optical response of gold nanostars," *Nanotechnology*, vol. 19, no. 1, p. 015606, 2008.

[50] M. D. Brown, T. Suteewong, Kumar, V. D'Innocenzo, A. Petrozza, M. M. Lee, U. Wiesner, and H. J. Snaith, "Plasmonic Dye-Sensitized Solar Cells Using Core-Shell Metal-Insulator Nanoparticles," *Nano Letters*, vol. 11, pp. 438–445, Feb. 2011.

Chapter 5

Ongoing projects

Describing work undertaken during the course of the preparation of this thesis that is still in progress or has been speculated upon, but not yet completed. Some of this work is directly or indirectly related to the research of the previous chapters.

Following from the energy transfer work of chapter 3 a system of cosensitization is investigated of a two-dye system in which one has no charge injection characteristics, therefore depending upon energy tranfer to function.

An ultra-fast sintering route using an infra-red pulse directly heating the titania paste is developed, investigating the feasibility of the nanostructure incorporation discussed in chapter 4 as an antennae to focus the incoming energy.

Finally, work done on functional devices not incorporating a traditional hole transport medium is discussed.

5.1 Deriving current from non-injecting dyes

Following the realisation in chapter 3 of a two dye system in which the light absorption and charge injection properties are to some degree separated, the clear follow-up work is the implementation of a system wherein the actions of light absorption and current generation are entirely abstracted. To this end, a non-injecting porphyrin dye was fabricated at request by a dye synthesis group under Dr Neil Robertson at the University of Edinburgh. Previously a perylene dye has been reported [?] as functional in DSC applications when acting as a 'relay' dye when suspended in the electrolyte HTM; perylene-3,4,9,10-tetracarboxylic diimide (PTCDI),[1] shows a strong visible absorption profile, but is unable to adsorp to a metal oxide surface or directly inject the it's photoexcited carriers. The Robertson group has synthesised a perylene molecule containing a functional -COOH group theoretically allowing adsorption to a titania mesostructure whilst precluding direct charge injection. Figure 5.2 (top panel) shows this mid-visible absorption profile.

The altered perylene was fabricated to be entirely unable to inject of the charge carriers generated, as such the excitations of the molecule are simply allowed to return to their ground state via fluorescence. This injection-limitation was purposed such that the complementary dye molecule would be obliged to control all of the carrier injection for the system and so clearly indicate if energy transfer were occuring from the porphyrin to the acceptor. The acceptor molecule used in this investigation was again TT1, having previously shown its energy relay amptitude both previously within this thesis and within contemporary literature. Devices were fabricated consistently with the methods defined in chapter 2 and the TT1 preparation as outlined in chapter 3. The altered PTCDI was found to not satisfactorily dissolve in a number of typical solvents used in dye preparation and simply formed suspensions. The only effective solvent found dimethylformamide (DMF) which led to the neccesity of the porphyrin dye being adsorbed to the substrate before the TT1 to prevent the secondary application of the DMF desorbing the first dye. Although chloroform has been used as a solvent for this dye,[?] the apparently non-ideal nature of the functionalisation impedes the surface adsorption to the titania substrate. The chemical structure of the fabricated perylene diimide is shown in figure 5.1 which illustrates the incorporated anchoring carboxylic group. Furthermore, the sensitization order may have some effect on the final performance of a cosensitized device as, for a finite volume dye

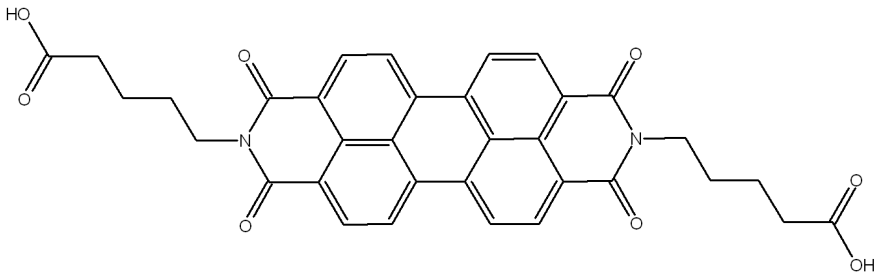

Figure 5.1: Molecular structure of perylene diimide, designed to be visibly absorptive but with minimal or no injection characteristics. *Molecule synthesis and structural image courtesy of T. E. Hewat, Edinbrugh, 2011*

molecule, there can only be a finite number of adsorption sites and the first dye solution applied is assumed to fill the majority of these (preclulding the adsorption of a spacer molecule such as cheno-deoxycholic acid) and the second will displace sites dependant upon its solvent and dye time. It is also theorised that, to some degree, aggregation of the dye molecules may occur, wherein once a monolayer has been established further dye molecules may attach to the dye molecules instead of to the substrate. As such, in this system it would be considered benificial for the injection molecules to adsorp first to ensure direct anchoring to the substrate; however, due to the solvent limitations and indeed the structure of perylene itself, a non-ideal system has been implemented at present.

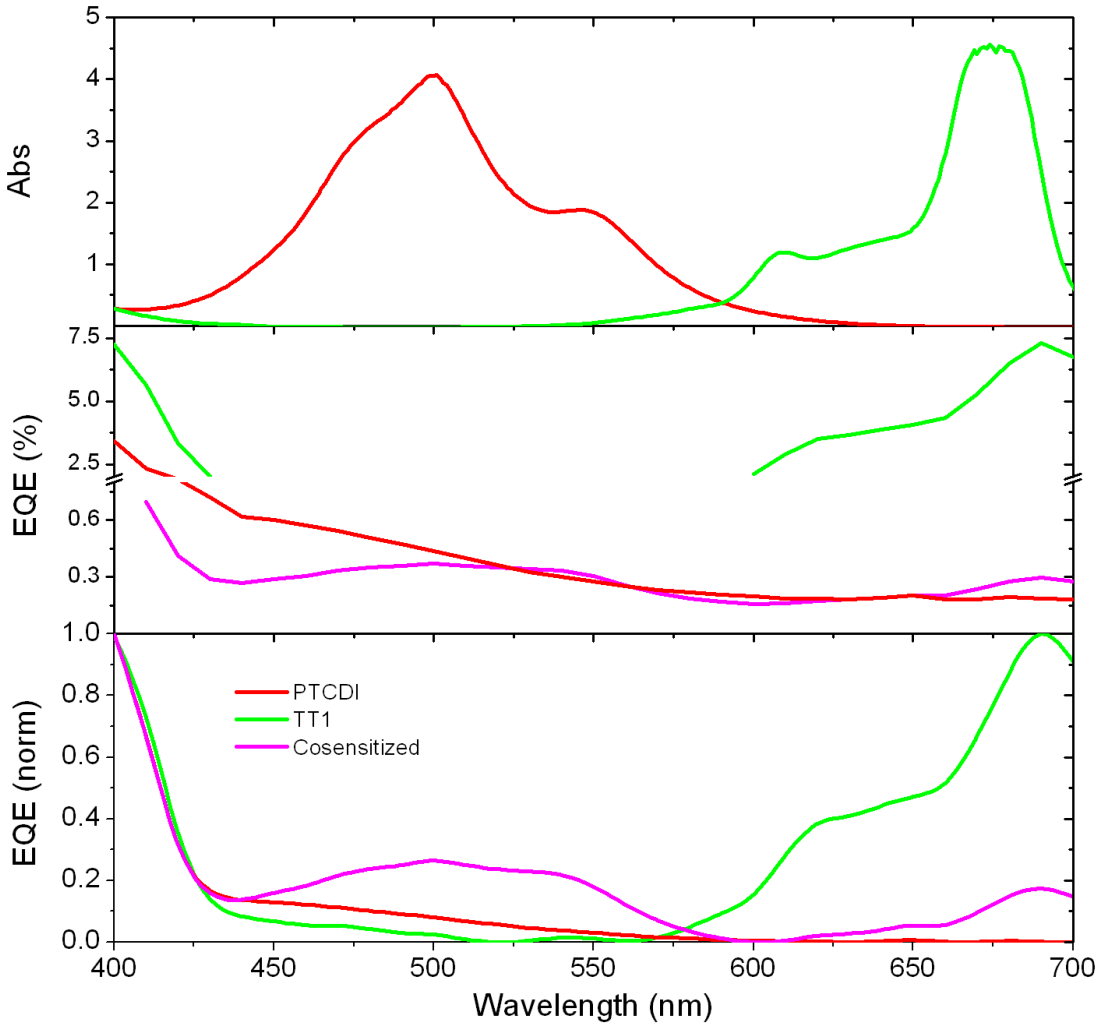

Figure 5.2: Top Panel: Absorption profile for perylene diimide in solvent (H_2O with 0.5μM NaOH), compared with TT1 in solvent (ethanol)

Middle Panel: External quantum eficiency spectrum for perylene coadsorped with TT1. Note the scale break between 0.8% and 2.5%, allowing the rendition of all spectra with some clarity.

Bottom Panel: Normalised external quantum efficiency spectrum, the featureless response of the lone perylen device is typical of a TiO_2 susbtrate infiltrated with spiro and is simply exaggerated by the normalisation applied to all of the spectra. The cosensitized plot shows action from spectral areas typical of both the perylene and pthalocyanine molecules, suggesting that the non-injecting perylene molecule may be attaining functionality via resonant energy transfer to the TT1 molecule.

Figure 5.2 shows the absorption profile of the perylene and IR dye (top panel) and the absolute (middle panel) and normalised (bottom panel) spectral response for devices containing the two dyes singly- and co-sensitized. For the singly-sensitized devices the quantum efficiency plots show a typical near-IR response for the pthalocyanine TT1 and a featureless slope for the PTCDI, characteristic of an unsensitized TiO_2 mesostructure infiltrated with spiro. Upon cosensitization the profile of the pthalocyanine (690nm peak) is reduced considerably, but is joined by a mid-visible (520nm peaked) response indicative of action from the perylene, a response seemingly inconsistent with the summation of the two dye responses. This is clarified by the normalised spectra of the bottom panel of figure 5.2. This indicates that the light being absorbed in this wavelength regime is not being dissipated in the same fashion as when the perylene is adsorbed singly and that, as in the FRET work of chapter 3 the second molecule, in this case the TT1, provides a route for energy transfer that can result in generated photocurrent in the device.

The results achieved from this system show promise for extending the system of energy transfer via coadsorption but it has proven difficult, likely due to the problems of dissolution and adsorption on the part of the perylene, to fabricate highly efficient DSCs capable of displaying conclusively the efficacy of the concept. As a comparable system has been fabricated by Hardin et al in electrolyte devices wherein the perylene (PTCDI) acts as a abstracted relay dye not adsorbed to the surface, the system indeed appears effective, but this route appears dependant upon the fabrication of dye molecules with a more surface adsorptive nature. As noted in chapter 3, if the light harvesting and carrier injection aspects of current generation were seperated these dyes could be more heavily specialised to idealise this system.

5.2 Incorporation of further plasmonic nanostructure geometries

Chapter 4 discusses the nascent field of plasmonic hybrid devices and the work accomplished via the incorporation of gold spheres coated in silica. The system outlined in that chapter is known to be conceptually applicable to further variations of topographies and metal-dielectric combinations. This has already been investigated to some extent by Belcher et al. who have fabricated electrolyte devices incorporating silver-titania nanospheres.[2] The system is also speculated to be entirely adaptable to the incorporation of more complex nanoparticle geometries.

5.2.1 Ultra-fast sintering of titania substrates through near-IR pulse techniques

Worsely et al. have recently demonstrated a method of sintering titania films adhered to the surface of metallic substrates.[3] This concept is dependant upon the tranmission of IR radiation directly into the metal substrate which acts as a built-in hot plate, sintering the titania. Significantly, this method allows energy transmission at such a high rate that complete, effective sinter of the films can be achieved in around 12.5 seconds, in contrast to the traditionally sintered films (see section 2.2) which generally takes in excess of 4 hours when the cool down of the hot plate is included. This system does not appear immediately transferable to standard DSCs though, as transmission the IR pulse requires a metallic element to the devices, not present in typical glass supported cells. The work discussed in chapter 4 provides an ready prepared system of metal antennae incorporation that can be implemented in the investigation of this infrared pulse sintering route. This work uses nanobars of varying lengths: R2 denoted structures indicate an aspect ratio of 2:1, typified by a main absorption peak between 600-700nm, while R4 indicates an aspect ratio of 4:1 with a characteristic absorption further into the near IR at around 800nm. The topography and aspect ratio of these structures is clarified by transmission electron microscopy (TEM) shown in the top panel of figure 5.3 and the transmission profile in the bottom panel.. Nanoparticles were incorporated directly into the paste pre-application as described in section 4.3.4.

Following the pulse-sinter procedure, no thermal processes are applied to the devices in their fabrciation. SEM images of the pulse-sintered films (R2 and R4) indicate qualitatively that the

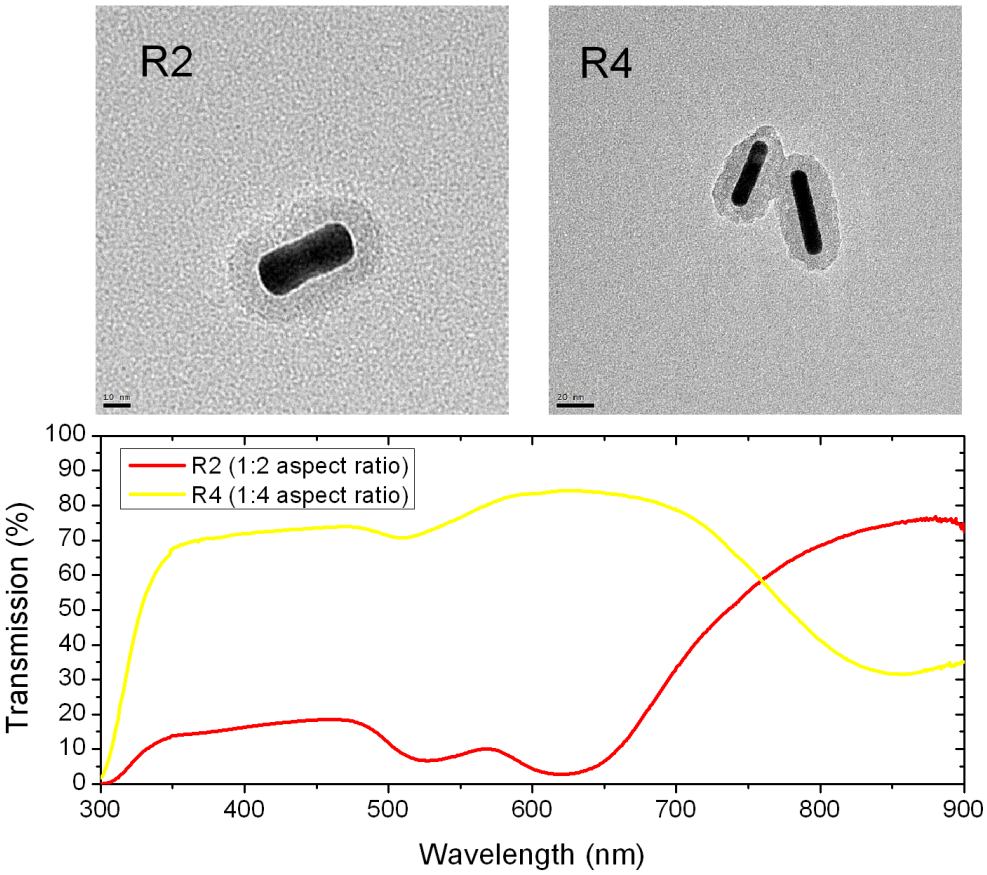

Figure 5.3: Top Panel: TEM graphics illustrating the aspect ratios associated with the silica-shelled gold nanostructures termed R2 (left) and R4 (right). *TEM images courtesy of S. Fairclough, Oxford 2011*

Bottom Panel: transmission spectra for R2 and R4 nanobars in ethanol solution.

pulsing procedure undertaken sinters films consistently with traditional thermal sintering routes, apparently forming a visually comparable mesostructure. Figure 5.4 shows the tranmission spectra for plain titania, R2-containing titania and R4-containing titania. Complete absence of transmission below 360nm in all substrates is due to attenuation by the FTO glass. The shift in the transmission spectra for the plain films between 40% and 50% and later slight increase is likely due to the environs of the pulse chamber which independantly heats significantly thus providing some degree of orthodox thermal sintering. It is observed in both R2- and R4-incorporating films that the typical absorption profiles of the nanostructures are observable in the unsintered film and for the low power pulsed films (40%). At 50% pulse power and above, the nanostructures show a significant and monotonic blue-shift in their absorption profiles, likely due to thermal distortion of the existing topography. With the extreme temperature induction of the pulse, it is likely that the nanostructures may distort towards spherical bodies with the power of the input IR pulse. The monotonic nature of the shift is observed most clearly in the transmission spectra for the R4-incorporating films, with an apparent movement of the absorption peak from 900nm to 650nm.

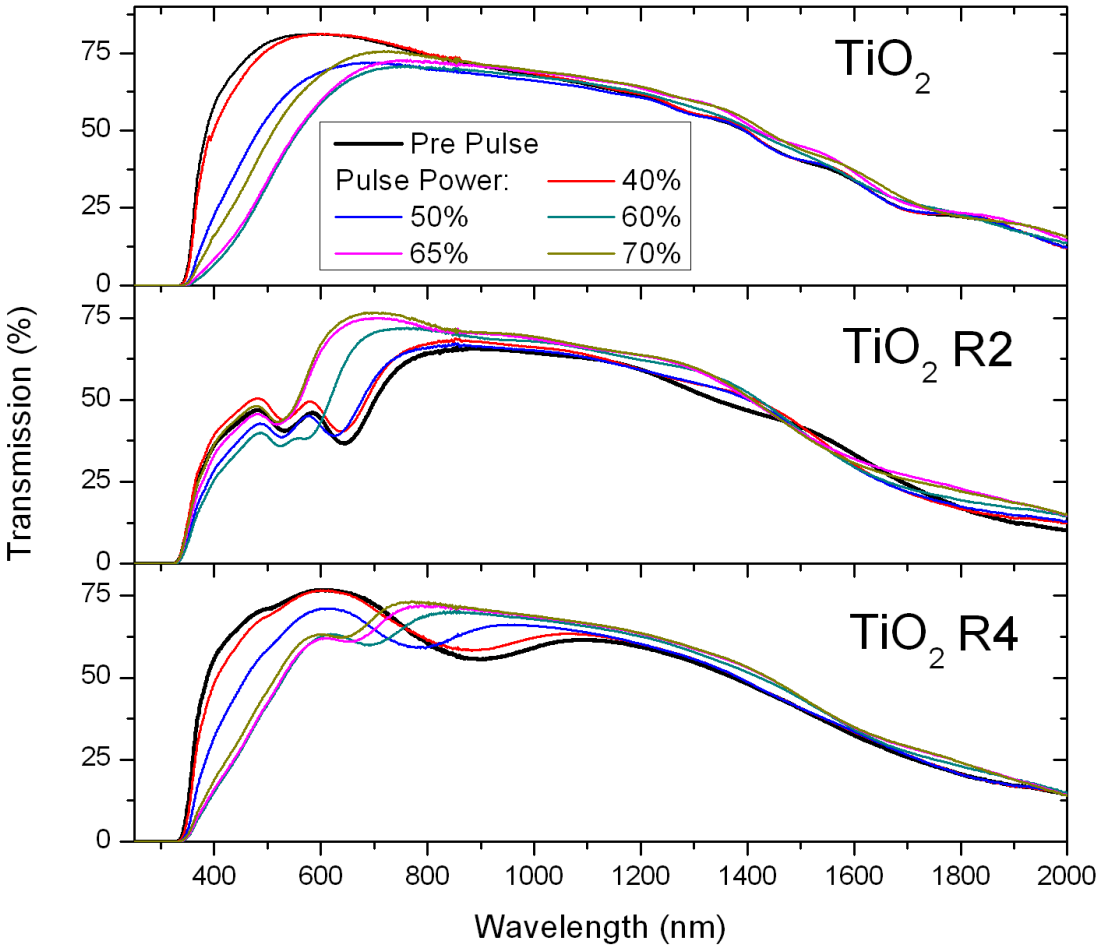

Figure 5.4: Transmission of IR pulse-sintered ~3μm films. The top panel shows the transmission of plain TiO_2, the middle shows TiO_2 containing R2 nanoparticles and the bottom shows TiO_2 containing R4 particles. The black line showing the transmission spectra follwing a 120°C drying but prior to sintering. Coloured lines indicate the varying power of sinter pulse applied. *Transmission data courtesy of T. Watson, Swansea 2011*

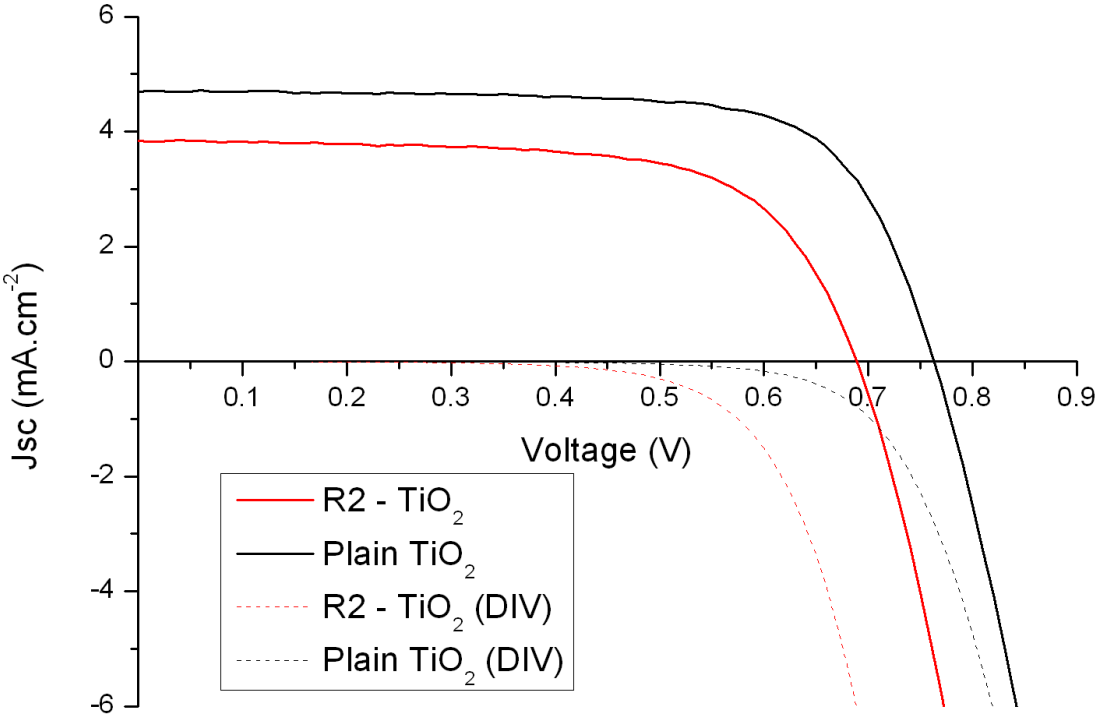

Figure 5.5: Current-voltage characterisation of ~3μm films sintered by IR pulse. Black lines represent orthodox TiO_2 and red indicates TiO_2 incorporating nanobars (2:1 aspect ratio - R2). Dashed lines show dark JV response.

	Current (mA)	Voltage (mV)	Fill Factor (%)	Efficiency (%)
Plain TiO_2	4.69	760	72	2.47
R2 - TiO_2	3.84	690	66	1.69

Table 5.1: Photovoltaic characteristics of IR pulse sintered devices illustrated in figure 5.5, containing plain TiO_2 and R2-incorporating TiO_2.

Due to the uncertainty associated with the sintering procedure and specifically the effect on FTO, no prior etching of the FTO was undertaken and therefore substrates were prepared as electrolyte devices. Substrates optically described in figure 5.4 were immersed in N719 [4] for 18 hours, mounted with a counter electrode and filled with an iodide-triiodide electrolyte.[5] Figure 5.5 shows the current-voltage characterisation associated with these devices. Devices made from

substrates incorporating the 4:1 aspect ratio nanobars have not produced functional devices at the time of writing. Spectral response measurements of both R2 and plain TiO_2 films show near-identical spectra characteristic of the dye suggesting that there is no contribution from the absorption associated with the plasmonic modes of the nanobars.

It may be that the repeated pulse procedures provide enough ambient heat through the chamber walls that the substrates sinter thermally. Continuing shifts observed in the transmission spectra for the nanobar-incorporating films beyond 50% power suggest that the IR pulse is progressively heating the nanostructures; at the time of writing it can not be confirmed that the functional mesostructure fabrication is a result of the IR pulse or ambient thermal generation. Regardless of the route occuring, this process shows promise for drastically reducing the sintering time of titania films while retaining considerable device performance.

5.3 Functional devices not incorporating a traditional hole transporting medium

At some point in the preparation of this thesis a device in fabrication reached the characterisation stage having eluded the spin casting infiltration of a HTM, but was observed to still produce current and have non-negligible overall photoconversion efficiency. Although charge injection from dye molecules directly into electron and hole conductors has been observed,[6, 7] to the author's knowledge there has been no observation of functional devices lacking an orthodox HTM. Figure 5.6 illustrates the current-voltage characteristics of thin mesostructured devices with and without HTM infiltration. This indicates that, although the charge extraction is significantly reduced in comparison to the orthodox devices, photocurrent is still being sucessfully generated and contributing to the device.

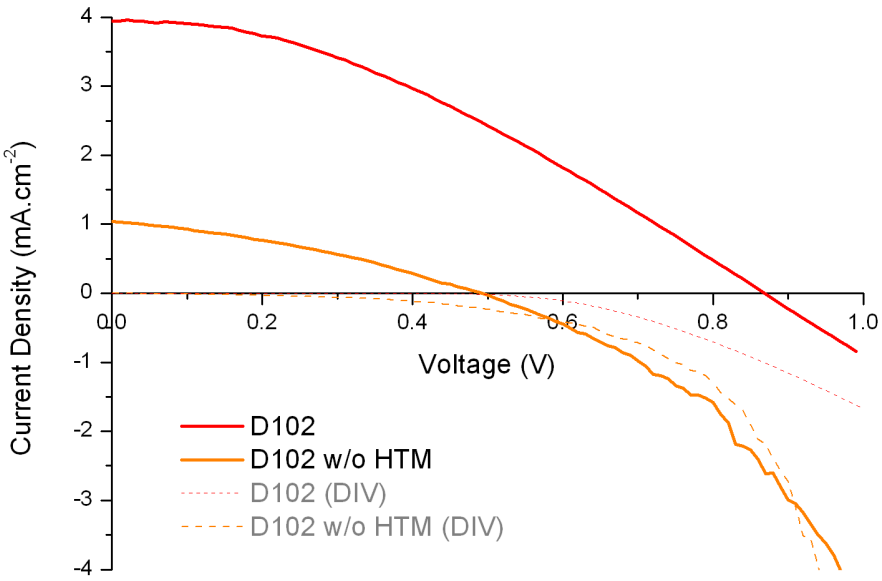

Figure 5.6: Current Density-Voltage characterisation for entirely solid phase DSCs produced using a thin mesostructure (~1μm), dyed with D102 implementing a typical HTM infiltration (red) and with no orthodox HTM beyond the dye molecules themselves (orange). The dotted lines illustrate the dark IV characteristics for these devices.

	Current (mA)	Voltage (mV)	Fill Factor (%)	Efficiency (%)
D102	3.94	830	35	1.16
D102 w/o HTM	1.04	490	33	0.16

Table 5.2: Photovoltaic characteristics of control and HTM-less devices illustrated in figure 5.6.

Experimental devices using the HTM spiro [?] and the mid-visible absorptive dye D102 [8] were fabricated to clarify the action of function with no apparent HTM. Spectral response of complete DSCs was undertaken and absolute and normalised curves are illustrated in figure 5.7. Devices discussed hereafter incorporate extremely thin (<400nm) substrates to also allow the investigation of transport properties. Devices containing both dye and HTM show a peak at around 420nm, characteristic of the spiro HTM in the vicinity of a visible-spectra dye moelecule[?, 9] and an apparently distorted D102 response. There appears to be a reduction in the dye response at ~500nm that may be a result of the absorptive nature of oxidised spiro.[10, 11] This may be a result of the extremely thin mesostructure (<400nm) coupled with a standard spiro cap (~100nm) would reduce the dye optical density with respect to the HTM's, possibly allowing the absorptive spectra of the HTM to compete with the sensitizer.

Those containing no sensitizing molecule and only HTM show a clear response peaking at around 350nm; in this range the HTM and TiO_2 both absorp strongly and will likely provide some photoaction. Devices containing senzitizer with no HTM show an EQE response that mirrors almost precisely the absorption profile of the dye in solution, peaking at ~500 nm with the implication that, in the absence of the HTM there has been no oxidation or otherwise alteration of the dye structure.

5.3.1 Carrier transport measurements

Following the observation of quasi-efficient hole transport in the dye layer the next step was to investigate the variation in carrier transport properties that arise from the presence or lack of an infiltrated HTM.

Figure 5.8 shows preliminary transport data for the short-circuit current and voltage decays (J_{SC} and V_{SC}) of thin mesostrucure devices with and without HTM addition. Devices incorporating HTM are observed to show a stronger dependance of J_{SC} on light intensity than those

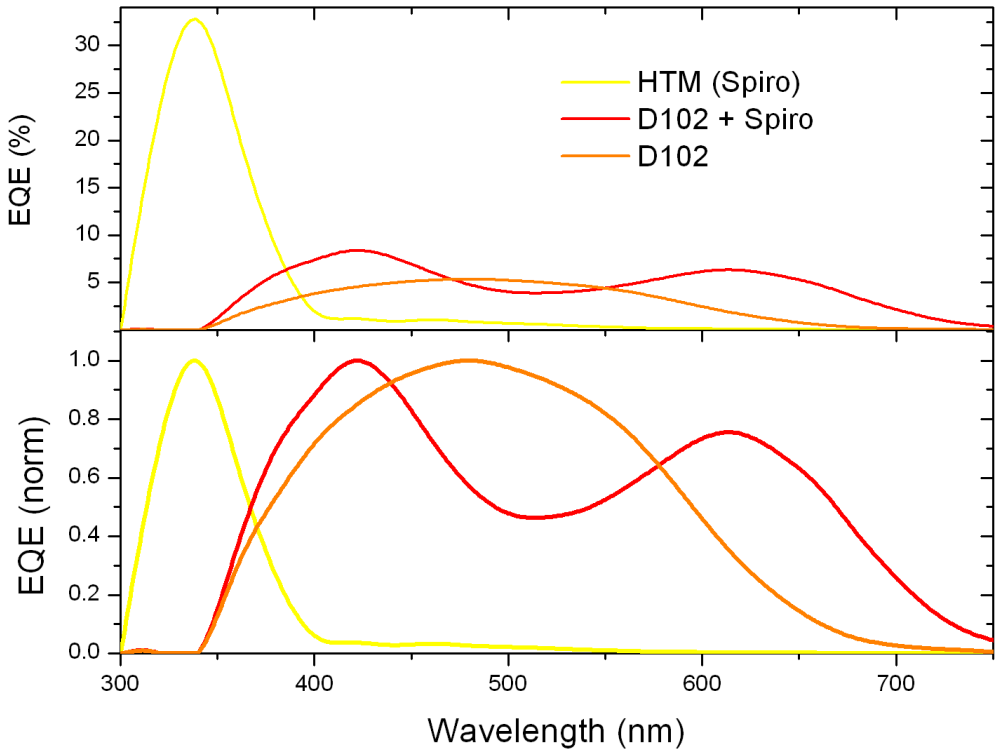

Figure 5.7: Absolute and normalised spectral response characterisation for entirely solid phase DSCs produced using an extremely thin mesostructure (<400nm), dyed with D102 implementing a typical HTM infiltration (red), with no orthodox HTM beyond the dye molecules themselves (orange) and for devices containing HTM with no sensitizing dye (yellow). The bottom panel shows normalised spectra for ease of comparison.

that do not as well as being an order of magnitude slower at low light intensities. The charge collection efficiency can be estimated by:

$$\eta = \frac{k_{coll}}{k_{coll} + krec} \tag{5.1}$$

where the charge collection rate, k_{coll}, can be taken from the short-circuit voltage lifetime and recombination rate, k_{rec}, from the short circuit current lifetime. This suggests a charge collection efficiency of 95% for the HTMless device at 0.01sun that drops to 86% for 1sun, while the devices incorporating an active HTM (spiro) appear to have a η_{coll} of 86% at 0.01sun, increasing to 97% at 1sun. This suggests that the dye molecules themselves may form an effective HTM when photocurrent generation is low, but at typical light intensities may be victim to greater losses

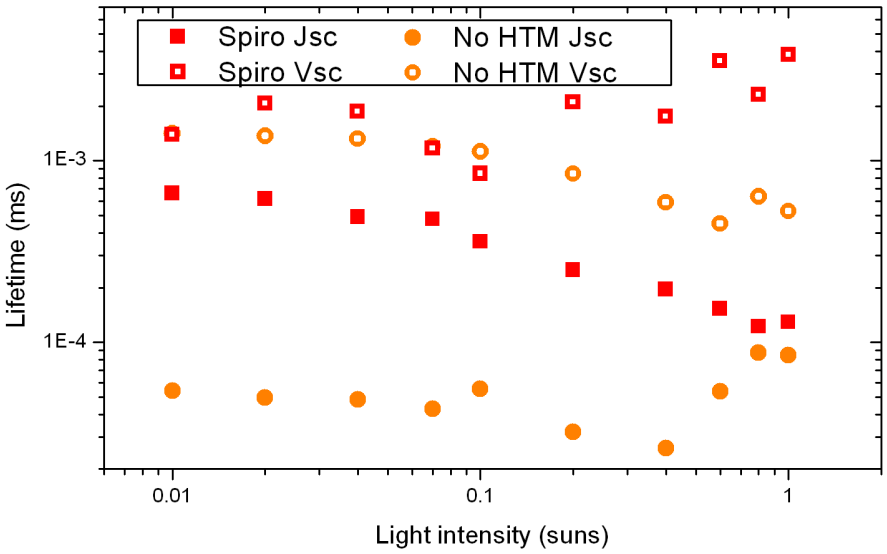

Figure 5.8: Transport measurements for solid phase DSCs using an extremely thin mesostrucure (<400nm), dyed with D102 implementing a typical HTM (red) and with no orthodox HTM (orange). Measured are the J_{SC} decay and V_{SC} decay.

as the hopping of carriers on a surface dye layer will inevitably be subject to recombination.

In conclusion, it has been observed that in the absence of an orthodox hole transport medium significant photocurrent can still be generated. Although the data presented in this section is entirely preliminary, it may be that the circumstances outlined here can be usefully studied to provide insight into the balance of charge transport within dye sensitized devices and the possible action of dye molecules themselves.

References

[1] Z. B. Hill, D. B. Rodovsky, J. M. Leger, and G. P. Bartholomew, "Synthesis and utilization of perylene-based n-type small molecules in light-emitting electrochemical cells.," *Chemical communications*, pp. 6594–6, Dec. 2008.

[2] J. Qi, X. Dang, P. T. Hammond, and A. M. Belcher, "Highly Efficient Plasmon-Enhanced Dye-Sensitized Solar Cells through Metal@Oxide Core-Shell Nanostructure.," *ACS nano*, vol. 5, pp. 7108–16, Sept. 2011.

[3] T. Watson, I. Mabbett, H. Wang, L. Peter, and D. Worsley, "Ultrafast near infrared sintering of TiO 2 layers on metal substrates for dye-sensitized solar cells," *Progress In Photovoltaics*, pp. 482–486, 2011.

[4] Y. Tachibana, K. Nazeeruddin, M. Gr, D. R. Klug, and J. R. Durrant, "Electron injection kinetics for the nanocrystalline TiO2 films sensitised with the dye (Bu4N)2Ru(dcbpyH)2(NCS)2," *Chemical Physics*, vol. 285, pp. 127–132, 2002.

[5] P. Wang, C. Klein, R. Humphry-Baker, S. M. Zakeeruddin, and M. Gratzel, "Stable >8% efficient nanocrystalline dye-sensitized solar cell based on an electrolyte of low volatility," *Applied Physics Letters*, vol. 86, no. 12, p. 123508, 2005.

[6] B. Mahrov, G. Boschloo, a. Hagfeldt, L. Dloczik, and T. Dittrich, "Photovoltage study of charge injection from dye molecules into transparent hole and electron conductors," *Applied Physics Letters*, vol. 84, no. 26, p. 5455, 2004.

[7] F. O. Lenzmann, B. C. O'Regan, J. J. T. Smits, H. P. C. E. Kuipers, P. M. Sommeling, L. H. Slooff, and J. a. M. van Roosmalen, "Dye solar cells without electrolyte or hole-transport layers: a feasibility study of a concept based on direct regeneration of the dye by metallic conductors," *Progress in Photovoltaics: Research and Applications*, vol. 13, pp. 333–340, June 2005.

[8] L. Schmidt-Mende, U. Bach, R. Humphry-Baker, T. Horiuchi, H. Miura, S. Ito, S. Uchida, M. Grï¿œtzel, and M. Gratzel, "Organic Dye for Highly Efficient Solid-State Dye-Sensitized Solar Cells," *Advanced Materials*, vol. 17, pp. 813–815, Apr. 2005.

[9] M. D. Brown, T. Suteewong, Kumar, V. D'Innocenzo, A. Petrozza, M. M. Lee, U. Wiesner, and H. J. Snaith, "Plasmonic Dye-Sensitized Solar Cells Using Core-Shell Metal-Insulator Nanoparticles," *Nano Letters*, vol. 11, pp. 438–445, Feb. 2011.

[10] X. Jiang, T. Marinado, E. Gabrielsson, D. P. Hagberg, L. C. Sun, and A. Hagfeldt, "Structural Modification of Organic Dyes for Efficient Coadsorbent-Free Dye-Sensitized Solar Cells," *Journal of Physical Chemistry C*, vol. 114, pp. 2799–2805, 2010.

[11] U. B. Cappel, E. A. Gibson, A. Hagfeldt, and G. Boschloo, "Dye Regeneration by Spiro-MeOTAD in Solid State Dye-Sensitized Solar Cells Studied by Photoinduced Absorption Spectroscopy and Spectroelectrochemistry," *Society*, pp. 6275–6281, 2009.

Chapter 6

Conclusions and Outlook

Prospective solutions to the light harvesting insufficiencies of both weak, broad and strong, narrow sensitizers have been outlined in this thesis. Although these are by no means ultimate solutions, they provide ample area for further research.

In the work dealing with coadsorption (Chapter 3), the apparently simple goal of extending the absorption spectrum via a system of complementarily-absorptive dye molecules bore unintended interest in the form of an unprecendented energy transfer process that appears to enhance the photoconversion efficiency of both dyes. This was investigated both electronically and spectroscopically and it was demonstrated that resonant energy transfer is occuring from the visible to the near-IR dye, providing a previously unanticipated charge generation route that apparently works in conjunction with the direct charge injection from the dye molecule itself. The FRET process outlined is suggested to provide an alternate charge generation mechanism and therefore relax the design criteria for visible absorbing sensitizers. The work undertaken culminated in some of the most efficient organic solid state dye sensitized solar cells so far recorded.

As noted in Chapter 4, there had previously been significant discussion and conjecture on the possiblity of plasmonic hybrid solar cells whilst no devices conclusively demonstrating the concept had, to the author's knowledge, been fabricated. During the course of this research the author has fabricated functional plasmonic hybrid DSCs and has proven their effect through electronic, optical and spectroscopic measurements. Clear photovoltaic efficiency improvements have been observed and investigations have confirmed that the enhancements observed are of a plasmonic nature. The work done on plasmonics in the preparation of this thesis has already been built upon by other groups and it is believed that the research done on plasmonic integration, especially with regards to the core-shell architecture, will prove an important cornerstone upon which much further development can be undertaken.

Chapter 5 describes a number of other projects that are either smaller or incomplete and in some cases build on the work of other chapters. The possibility of entirely abstracting the photon collecting and carrier injection functions of the dyes in these devices is explored with the cosensitization of a proven carrier injecting dye with a non-injecting dye that shows good

absorption characteristics and the in doing so utilise the energy transfer phenomenon described extensively in chapter 3.

Further to the work done investigating nanoparticle integration, there may be some means to either utilising these plasmonic structures as antennae for the transfer of heat in sintering processes or by altering the topography of the nanostructures used to exploit the excellent absorptive properties that arise in more complex nanoscale strucures.

The functional hole transport properties of a dye-coated titania mesostructure have been investigated after it was observed that devices composing only a sensitizer with no hole transport medium can generate significant photocurrent.

The overriding theme of this thesis is the enhancement of the light harvesting of dye-sensitized solar cells. Although an entirely open-ended enterprise, this thesis has outlined and proven two control systems which, through drastically different routes, acheive this goal. These investigations have utlised the physical concepts of plasmonics and resonant energy transfer that had previously not been used to any great effect in dye sensitized solar cells and has proved their viability.

Refereed Publications and Conference Presentations

Refereed Publications

"Plasmonic dye-sensitized solar cells using core-shell metal-insulator nanoparticles"
Brown. M. D.; Suteewong. T.; Kumar, R. S.; D'Innocenzo, V.; Petrozza, A.; Lee, M.; Wiesner, U.; Snaith, H. J.;
Nano Letters (2011)

"Surface Energy Relay between Cosensitizer Molecules in Solid-state Dye-sensitised Solar Cells"
Brown, M. D.; Parkinson, P.; Torres, T.; Miura, H.; Herz, L. M.; Snaith, H. J.;
The Journal of Physical Chemistry, C (2011)

Conference Presentations

"Surface Energy Relay Between Cosensitizer Molecules in Solid-state Dye-sensitized Solar Cells"
Oral Presentation, International Conference on Advanced Materials (ICAM), September 2009, Rio de Janiero, Brazil.

"Plasmonic Dye-sensitized Solar Cells"
Oral Presentation, Hybrid and Organic Photovoltaics Conference (HOPV), May 2010, Assisi, Italy.

"System Designed to realise Plasmonic Dye-sensitized Solar Cells"
Oral Presentation, Supergen, July 2011, Imperial University, London, UK.

Appendix A

Appendices

A.1 Structures of dyes and hole transport molecules

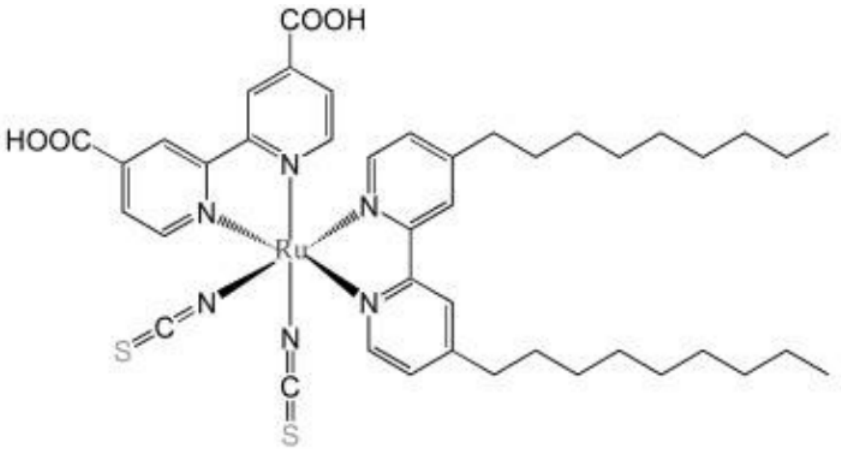

Figure A.1: Z907 molecular arrangement [?]

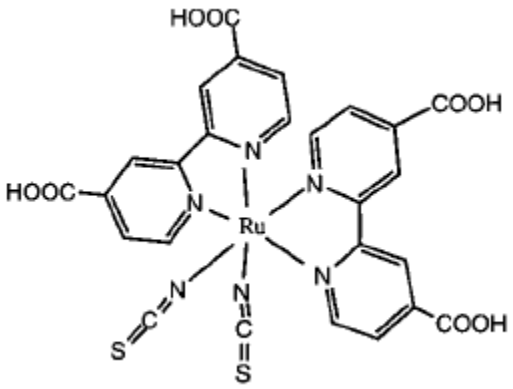

Figure A.2: N719 structure[1]

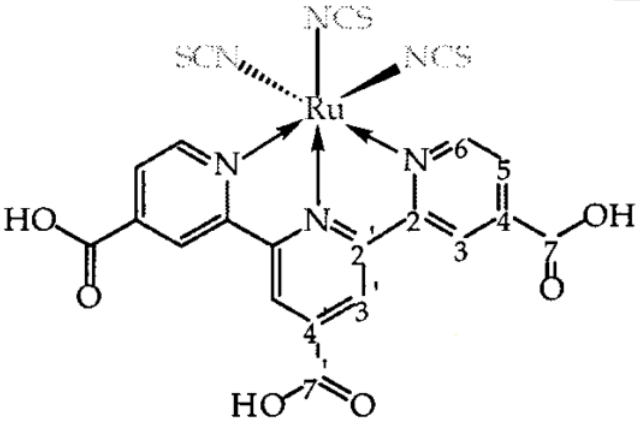

Figure A.3: Black Dye structure[2]

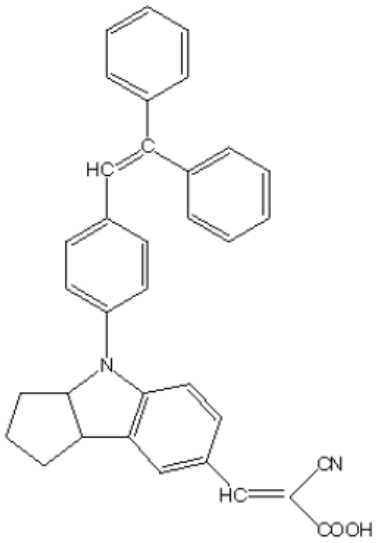

Figure A.5: D131 structure[4]

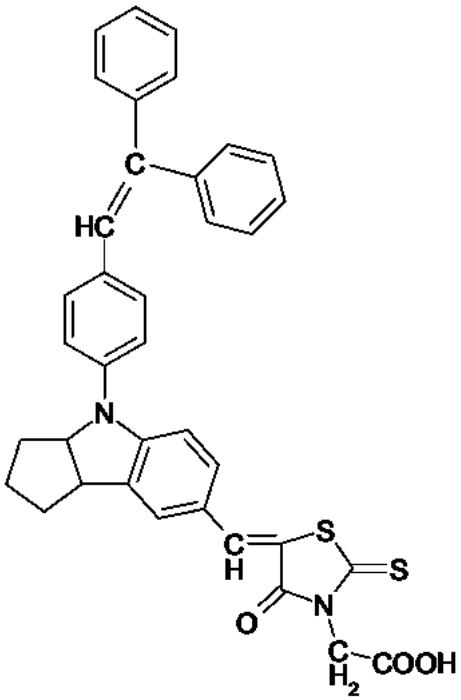

Figure A.4: D102 structure[3]

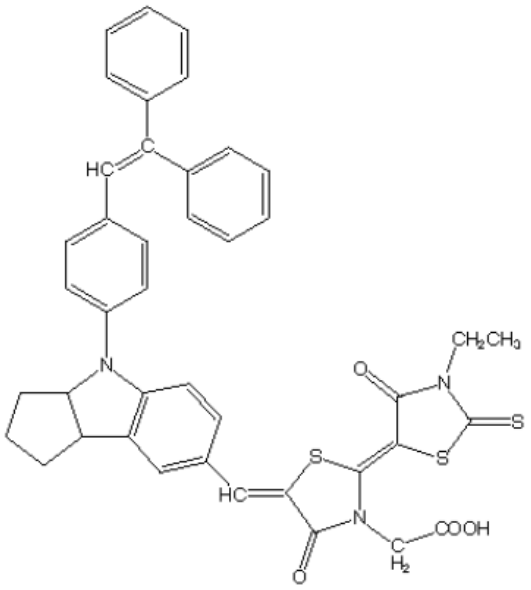

Figure A.6: D149 structure[?]

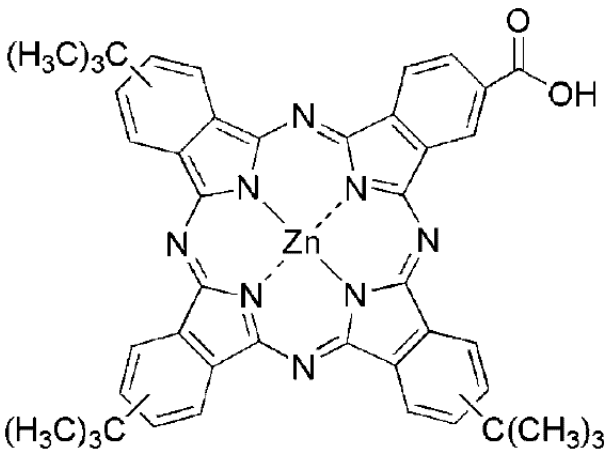

Figure A.7: TT1 structure[5]

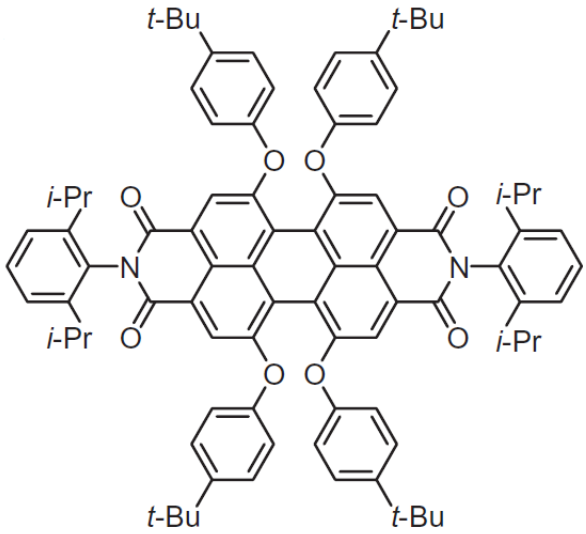

Figure A.9: PTCDI structure. [?]

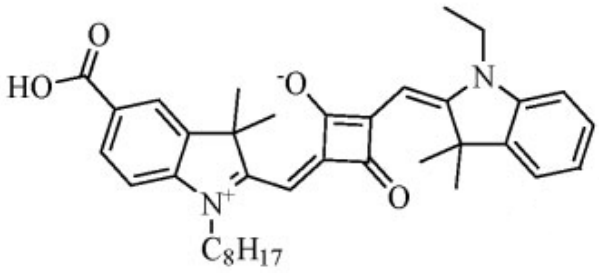

Figure A.8: SQ02 structure[6]

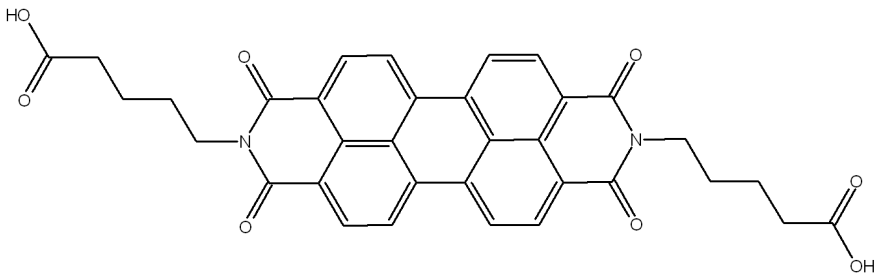

Figure A.10: Perylene diimide structure *Molecule synthesis and structural image courtesy of T.E. Hewat, Edinbrugh, 2011*

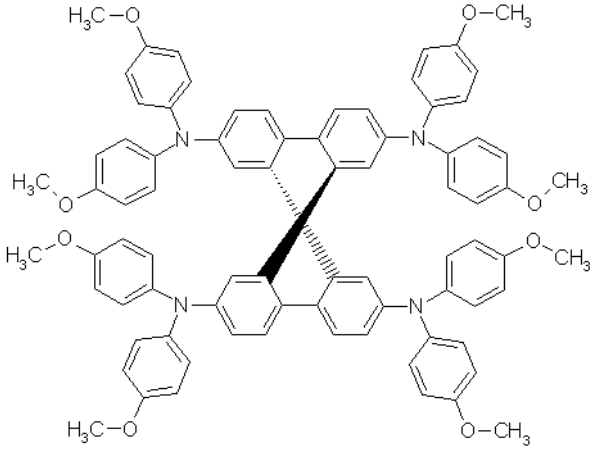

Figure A.11: Spiro OMeTAD structure[?]

A.2 Time correlated single photon counting

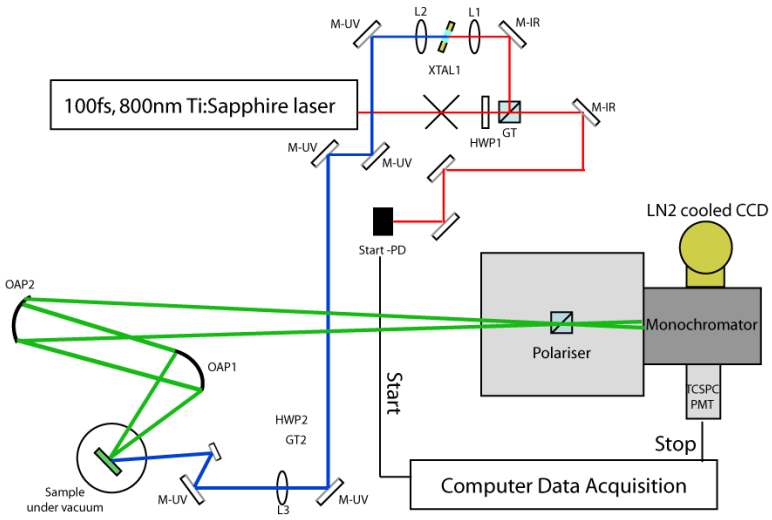

Figure A.12: Simplified TCSPC optical arrangement. *Figure courtesy of Patrick Parkinson, Oxford 2009*

A.3 Nanoparticle Synthesis Proceedures

Au nanoparticles with and without a thin sodium silicate shell were prepared according to previously published methods with slight modification.[7, 8] Briefly, for the synthesis of bare Au nanoparticles, hydrogen tetrachloroaurate (III) (HAuCl4.3H2O, 0.095 g) was dissolved in water (500 mL). The solution was heated to boil. 1%w/w citric acid solution (citric acid trisodium salt dihydrate, 33 mL) was added into boiling solution. The solution quickly turned colorless then rose-black and later rose colored. After continuous boiling for 20 minutes, the solution was removed from the heat source and allowed to cool naturally. At this point, citrate-stabilized Au nanoparticles had formed. To replace citrate on the particle surface with 3-aminopropyl triethoxysilane (APTES), an aqueous solution of APTES (5 mL, 1.71 mM) was added to the Au solution under vigorously stirring over 30 minutes. The solution was allowed to sit overnight. For Au nanoparticles with thin silica shell (Au-SiO_2 nanoparticles), 0.54%w/w sodium silicate solution (20 mL) was added 30 minutes after the addition of APTES. The solution was stirred for 10 minutes and allowed to sit for 2 days. The pH of the sodium silicate solution was adjusted to 10-11 by amberlite IR-120 before addition to the Au solution. The sizes of the Au core and Au-SiO_2 core-shell nanoparticle as well as the thickness of the silica shell were characterized by transmission electron microscopy (TEM). *Synthesis procedure reproduced verbatim from 2011 Nanoletters paper.*

References

[1] Y. Tachibana, K. Nazeeruddin, M. Gr, D. R. Klug, and J. R. Durrant, "Electron injection kinetics for the nanocrystalline TiO2 films sensitised with the dye (Bu4N)2Ru(dcbpyH)2(NCS)2," *Chemical Physics*, vol. 285, pp. 127–132, 2002.

[2] M. K. Nazeeruddin, P. Pechy, T. Renouard, S. M. Zakeeruddin, R. Humphry-Baker, P. Comte, P. Liska, L. Cevey, E. Costa, V. Shklover, L. Spiccia, G. B. Deacon, C. A. Bignozzi, and M. Gratzel, "Engineering of efficient panchromatic sensitizers for nanocrystalline TiO2-based solar cells," *Journal of the American Chemical Society*, vol. 123, pp. 1613–1624, 2001.

[3] L. Schmidt-Mende, U. Bach, R. Humphry-Baker, T. Horiuchi, H. Miura, S. Ito, S. Uchida, M. Grï¿œtzel, and M. Gratzel, "Organic Dye for Highly Efficient Solid-State Dye-Sensitized Solar Cells," *Advanced Materials*, vol. 17, pp. 813–815, Apr. 2005.

[4] R. Jose, a. Kumar, V. Thavasi, and S. Ramakrishna, "Conversion efficiency versus sensitizer for electrospun TiO(2) nanorod electrodes in dye-sensitized solar cells.," *Nanotechnology*, vol. 19, p. 424004, Oct. 2008.

[5] J. J. Cid, M. Garcia-Iglesias, J. H. Yum, A. Forneli, J. Albero, E. Martinez-Ferrero, P. Vazquez, M. Gratzel, M. K. Nazeeruddin, E. Palomares, and T. Torres, "Structure-Function Relationships in Unsymmetrical Zinc Phthalocyanines for Dye-Sensitized Solar Cells," *Chemistry-a European Journal*, vol. 15, pp. 5130–5137, 2009.

[6] T. Geiger, S. Kuster, J.-H. Yum, S.-J. Moon, M. K. Nazeeruddin, M. Grdtzel, and F. Esch, "Molecular Design of Unsymmetrical Squaraine Dyes for High Efficiency Conversion of Low Energy Photons into Electrons Using TiO2 Nanocrystalline Films," *Advanced Functional Materials*, vol. 19, pp. 2720–2727, 2009.

[7] B. V. Enustun and J. Turkevich, "Coagulation of Colloidal Gold," *Journal of the American Chemical Society*, vol. 85, p. 3317, 1963.

[8] L. M. LizMarzan, M. Giersig, and P. Mulvaney, "Synthesis of nanosized gold-silica core-shell particles," *Langmuir*, pp. 4329–4335, 1996.